ISSN 2782-2192 (Print)
ISSN 2782-2206 (Online)
DOI: 10.17277/jamt

Journal of Advanced Materials and Technologies

Vol. 10, No. 4.
2025

Том 10, № 4.
2025

16+

Journal of Advanced Materials and Technologies

Scientific Journal

"Journal of Advanced Materials and Technologies" is a peer-reviewed scientific journal of research in materials science and related issues in materials physics and mechanics.

"Journal of Advanced Materials and Technologies" publishes original articles, reviews, short reports written by both renowned scientists and young researchers that contribute to the development of modern materials science.

The journal promotes research and exchange of information in the field of theoretical and practical research into materials science, modeling of processes involved in the creation of new materials, including nanomaterials, their properties and application.

The journal papers and metadata abstracted and indexed in CAS (American Chemical Society), Google Scholar, Research4life, Dimensions, ROAD, OpenAlex, Scilit.

ISSN 2782-2192 (Print), ISSN 2782-2206 (Online)

Rename information	Advanced materials & technologies (2016-2021) Print ISSN 2414-4606, Online ISSN 2541-8513
The journal was founded	2016
Publication frequency	Quarterly
Founders	Tambov State Technical University (TSTU), Merzhanov Institute of Structural Macrokinetics and Materials Sciences of Russian Academy of Sciences (ISMAN)
Postal address	TSTU: Bld. 2, 106/5, Sovetskaya St., Tambov, 392000 ISMAN: 8, Academician Osipyan St., Moscow region, Chernogolovka, 142432
Editorial office address	Bld. 2, 106/5, Sovetskaya St., Tambov, 392000
Contacts	Phone + 7 4752 63 03 91; amt.journal@yandex.ru
Printing House	TSTU Publishing, 112A, Michurinskaya St., Tambov, 392032 Phone + 7 4752 63 03 91; + 7 4752 63 07 46
Website ***E-mail*** ***Phone***	http://amt.tstu.ru/ amt.journal@yandex.ru +7 4752 63 92 93
Subscription	The electronic version of the Journal is freely available on the journal's website, as well as in open access databases.
Editor-in-Chief	Mikhail I. Alymov, D. Sc. (Engineering), Professor, Corresponding Member of the Russian Academy of Sciences

Journal of Advanced Materials and Technologies

Научный журнал

«Journal of Advanced Materials and Technologies» – научный рецензируемый журнал, посвященный исследованиям в области материаловедения и примыкающих вопросов физики и механики материалов.

Журнал «Journal of Advanced Materials and Technologies» публикует оригинальные статьи, обзоры, краткие сообщения, содействующие развитию современной науки о материалах, подготовленные как известными учеными, так и молодыми специалистами.

Миссия журнала – обмен актуальной научной информацией в области теоретических и практических исследований и моделирования процессов, связанных с получением, определением свойств новых материалов, в том числе наноразмерных, и их применения.

Средство массовой информации периодическое печатное издание, журнал «Journal of Advanced Materials and Technologies» зарегистрировано Федеральной службой по надзору в сфере связи, информационных технологий и массовых коммуникаций. Регистрационный номер СМИ ПИ № ФС 77-74804 от 25.01.2019.

Журнал входит в перечень рецензируемых научных изданий (перечень ВАК Минобрнауки РФ) от 16 декабря 2021 г. по научным специальностям: 1.4.15 – Химия твердого тела; 2.6.6 – Нанотехнологии и наноматериалы; 2.6.13 – Процессы и аппараты химических технологий; 2.6.17 – Материаловедение.

Журнал индексируется в РИНЦ, RSCI, CAS (American Chemical Society), Google Scholar, Research4life, Dimensions, ROAD, OpenAlex, Scilit.

ISSN 2782-2192 (Print), ISSN 2782-2206 (Online)

Сведения о переименовании	«Advanced materials & technologies» (2016–2021) Print ISSN 2414-4606, Online ISSN 2541-8513
Журнал основан	2016 г.
Периодичность	4 раза в год
Учредители	Федеральное государственное бюджетное образовательное учреждение высшего образования «Тамбовский государственный технический университет» (ФГБОУ ВО «ТГТУ»), Федеральное государственное бюджетное учреждение науки Институт структурной макрокинетики и проблем материаловедения им. А. Г. Мержанова Российской академии наук (ИСМАН)
Адреса учредителей	ФГБОУ ВО «ТГТУ»: 392000, Тамбовская область, г.о. город Тамбов, г. Тамбов, ул. Советская, д. 106/5, помещ. 2, ИСМАН: 142432, Московская область, г. Черноголовка, ул. Академика Осипьяна, д. 8
Адрес издателя	ФГБОУ ВО «ТГТУ»: 392000, Тамбовская область, г.о. город Тамбов, г. Тамбов, ул. Советская, д. 106/5, помещ. 2
Адрес редакции	392000, Тамбовская область, г.о. город Тамбов, г. Тамбов, ул. Советская, д. 106/5, помещ. 2
Контакты	Тел.: + 7 4752 63 03 91; amt.journal@yandex.ru
Адрес типографии	392032, Тамбовская обл., г. Тамбов, ул. Мичуринская, д. 112А Тел.: + 7 4752 63 03 91; + 7 4752 63 07 46
Сайт	http://amt.tstu.ru/
E-mail	amt.journal@yandex.ru
Телефон	+7 4752 63 92 93
Подписка	Электронная версия журнала находится в свободном доступе на сайте журнала, а также в базах данных открытого доступа
Главный редактор	Алымов Михаил Иванович, д. т. н., профессор, член-корреспондент РАН

EDITORIAL BOARD

СОВЕТ РЕДАКТОРОВ

CONTENTS

Original papers

Manufacturing processes and systems

Nanostructured, nanoscale materials and nanodevices

Materials for energy and environment, next-generation photovoltaics, and green technologies

Reviews

Materials for energy and environment, next-generation photovoltaics, and green technologies

СОДЕРЖАНИЕ

Оригинальные статьи

Производственные процессы и системы

Наноструктурированные, наноразмерные материалы и наноустройства

Материалы для энергетики и окружающей среды, фотоэлектрическая энергия следующего поколения и зеленые технологии

Обзор

Материалы для энергетики и окружающей среды, фотоэлектрическая энергия следующего поколения и зеленые технологии

Original papers
Manufacturing processes and systems

УДК 66.02:66.097.3:66.097.5 DOI: 10.17277/jamt-2025-10-04-290-300

Synthesis of Co-Mn/diatomite composites by low-temperature combustion

© Roza I. Jussupkaliyeva[a]✉, Vyacheslav N. Borshch[b], Inna M. Bystrova[b], Elena V. Pugacheva[b], Natalia Yu. Khomenko[b], ArtemV. Rukhov[c], Svetlana I. Pomogailo[b,d]

[a] *Zhangir Khan West Kazakhstan Agrarian Technical University, 51, Zhangir Khan St., Uralsk, 090009, Republic of Kazakhstan,*
[b] *Merzhanov Institute of Structural Macrokinetics and Materials Science, Russian Academy of Science, 8, Academician Osipyan St., Chernogolovka, 142432, Russian Federation,*
[c] *Tambov State Technical University, Bld. 2, 106/5, Sovetskaya St., Tambov, 392000, Russian Federation,*
[d] *All-Russian Institute for Scientific and Technical Information, 20, Usievich St., Moscow, 125190, Russian Federation*

✉ rozaid2@mail.ru

Abstract: Co-Mn-containing composites based on diatomite as a carrier (matrix) were prepared using the energy-efficient low-temperature combustion method using natural and activated diatomite from the Utesai deposit (Republic of Kazakhstan) as a support (matrix). Activation included the stages of washing with water, calcination at 500 °C, and treatment with an HCl solution in various combinations. The phase containing 5 wt. % of Co + 5 wt. % of Mn (calculated as metals) was applied to diatomite by low-temperature combustion of a mixture of Co and Mn nitrates (oxidizers) with urea (reducing agent, fuel) applied to diatomite. The maximum temperature in the combustion wave reached 337 °C. The physicochemical properties of the composites were studied using X-ray diffraction, SEM/EDS, and the specific surface area was measured according to BET on nitrogen. The main phases in the composites, according to XRD data, were modifications of SiO_2 (quartz, tridymite, and cristobalite). According to the SEM/EDS results, there is an uneven distribution of the Co-Mn-containing phase components over the surface of the catalyst granules, due to the heterogeneity of the surface morphology and internal pores of natural diatomite. Impurity elements (Mg, Al, Na, K, Ca, Fe) were also detected in the composition of the supports and catalysts. The specific surface area of the support samples ranged from 56.0 to 83.5 $m^2 \cdot g^{-1}$, and that of the composites – from 46.4 to 78.5 $m^2 \cdot g^{-1}$. The resulting composites are expectedto be used as catalysts for deep oxidation of CO and hydrocarbons for environmentally important technologies for the neutralization of man-made exhaust and waste gases.

Keywords: diatomite; activation; low-temperature combustion; cobalt; manganese; composites.

For citation: Jussupkaliyeva RI, Borshch VN, Bystrova IM, Pugacheva EV, Khomenko NYu, Rukhov AV, Pomogailo SI. Synthesis of Co-Mn/diatomite composites by low-temperature combustion. *Journal of Advanced Materials and Technologies*. 2025;10(4):290-300. DOI: 10.17277/jamt-2025-10-04-290-300

Синтез композитов состава Co-Mn/диатомит методом низкотемпературного горения

© Р. И. Джусупкалиева[a]✉, В. Н. Борщ[b], И. М. Быстрова[b], Е. В. Пугачева[b], Н. Ю. Хоменко[b], А. В. Рухов[c], С. И. Помогайло[b,d]

[a] *Западно-Казахстанский аграрно-технический университет им. Жангир хана, ул. Жангир хана, 51, Уральск, 090009, Республика Казахстан,*
[b] *Институт структурной макрокинетики и проблем материаловедения им. А. Г. Мержанова РАН, ул. Академика Осипьяна, 8, Черноголовка, 142432, Российская Федерация,*
[c] *Тамбовский государственный технический университет, ул. Советская, 106/5, пом. 2, Тамбов, 392000, Российская Федерация,*
[d] *Всероссийский институт научной и технической информации РАН, ул. Усиевича, 20, Москва, 125190, Российская Федерация*

✉ rozaid2@mail.ru

Аннотация: Энергоэффективным методом низкотемпературного горения получены Co-Mn-содержащие композиты на основе природного и активированного диатомита Утесайского месторождения (Республика Казахстан) в качестве носителя (матрицы). Активация включала этапы промывки водой, прокалки при 500 °C,

а также обработки раствором HCl, в различных сочетаниях. Нанесение фазы, содержащей 5 мас. % Co + 5 мас. % Mn (в расчете на металлы), на диатомит производили путем низкотемпературного горения смеси нитратов Co и Mn (окислители) с мочевиной (восстановитель, горючее). Максимальная температура в волне горения достигала 337 °C. Исследованы физико-химические свойства композитов методами РФА, СЭМ/ЭДС, и измерена удельная поверхность по адсорбции азота. Основными фазами в составе композитов по данным РФА являлись модификации SiO_2 (кварц, тридимит и кристобалит). Согласно результатам СЭМ/ЭДС, имеет место неравномерное распределение компонентов Co-Mn-содержащей фазы по поверхности гранул катализаторов, связанное с неоднородностью морфологии поверхности и внутренних пор природного диатомита. Также были обнаружены примесные элементы (Mg, Al, Na, K, Ca, Fe). Удельная поверхность по БЭТ образцов носителей составила от 56,0 до 83,5 $м^2$/г, а композитов – от 46,4 до 78,5 $м^2$/г. Полученные композиты предполагается использовать как катализаторы процесса глубокого окисления CO и углеводородов для экологически важных технологий нейтрализации выхлопных и отходящих газов техногенной природы.

Ключевые слова: диатомит; активация; низкотемпературное горение; кобальт; марганец; композиты.

Для цитирования: Jussupkaliyeva RI, Borshch VN, Bystrova IM, Pugacheva EV, Khomenko NYu, Rukhov AV, Pomogailo SI. Synthesis of Co-Mn/diatomite composites by low-temperature combustion. *Journal of Advanced Materials and Technologies*. 2025;10(4):290-300. DOI: 10.17277/jamt-2025-10-04-290-300

1. Introduction

Diatomite is a sedimentary rock formed from the remains of diatomaceous algae, with abundant deposits in Kazakhstan and Russia [1, 2]. The main component of diatomite is silica SiO_2 (70–98 wt. %, depending on the deposit), largely in an amorphous state. Its characteristic feature is a highly porous structure, resulting in a low density (on average 0.5–0.7 $g \cdot cm^{-3}$), a high specific surface area, high adsorption capacity, and low thermal conductivity. Furthermore, it is quite heat-resistant and resistant to aggressive environments. Due to these properties, as well as its low cost, diatomite is widely used in various industries and construction. Thus, in its original or modified forms, it is an effective sorbent for removing oil spills and waste containing petroleum products [3], water purification from aromatic compounds and esters [4], inorganic salts, in particular, phosphates (in combination with $Mg(OH)_2$ [5]). Particular attention is paid to the development of diatomite-based adsorbents for the removal of organic dyes from waste and discharge water [6, 7]. High specific surface area and chemical stability are attractive factors for the use of diatomite as a carrier of deposited catalysts for various processes. The range of developed diatomite-based catalysts is currently quite wide. Diatomite modified with organoaluminum compounds turned out to be an active catalyst for ethylene polymerization [8]; with deposited transition metal salts it showed high activity in the process of catalytic pyrolysis of the propane-butane fraction to obtain multiwalled carbon nanotubes [9]. Diatomite-based catalysts have demonstrated high selectivity in the isomerization of α-pinene [10], the hydrogenation of vegetable oils to particularly valuable cis-isomers [11], and the hydrogenation of CO_2 to methane [12]. Developments have been made of catalysts for the deep oxidation of CO and propane [13], formaldehyde [14, 15], and the liquid-phase oxidation of As(III) compounds in an alkaline medium [16]. Catalysts for photooxidation processes in both gaseous and liquid media, including those for water purification processes, are being intensively developed [17–21].

The most common method for synthesizing supported catalysts is the impregnation of carriers with solutions of active transition metal salts (most often nitrates), followed by drying and calcination [9, 23]. The disadvantage of this method is the high calcination temperature (usually not less than 500 °C) and the corresponding energy costs, as well as toxic gas emissions containing nitrogen oxides. An alternative to this method is the relatively recently developed energy-efficient method of self-propagating surface thermal synthesis or the low-temperature combustion method [24–32]. Its essence lies in impregnating the carrier with a mixture of solutions of an oxidizer (usually transition metal nitrates) and a reducing agent (fuel) – a water-soluble organic compound (urea, glycine, citric acid, sucrose, sorbitol, etc.). After drying, slight heating (< 200 °C) initiates a self-sustaining combustion reaction in the sample, usually proceeding in a wave mode. The gaseous products of combustion are water vapor, CO_2, and, in the case of nitrogen-containing fuels, N_2. The resulting catalysts often have a nanosized active phase, which contributes to their high activity and selectivity. We previously used this method to obtain a number of catalysts for the deep oxidation of CO and propane, as well as the hydrogenation of CO_2 [29–32, 36] on a wide range of supports (γ-Al_2O_3,

silica gel (including modified Al_2O_3), zeolites NaX and ZSM-5, halloysite (natural aluminosilicate nanotubes), and the natural silica mineral opoka). The catalysts demonstrated high activity, selectivity, and stability in the processes studied. In [29], we were the first to show that this method can be used to obtain not only oxide but also metallic phases of transition metals in the catalyst composition.

In this study, a low-temperature combustion method was used to obtain composites containing Co-Mn phases based on the initial and activated diatomite. These composites are expected to be used in the future as catalysts for the deep oxidation of CO and hydrocarbons for environmentally important technologies for the neutralization of exhaust and waste gases of anthropogenic origin. The composition of the Co-Mn-containing phase was selected based on the results of our previous studies and literature data [23, 29, 33–36], which showed that catalysts supported on various supports with a bimetallic active phase Co-Mn were characterized by high activity and stability in the process of deep oxidation of CO and propane. The study was aimed at studying the features of the synthesis process of various samples of the Co-Mn/diatomite system, and the physicochemical characteristics of the obtained materials.

2. Materials and Methods

2.1. Composite preparation

2.1.1. Preparation of the carrier

Diatomite from the Utesai deposit in the Republic of Kazakhstan was used as the carrier for the composites. All carrier samples were crushed to a 0.1–0.3 mm fraction using sieves, pre-washed several times with distilled water to remove water-soluble impurities and easily dispersible clay impurities, and dried in an oven at 90 °C. Samples that did not undergo further processing are designated D1. The next subset of samples were calcined at 500 °C for 3 hours, washed again with distilled water, and dried in an oven at 90 °C (D2). The third part of the carriers was washed with a 10 % HCl solution to remove impurities of carbonates, oxides and hydroxides of alkaline earth metals and iron, then washed with distilled water until a neutral reaction and dried in a drying oven at 90 °C (D3). The fourth part of the samples was washed with a 10 % HCl solution, then washed with distilled water until a neutral reaction, dried in a drying oven at 90 °C, calcined at 500 °C for 3 hours and again washed with distilled water and dried at 90 °C (D4).

2.1.2. Synthesis of composites by low-temperature combustion

The support samples prepared in accordance with section 2.1.1 were impregnated with a mixture of cobalt nitrate hydrate solutions $Co(NO_3)_2{\cdot}6H_2O$ and manganese $Mn(NO_3)_2{\cdot}4H_2O$ (oxidizers), and urea $CO(NH_2)_2$ (reducing agent, fuel). The required amount of precursors to obtain a composite containing 5 wt. % of Co and 5 % wt. % of Mn (calculated as metals) was calculated using the following equation:

$$Co(NO_3)_2{\cdot}6H_2O + Mn(NO_3)_2{\cdot}4H_2O + 4CO(NH_2)_2 \rightarrow$$
$$\rightarrow Co + Mn + 4CO_2 + 5N_2 + 18H_2O. \quad (1)$$

Thus, the maximum amount of reducing agent (urea) was introduced into the precursor mixture, sufficient to obtain the fully reduced (metallic) phases of Co and Mn. This limiting case is far from always realized; a mixture of metallic and oxide phases [29], or even oxide phases alone, was often obtained. In any case, unreacted fuel was simply washed from the sample. The proposed metal content is the minimum possible for achieving stable low-temperature combustion.

The calculated amounts of nitrates and urea were dissolved in a minimal amount of water at room temperature, and the carrier samples were impregnated with the resulting solution while stirring. After drying in a drying oven at 90 °C, 10 g of the samples were placed in a combustion reactor assembled according to the diagram in Fig. 1.

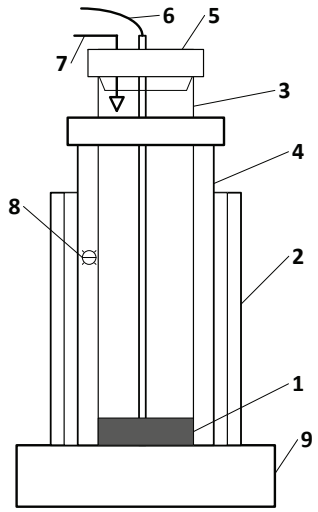

Fig. 1. A diagram of the experimental setup for synthesis in the low-temperature combustion mode: *1* – sample; *2* – heat-insulating casing with a viewing window; *3* – tubular quartz reactor with a flat bottom; *4* – quartz glass with a lid; *5* – dust collection system; *6* – thermocouple; *7* – argon supply; *8* – backlight lamp; *9* – electric heater

Throughout the experiment, the reactor was purged with argon. The reactor bottom heater was turned on and its power remained constant throughout the entire process. Temperature was monitored with a thermocouple placed in the sample layer at the center of the reactor bottom. Thermocouple readings were entered into a computer using a Metex ME-31 digital multimeter (Metex, Korea), and thermograms of the process were plotted as a temperature-time dependence. The sample combustion reaction began at a random point near the reactor perimeter and proceeded as a combustion wave, appearing as a darkening wave accompanied by intense gas evolution and dust emission above the sample layer. After cooling, the sample in the reactor under argon was stabilized with a 5 % H_2O_2 solution to prevent spontaneous combustion of any highly dispersed metallic phases in the active phase. The sample was then rinsed with distilled water and then dried at 90 °C. The fraction < 0.1 mm was removed from the resulting product by sifting on a sieve.

The prepared samples have the following designations: 5Co5Mn/D1, 5Co5Mn/D2, 5Co5Mn/D3, 5Co5Mn/D4. The numbers before the names of the elements indicate their content in the composites in wt. %, calculated as metal.

2.2. Physicochemical studies of samples

The X-ray diffraction (XRD) analysis of the samples was performed on a DRON-3M diffractometer (Russia), using FeKα radiation. Surface morphology and elemental composition were analyzed using a scanning electron microscope with an EDS attachment (SEM/EDS) (Zeiss Ultra plus microscope + INCA Energy 350 XT energy-dispersive spectrometer). Specific surface area was measured using a dedicated laboratory setup designed and constructed according to the design and methodology of Russian Standard 23401-90, using a multipoint scheme at liquid nitrogen temperature. Specific surface area was calculated using the BET method.

3. Results and Discussion

Figure 2 shows thermograms of the synthesis processes of composite samples on all types of supports. T_S denotes the point of temperature rise at the front of the combustion wave incident on the thermocouple, when the heat release from the chemical reaction begins to exceed the external heat input. In essence, this value is close to the autoignition temperature. The T_S values are quite close for all samples. Tmax correspond to the maximum temperatures in the combustion wave; the spread of their values is more significant (~50 °C). The splitting of the maximum temperature peaks (Fig. 2) was previously observed in the case of the synthesis of Co-Mn/γAl_2O_3 catalysts [29] and was explained as the passage of combustion and afterburning waves associated with the heterogeneity of the porous structure of the samples and the complex mechanism of the process, including the autocatalytic action of newly formed oxo-metallic phases.

The X-ray diffraction results for the support and composite samples are shown in Fig. 3. As can be seen, the diffraction patterns of both the support and the resulting composites show only peaks corresponding to three different SiO_2 modifications: quartz, cristobalite, and tridymite. Thus, support activation and composite synthesis do not significantly affect their phase structure. Co- and Mn-containing phases were not detected, apparently due to their content being below the detection limit of the method (~5 %) and the significant amorphous nature of the support.

In order to study the phase composition of the cobalt-manganese phase, the samples of 5Co5Mn/D1 and 5Co5Mn/D2 composites were boiled for 1 hour in a 20 % NaOH solution according to our previously proposed method [29], washed with distilled water until a neutral reaction was achieved, and dried at 90 °C. As a result, the amorphous component of the carriers dissolved, increasing the content of the Co-Mn component in the residue. The mass loss of the 5Co5Mn/D2 sample was 55.47 %, while that of the 5Co5Mn/D4 sample was 58.27 %. The X-ray diffraction results of the leached composite samples are shown in Fig. 4.

As can be seen, the next phase, $Co_xMn_yO_z$, is observed. This phase is a mixed oxide, meaning that reduction during combustion according to reaction (1) is incomplete.

The results of specific surface area measurements for the initial and activated support samples, as well as the Co-Mn-containing composites based on them, are shown in the histogram in Fig. 5.

As can be seen, the processing processes affect the specific surface area differently compared to the original diatomite sample. A slight decrease is observed only during the initial calcination of the diatomite, but the acid treatment and calcination processes lead to a significant increase in the specific surface area, reaching a maximum in the case of sample D4.

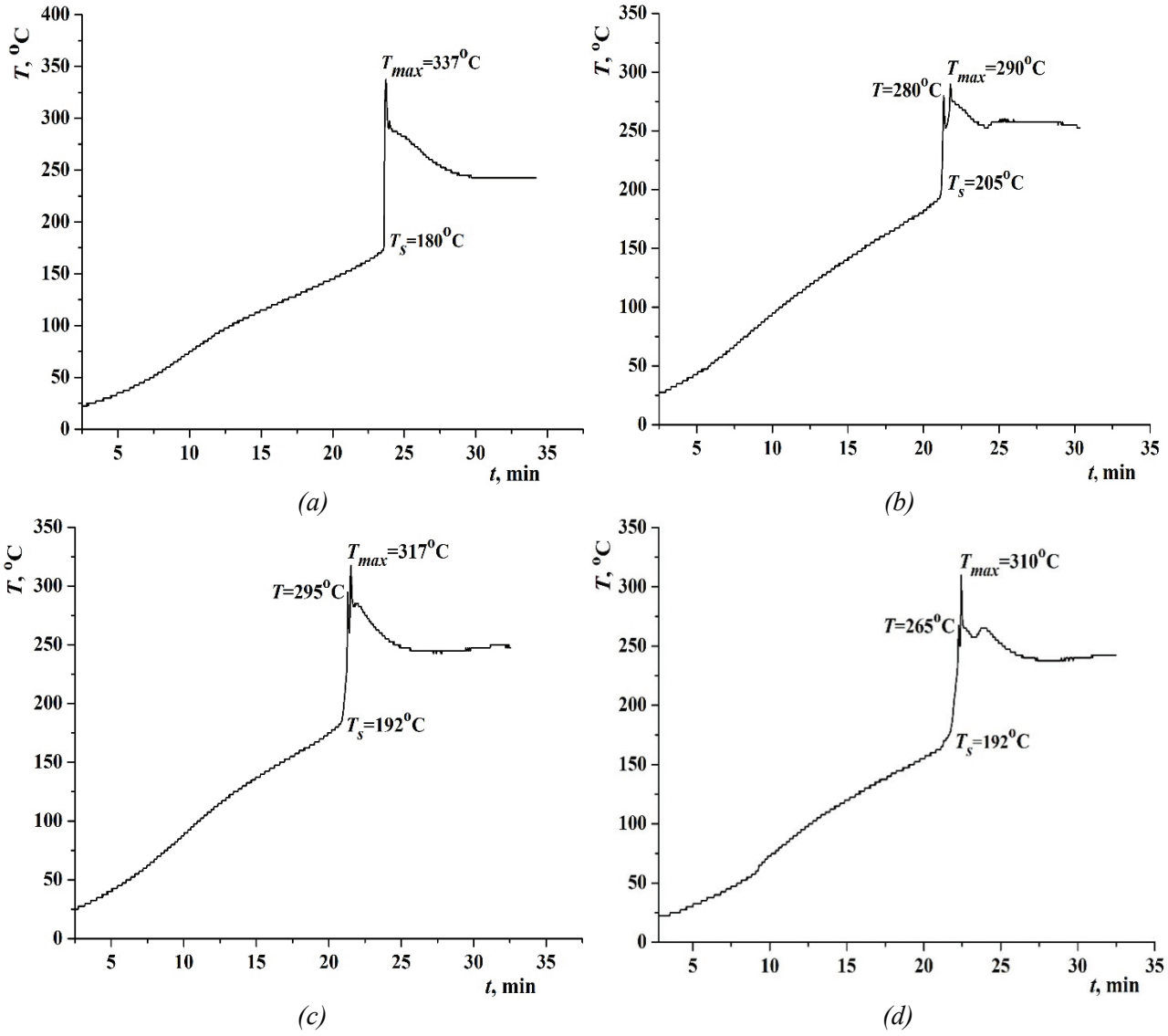

Fig. 2. Thermograms of the composite's synthesis process:
a – 5Co5Mn/D1; *b* – 5Co5Mn/D2; *c* – 5Co5Mn/D3; *d* – 5Co5Mn/D4

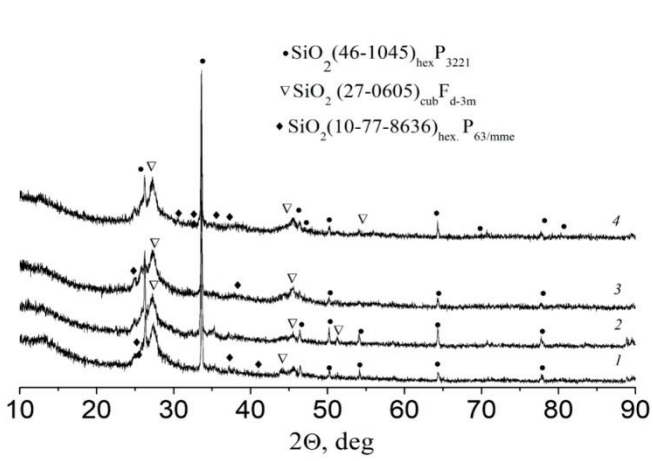

Fig. 3. XRD-patterns of samples:
1 – D1; *2* – D2; *3* – 5Co5Mn/D1; *4* – 5Co5Mn/D2

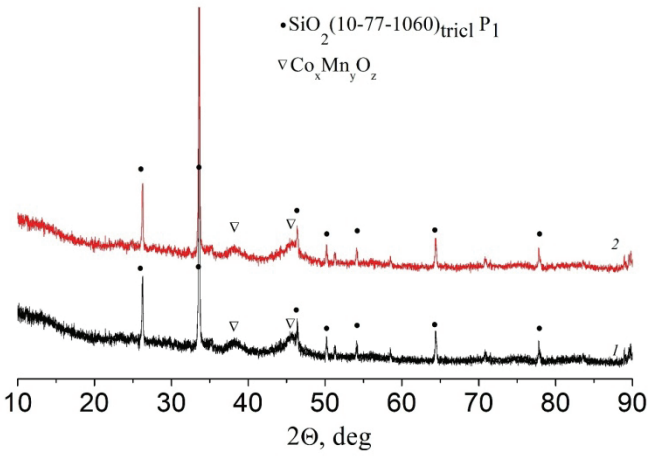

Fig. 4. XRD-patterns of leached composite samples:
1 – 5Co5Mn/D2; *2* – 5Co5Mn/D4

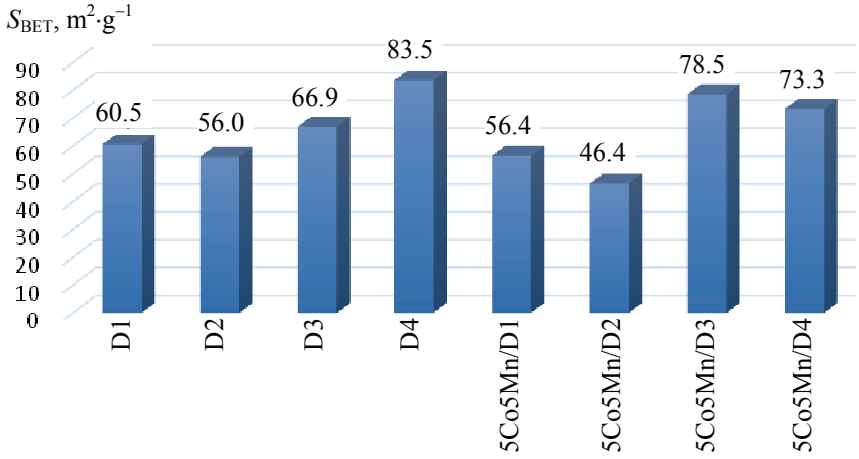

Fig. 5. Histogram of specific surface area values of support and composite samples

This is likely due to the opening of small pores in the support. The application of the Co-Mn-containing phase leads to a nearly identical dependence of the specific surface area of the composites on the specific surface area of the supports (except for the 5Co5Mn/D3 sample), with a slight decrease in the specific surface area of the composites. This suggests that the dispersion of the metal-containing phase is somewhat lower than the characteristic pore size of the support, as a result of which some of the small pores of the support may be blocked by particles of the applied phase. It should be noted that the specific surface area of the composites obtained in this study is significantly (by approximately 15 $m^2 \cdot g^{-1}$) higher than that of the 5Co5Mn/flask composites obtained by us previously [36], which demonstrated high catalytic activity in the process of deep oxidation of CO and propane. It should be noted that flasks are similar in composition and structure to diatomite, so it can be expected that diatomite-based composites will also exhibit high catalytic activity.

The results of the elemental analysis of the surface of composite granules according to SEM/EDS data at points in Figs. 6 and 7 are presented in Tables 1 and 2.

According to Table 2, significant levels of impurity elements (Na, K, Mg, Ca, Al, and Fe) are observed in both the carrier and finished composite samples. This is related to the natural origin of diatomite and depends on the specific deposit. The highest concentrations are indicated for iron-containing phases, which impart a characteristic reddish-brown hue to the original diatomite samples.

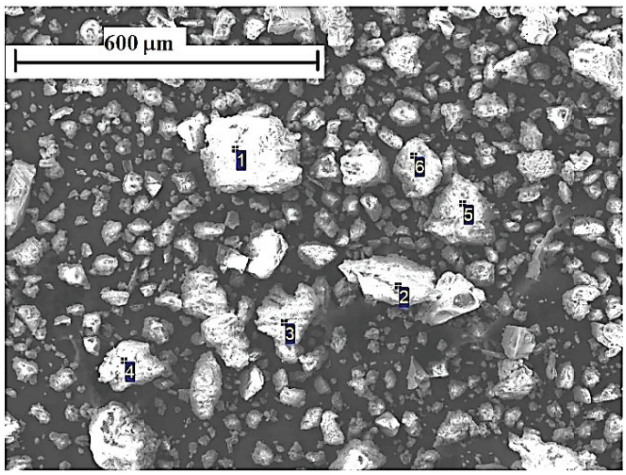

Fig. 6. SEM-image of D2 sample

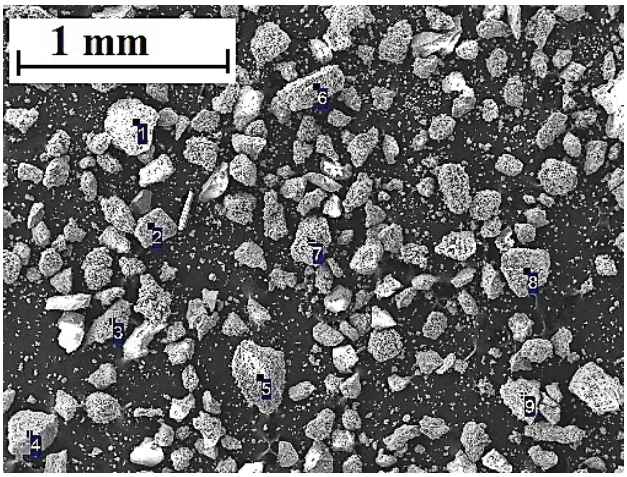

Fig. 7. SEM-image of catalyst sample 5Co5Mn/D2

Table 1. Elemental composition of the surface (wt. %) of the D2 sample in the points in Fig. 6

Point number	Elements, wt. %						
	O	Mg	Al	Si	K	Ca	Fe
1	31.91	0.52	1.50	41.16	2.36	1.32	21.23
2	35.75	0.42	1.88	21.96	0.95	0.56	38.48
3	58.40	0.58	4.64	32.79	1.32	0.42	1.85
4	49.14	0.56	4.57	40.25	1.63	0.73	3.12
5	67.28	0.13	1.87	29.62	0.42	0.23	0.45
6	63.19	0.44	2.66	32.08	0.62	0.30	0.67
Mean	51.08	0.44	2.85	33.05	1.22	0.60	10.76

Table 2. Elemental composition of the surface (wt. %) of the 5Co5Mn/D2 sample in the points in Fig. 7

Point number	Elements, wt. %										
	O	Na	Mg	Al	Si	K	Ca	Ti	Mn	Fe	Co
1	57.25	0.60	0.43	3.44	28.05	0.54	0.55	0.77	3.78	1.04	3.55
2	24.47	0.00	0.10	2.65	13.07	1.12	0.85	0.44	25.55	1.37	27.39
3	56.16	0.13	0.31	2.02	29.33	0.33	0.55	0.15	5.05	0.97	5.00
4	11.82	0.00	0.18	1.45	10.84	1.48	1.58	0.95	32.25	6.52	32.93
5	54.50	0.20	0.31	1.95	23.76	0.52	0.65	0	8.28	1.74	8.12
6	33.74	0.08	0.26	3.32	34.75	0.97	0.80	0.05	11.53	2.24	12.25
7	18.87	0.00	0.08	2.09	11.24	0.10	0.64	0.00	29.16	6.73	31.09
8	29.46	0.30	0.65	3.03	28.79	0.62	2.04	0.82	14.89	7.51	12.26
9	5.07	0.00	0.11	2.77	4.95	0.60	2.19	0.00	31.52	12.86	39.94
Mean	32.37	0.15	0.23	2.55	20.47	0.69	1.09	0.35	18.13	4.92	19.17

Note the wide range of concentrations of cobalt- and manganese-containing phases on the surface of various composite granules, apparently related to the varying absorption of the initial precursor solution by the individual granules. This absorption, in turn, depends on the wettability and pore structure of the individual granules, which varies greatly due to the structural heterogeneity of natural minerals. This heterogeneity manifests itself when the carrier is crushed into granules of different types. Even visually, Figs. 6 and 7 reveal granules with a denser surface and granules that are essentially conglomerates of small particles. However, the higher average Co and Mn contents, compared to the calculated values, indicate that the metal-containing phases are concentrated primarily on the outer surface of the granules. The surface morphology of the composite granules is shown in more detail in Fig. 8.

To study the surface morphology of the composite in Fig. 8, composite granules based on two main types of carrier granules were selected. Granules of the first type (Fig. 8*a*) are denser, layered, and covered with micron-sized crystallites. However, at the nanoscale, a flaky surface structure appears, with characteristic flake sizes < 200 nm. The composition of these morphological elements, due to their size, cannot be analyzed by EDS. Since the specific surface area of this composite sample is smaller than that of its carrier (see Fig. 5), the morphology of the metal-containing phase can be associated with the noted micron-sized crystallites on the surface. Granules of the second type (Fig. 8*b*) have the appearance of loose breccia-type conglomerates; however, at the nanoscale, in contrast to granules of the first type, their stepped surface is smoother and permeated with nanopores. No details that could be associated with the deposited phase are observed at this level.

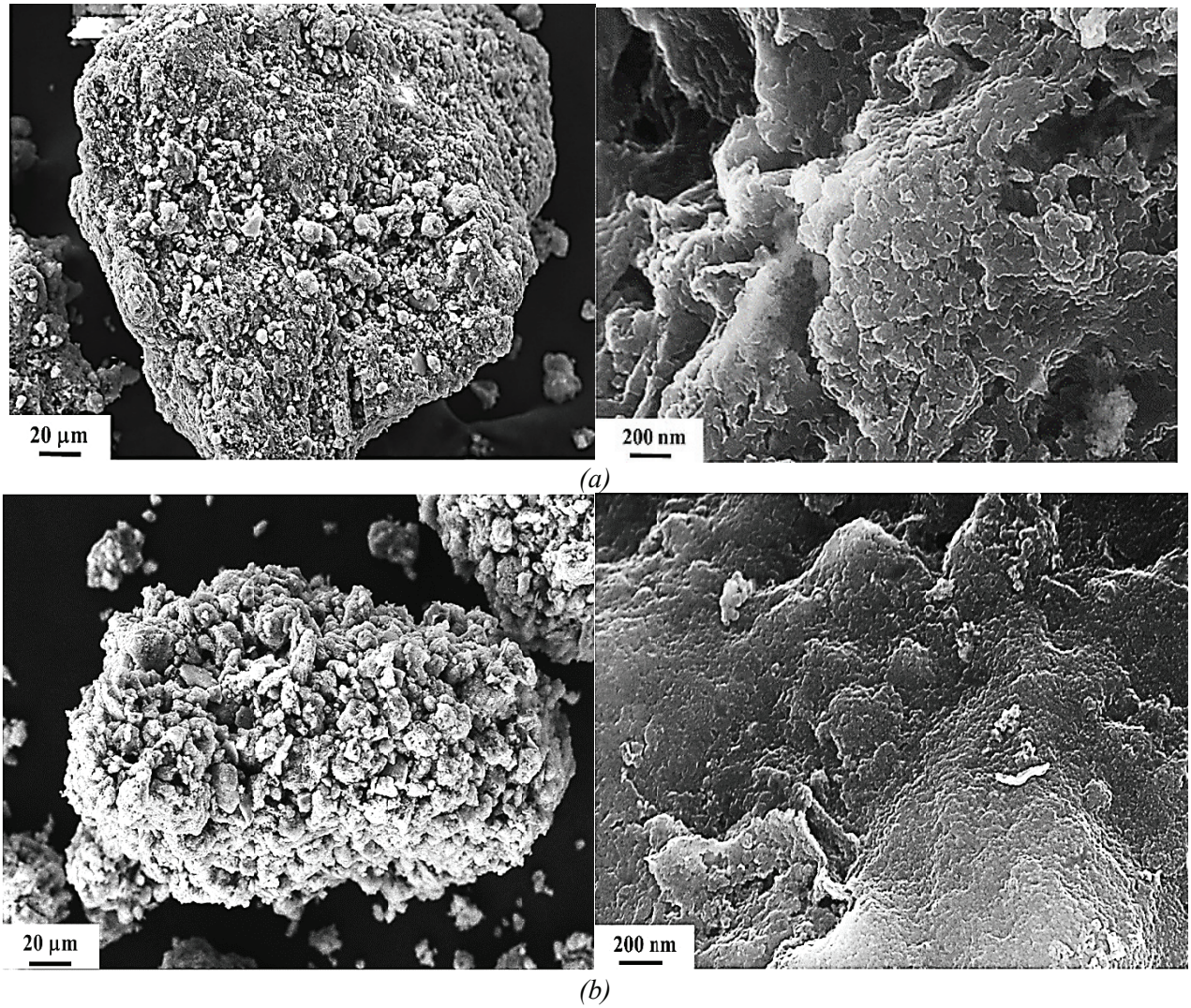

Fig. 8. SEM-images of two 5Co5Mn/D2 composite granules of different structure

4. Conclusion

Composite materials with a deposited Co-Mn-containing phase were obtained using low-temperature combustion on the basis of natural and activated diatomite samples. These materials were then used as catalysts in the deep oxidation of CO and hydrocarbons. In addition to the original diatomite (D1), three types of activated diatomites were obtained: those calcined at 500 °C (D2), those treated with an HCl solution (D3), and those treated with an HCl solution and then calcined at 500 °C (D4). Synthesis of the composites by low-temperature combustion included the following steps: impregnation of the diatomite samples with solutions of Co and Mn nitrates (oxidizers) and urea (reducing agent, fuel), drying, and initiation of the combustion process by heating the impregnated samples. The process was visually observed in the combustion wave mode. The maximum temperature in the combustion wave (337 °C) was recorded during the synthesis of the 5Co5Mn/D1 composite. In the thermograms of the synthesis of three composite samples, in addition to 5Co5Mn/D1, secondary peaks were observed, apparently associated with the passage of afterburning waves due to a complex, possibly autocatalytic combustion mechanism. According to XRD data, only peaks of various SiO_2 phases (quartz, tridymite, and cristobalite) were observed in the composites. The specific surface area of the composites ranged from 46.4 to 78.5 $m^2 \cdot g^{-1}$. EDS analysis revealed a significant spread in the surface concentrations of Co and Mn, mainly on two types of granules, apparently associated with the structural heterogeneity of natural diatomite. Noticeable concentrations of impurity elements, including iron, were also detected. The SEM morphology of composite granules with two different surface types was studied. Some assumptions are

made about the morphology of the Co-Mn-containing phases. The resulting composites are similar in composition to our previously synthesized 5Co5Mn/opoka composites, which demonstrated high catalytic activity in the deep oxidation of CO and propane. Since these diatomite-based composites have a significantly higher specific surface area (approximately 15 $m^2 \cdot g^{-1}$) compared to 5Co5Mn/opoka, their high catalytic activity can be assumed.

5. Funding

The study was conducted on the ISMAN state assignment.

R.I. Jussupkaliyeva is grateful to the Ministry of Science and Higher Education of the Republic of Kazakhstan for the financial support.

6. Conflict of interest

The authors declare no conflict of interest.

References

1. Smirnov PV, Konstantinov AO, Gursky HJ. Petrology and industrial application of main diatomite deposits in the Transuralian region (Russian Federation). *Environmental Earth Sciences*. 2017;76(20):682. DOI:10.1007/s12665-017-7037-3

2. YergozhinEE, Akimbayeva AM. *Organomineral sorbents and polyfunctional systems based on natural aluminosilicate and coal-mineral raw materials.* Almaty: TOO "Print-S" Publ. House; 2007. 373 p. (In Russ.)

3. Makarova I, Faizov R, Buzaeva M, Davydova O, et al. Utilization of nanomodified dispersion of lubricating coolants with the use of natural sorbents. *Bulletin of the South Ural State University series "Chemistry"*. 2017;9(2):5-12. DOI:10.14529/chem170201

4. Aivalioti M, Papoulias P, Kousaiti A, Gidarakos E. Adsorption of BTEX, MTBE and TAME on natural and modified diatomite. *Journal of Hazardous Materials*. 2012;207-208:117-127. DOI:10.1016/j.jhazmat.2011.03.040

5. Xie F, Wu F, Liu G, Mu Y, et al. Removal of phosphate from eutrophic lakes through adsorption by in situ formation of magnesium hydroxide from diatomite. *Environmental Science & Technology*. 2014;48(1):582-590. DOI:10.1021/es4037379

6. Ma T, Wu Y, Liu N, Wu Y. Hydrolyzed polyacrylamide modified diatomite waste as a novel adsorbent for organic dye removal: adsorption performance and mechanism studies. *Polyhedron*. 2020;175:114227. DOI:10.1016/j.poly.2019.114227

7. Tao X, Wu Y, Sha H. Cuprous oxide-modified diatomite waste from the brewery used as an effective adsorbent for removal of organic dye: adsorption performance, kinetics and mechanism studies. *Water, Air, & Soil Pollution*. 2018;229(10):322. DOI:10.1007/s11270-018-3977-9

8. Rudakov VM, Agladze MG, Kolpakova EE, Kazakov JuM, Davydova GI. Polymerization of ethylene on the surface of diatomites and other natural silica rocks activated by an organoaluminum compound. *Vysokomolekulyarnye soedineniya. Seriya B.* 1992;34(5): 37-43. (In Russ.)

9. Nazhipkyzy M, Nemkayeva RR, Nurgain A, Seitkazinova AR, et al. The use of diatomite as a catalyst carrier for the synthesis of carbon nanotubes. *Nanomaterials*. 2022;12(11):1817. DOI:10.3390/nano12111817

10. Agabekov VE, Sen'kov GM, Sidorenko AYu, Tuyen ND, et al. New α-pinene isomerization catalysts. *Catalysis in Industry*. 2011;3(4):319-330. DOI:10.1134/S2070050411040027

11. Toshtay K, Auezov AB. Hydrogenation of vegetable oils over a palladium catalyst supported on activated diatomite. *Catalysis in Industry*. 2020;12(1):7-15. DOI:10.1134/S2070050420010109

12. Liang L, Miao C, Ke X, Peng Y, et al. A superior strategy for CO_2 methanation under atmospheric pressure: organic acid-assisted co nanoparticles assembly on diatomite. *Fuel*. 2023;351:128931. DOI:10.1016/j.fuel.2023.128931

13. Liu Q, Li M, Wang S, Lv S, et al. Ultrathin 3D CoMn nanoflowers coupled diatomite for highly efficient catalytic oxidation of CO and propane. *Chemical Engineering Journal*. 2023;477:147102. DOI:10.1016/j.cej.2023.147102

14. Zhang X, Shen J, Sun H, Gong Y, et al. Room temperature oxidation of formaldehyde using TiO_2/recycled diatomite composite. *Journal of the Minerals, Metals & Materials Society*. 2022;74(7):2716-2723. DOI:10.1007/s11837-022-05224-0

15. Han Z, Wang C, Zou X, Chen T, et al. Diatomite-supported birnessite-type MnO_2 catalytic oxidation of formaldehyde: preparation, performance and mechanism. *Applied Surface Science*. 2020;502:144201. DOI:10.1016/j.apsusc.2019.144201

16. Yang Y, Zhang Z, Li Y, Wang R, et al. The catalytic aerial oxidation of As(III) in alkaline solution by Mn-loaded diatomite. *Journal of Environmental Management*. 2022;317:115380. DOI:10.1016/j.jenvman.2022.115380

17. Matskan PA, Evdokimova EV, Mamontov GV. MIL-100(Fe)/diatomite composites for photo-fenton

degradation of phenol. *Kinetika ikataliz = Kinetics and Catalysis*. 2023;64(4):418-427. DOI:10.31857/S045388112304007X (In Russ.)

18. Dai N, Yi S, Zhang X, Feng L, et al. Typical synthesis of an iron-modified laponite @diatomite composite for photo-fenton degradation of methyl orange dyes. *Applied Surface Science*. 2023;607:154886. DOI:10.1016/j.apsusc.2022.154886

19. Ge Y, Xu HQ, Huang Q, Jia X, et al. Microwave-assisted synthesis of Ag/ZnO/diatomite composites for photocatalytic degradation of gaseous toluene. *Inorganic Chemistry Communications*. 2025;171:113543. DOI:10.1016/j.inoche.2024.113543

20. Rezig W, Elaziouti A, Laouedj N, Hadjel M. Synthesis and characterization of novel calcined ferrihydrite-modified diatomite (FMD3X6) and its UVA light-assisted heterogeneous photodegradation of VG3 dye. *Desalination and Water Treatment*. 2022;271:254-271. DOI:10.5004/dwt.2022.28719

21. Datsko TY, Zelentsov VI. Hybrid nano-titanium dioxide/diatomite photocatalyst for advanced oxidation processes (AOPs) mediated removal of toxic organic pollutants. *Chemical Safety Science.* 2020;4(2):101-116. DOI:10.25514/CHS.2020.2.18007

22. Xu H, Wang H, Wang X, Tang Z, et al. Fluidized bed photobioreactor based on diatomite powder and high light intensity improved microalgae harvesting, nutrient removal and lipid accumulation: Performance and microscopic mechanism. *Water Research*. 2024;264:122172. DOI:10.1016/j.watres.2024.122172

23. Borshch VN, Zhuk SYa, Vakin NA, Smirnov KL, et al. Sialons as a new class of supports for oxidation catalysts. *Doklady Physical Chemistry*. 2008;420(2):121-124. DOI:10.1134/S0012501608060018

24. Zav'yalova UF, Tret'yakov VF, Burdeinaya TN, Lunin VV, et al. Self-propagating synthesis of supported oxide catalysts for deep oxidation of CO and hydrocarbons. *Kinetics and Catalysis*. 2005:46(5):752-757. DOI:10.1007/s10975-005-0132-6

25. Zavyalova U, Scholz P, Ondruschka B. Influence of cobalt precursor and fuels on the performance of combustion synthesized Co_3O_4/γ-Al_2O_3 catalysts for total oxidation of methane. *Applied Catalysis A: General*. 2007:323:226-233. DOI:10.1016/j.apcata.2007.02.021

26. Kotolevich YS, Khramov EV, Mironenko OO, Zubavichus YaV, et al. Supported palladium catalysts prepared by surface self-propagating thermal synthesis. *International Journal of Self-Propagating High-Temperature Synthesis*. 2014;23(1):9-17. DOI:10.3103/S1061386214010075

27. Smagulova GT, Prikhod'ko NG, Guseinov NR, Nemkayeva R, et al. Zeolite based catalysts for synthesis of carbon nanotubes. *Goreniye i plazmoximia*. 2016;14(2):83-88. (In Russ.)

28. Kotolevich YS, Mamontov GV, Vodyankina OV, et al. Catalytic Pd-Ag nanoparticles immobilized on fiber glass by surface self-propagating thermal synthesis. *International Journal of Self-Propagating High-Temperature Synthesis*. 2017;26:234-239. DOI:10.3103/S1061386217040045

29. Borshch VN, Dement'eva IM, Khomenko NYu. Supported polymetallic catalysts by self-propagating surface synthesis. *International Journal of Self-Propagating High-Temperature Synthesis*. 2019;28(1):45-49. DOI:10.3103/S1061386219010059

30. Borshch VN, Bystrova IM, Pugacheva EV, Smirnova EM, et al. Low-temperature combustion synthesis of halloysite-based catalysts for the deep oxidation of hydrocarbons and carbon monoxide and the methanation of carbon dioxide. *Kinetics and Catalysis*. 2022;63(6):801-812. DOI:10.1134/S0023158422060027

31. Borshch VN, Bystrova IM, Pugacheva EV, Khomenko NYu. Hydrogenation of CO_2 on Co-Ni catalysts produced by low-temperature combustion using modified silica fabric. *International Journal of Self-Propagating High-Temperature Synthesis*. 2023;32(4):302-312. DOI:10.3103/S1061386223040131

32. Borshch VN, Bystrova IM, Boyarchenko OD, Khomenko NYu, et al. Low-temperature combustion synthesis and characterization of Co-containing catalysts based on modified silica gel. *International Journal of Self-Propagating High-Temperature Synthesis*. 2023;32(2):126-138. DOI:10.3103/S1061386223020024

33. Li G, Li N, Sun Y, Qu Y, et al. Efficient defect engineering in Co-Mn binary oxides for low-temperature propane oxidation. *Applied Catalysis B: Environmental*. 2021;282:119512. DOI:10.1016/j.apcatb.2020.119512

34. Shan C, Zhang Y, Zhao Q, Li J, et al. New insight into opposite oxidation behavior in acetone and propane catalytic oxidation over CoMn based spinel oxides. *Chemical Engineering Journal*. 2023;476:146550. DOI:10.1016/j.cej.2023.146550

35. Zhao H, Wang H, Qu Z. Synergistic effects in Mn-Co mixed oxide supported on cordierite honeycomb for catalytic deep oxidation of VOCs. *Journal of Environmental Sciences*. 2022;112:231-243. DOI:10.1016/j.jes.2021.05.003

36. Jussupkaliyeva RI, Bystrova IM, Pomogailo SI, Borshch VN. Synthesis of Co-Mn catalysts for deep oxidation of CO and propane based on natural opoka by low-temperature combustion. *Izvestiya vysshikh uchebnykh zavedeniy. Poroshkovaya metallurgiya i funktsional'nye pokrytiya = Powder Metallurgy and Functional Coatings.* 2024;18(6):17-27. DOI:10.17073/1997-308X-2024-6-17-27 (In Russ.)

Information about the authors / Информация об авторах

Roza I. Jussupkaliyeva, Senior Lecturer, Zhangir Khan West Kazakhstan Agrarian Technical University, Uralsk, Republic of Kazakhstan; ORCID 0000-0001-8916-0008; e-mail: Rozaid2@mail.ru

Vyacheslav N. Borshch, Cand. Sc (Chem.), Leading Researcher, Merzhanov Institute of Structural Macrokinetics and Materials Science RAS (ISMAN), Chernogolovka, Russian Federation; ORCID 0000-0001-5827-4942; e-mail: borsch @ism.ac.ru

Inna M. Bystrova, Junior Research Fellow, ISMAN, Chernogolovka, Russian Federation; ORCID 0000-0003-3739-7390; e-mail: inna2019@ism.ac.ru

Elena V. Pugacheva, Cand. Sc (Chem.), Senior Researcher, ISMAN, Chernogolovka, Russian Federation; ORCID 0000-0002-4354-8776; e-mail: help@ism.ac.ru

Natalia Yu. Khomenko, Senior Researcher, ISMAN, Chernogolovka, Russian Federation; ORCID 0000-0001-9388-7365; e-mail: khomenko@ism.ac.ru

Artem V. Rukhov, D. Sc. (Eng.), Professor, Head of the Department, Tambov State Technical University, Tambov, Russian Federation; ORCID 0000-0001-9194-8099; e-mail: rukhov.av@gmail.com

Svetlana I. Pomogailo, Cand. Sc. (Chem.), Senior Researcher, ISMAN, Chernogolovka, Russian Federation; Senior Researcher, All-Russian Institute for Scientific and Technical Information, Moscow, Russian Federation ORCID 0000-0001-8200-0706; e-mail: pom_lana@ism.ac.ru

Джусупкалиева Роза Ибраимовна, старший преподаватель, Западно-Казахстанский аграрно-технический университет имени Жангир хана, Уральск, Республика Казахстан; ORCID 0000-0001-8916-0008; e-mail: Rozaid2@mail.ru

Борщ Вячеслав Николаевич, кандидат химических наук, ведущий научный сотрудник, Институт структурной макрокинетики и проблем материаловедения им. А. Г. Мержанова РАН (ИСМАН), Черноголовка, Российская Федерация; ORCID 0000-0001-5827-4942; e-mail: borsch @ism.ac.ru

Быстрова Инна Михайловна, младший научный сотрудник, ИСМАН, Черноголовка, Российская Федерация; ORCID 0000-0003-3739-7390; e-mail: inna2019@ism.ac.ru

Пугачева Елена Викторовна, кандидат химических наук, старший научный сотрудник, ИСМАН, Черноголовка, Российская Федерация; ORCID 0000-0002-4354-8776; e-mail: help@ism.ac.ru

Хоменко Наталья Юрьевна, старший научный сотрудник, ИСМАН, Черноголовка, Российская Федерация; ORCID 0000-0001-9388-7365; e-mail: khomenko@ism.ac.ru

Рухов Артём Викторович, доктор технических наук, профессор, заведующий кафедрой, Тамбовский государственный технический университет, Тамбов, Российская Федерация; ORCID 0000-0001-9194-8099; e-mail: rukhov.av@gmail.com

Помогайло Светлана Ибрагимовна, кандидат химических наук, старший научный сотрудник, ИСМАН, Черноголовка, Российская Федерация; старший научный сотрудник, Всероссийский институт научной и технической информации РАН, Москва, Российская Федерация ORCID 0000-0001-8200-0706; e-mail: pom_lana@ism.ac.ru

Received 30 May 2025; Revised 25 July 2025; Accepted 07 August 2025

Original papers
Manufacturing processes and systems

УДК 621.6.04.001.5 DOI: 10.17277/jamt-2025-10-04-301-312

Phenomenology of clustering and separation effects in granular media under vibration impact in microgravity conditions

© Viktor N. Dolgunin[a]✉, Konstantin A. Kudi[b], Andrey A. Zhilo[a]

[a] *Tambov State Technical University, Bld. 2, 106/5, Sovetskaya St., Tambov, 392000, Russian Federation,*
[b] *JSC "BCS Bank", Bld. 1, 69, Mira Av. Moscow, 125047, Russian Federation*

✉ dolgunin-vn@yandex.ru

Abstract: The paper provides the phenomenological description of the effects of cluster formation and separation of cohesionless spherical particles by size and density in a bed of a rarefied granular medium under the action of vibrations in microgravity conditions. Mathematical modeling of the structural and kinematic parameters of the granular medium is performed based on its equation of state as a "gas of solid particles". It is established that the condition for particle cluster formation is sufficiently high values of the solid phase fraction and the thickness of the vibrating bed, at which the quasi-thermal vibration flux has a limited area of active penetration into the bed volume. The separation process is a consequence of the quasi-diffusion interaction of particles with different fluctuation velocity in the presence of a gradient in the fraction of voids in the granular medium. The distribution of particles of a binary mixture of varying sizes was simulated using the separation dynamics equation, which describes the transport of non-uniform particles as a result of the coupling of quasi-diffusion separation and mixing fluxes. The simulation results are compared with experimental data obtained with support from the European Space Agency (Parabolic Flight Campaign PFC64) using the VIP-Gran instrument.

Keywords: granular material; microgravity; vibration; clustering; quasi-diffusion separation by size and mass; mixing; granular temperature.

For citation: Dolgunin VN, Kudi KA, Zhilo AA. Phenomenology of clustering and separation effects in granular media under vibration impact in microgravity conditions. *Journal of Advanced Materials and Technologies*. 2025;10(4):301-312. DOI: 10.17277/jamt-2025-10-04-301-312

Феноменология эффектов кластеризации и сепарации в зернистых средах при вибрационном воздействии в условиях микрогравитации

© В. Н. Долгунин[a]✉, К. А. Куди[b], А. А. Жило[a]

[a] *Тамбовский государственный технический университет,*
ул. Советская, 106/5, пом. 2, Тамбов, 392000, Российская Федерация,
[b] *АО «БКС Банк», пр. Мира, 69, стр. 1, Москва, 125047, Российская Федерация*

✉ dolgunin-vn@yandex.ru

Аннотация: Предложено феноменологическое описание эффектов формирования кластеров и сепарации несвязных сферических частиц по размеру и плотности в слое разреженной зернистой среды под действием вибраций в условиях микрогравитации. Проведено математическое моделирование структурно-кинематических параметров зернистой среды на базе уравнения ее состояния как «газа твердых частиц», в результате которого установлено, что условием формирования кластера частиц являются достаточно высокие значения доли твердой фазы и толщины вибрирующего слоя, при которых квазитепловой поток вибрации имеет ограниченную область активного проникновения в объем слоя. Процесс сепарации является следствием квазидиффузионного взаимодействия частиц, имеющих различную скорость флуктуаций при наличии градиента доли пустот в объеме зернистой среды. Моделирование распределения частиц бинарной смеси, различающихся по размеру, проведено с использованием уравнения динамики сепарации, описывающего процесс переноса неоднородных частиц как

результат сопряжения квазидиффузионных потоков сепарации и перемешивания. Результаты моделирования приведены в сравнении с экспериментальными данными, полученными при поддержке европейского космического агентства (Parabolic Flight Campaign PFC64) с использованием прибора VIP-Gran.

Ключевые слова: зернистый материал; микрогравитация; вибрация; кластеризация; квазидиффузионная сепарация по размеру и массе; перемешивание; температура зернистой среды.

Для цитирования: Dolgunin VN, Kudi KA, Zhilo AA. Phenomenology of clustering and separation effects in granular media under vibration impact in microgravity conditions. *Journal of Advanced Materials and Technologies*. 2025;10(4):301-312. DOI: 10.17277/jamt-2025-10-04-301-312

1. Introduction

The study of small celestial bodies (asteroids and planetoids) in the Solar System is of continuing interest, both from scientific and practical perspectives [1–5]. On the one hand, the research results allow us to come closer to explaining the mechanisms underlying the origin of the planetary system [2–7] and life on Earth, and, on the other hand, to predict ways to expand the existing resource base with sources of rare earth elements and water. A comprehensive overview of the interdisciplinary findings on various aspects of small celestial bodies, conducted using analytical and experimental methods, including DEM modeling, various types of astronomical observations, and space missions, is presented in a review paper prepared by a large international team of authors [1]. A significant portion of this paper is devoted to the analysis of these celestial bodies as granular systems from the standpoint of classical mechanics and condensed matter physics, with the goal of identifying fundamental differences in their behavior under microgravity conditions.

In this regard, the behavior of non-uniform granular materials under conditions of minimal gravitational influence has attracted increasing attention over time [8–13]. The relevance of this research is confirmed by the expanding range of cognitive and practical problems associated with the exploration and development of near and deep space. In near-space environments, granular media, such as the regolith covering the surface of the Moon and hundreds of thousands of planetoids in the Solar System, can serve as a building material for space constructions and, in addition, solve the problem of a shortage of unique mineral raw materials [1, 2].

Moreover, microgravity conditions appear to be extremely favorable for fundamental research into the effects of particle interactions in granular materials and their physical and mechanical properties [11], such as wave effects and the dissipative properties of materials [14, 15], problems of gas-liquid quasi-interphase transitions [11, 16], and fundamental problems in the physics of nonequilibrium states of granular media [17, 18].

This study was initiated by the results of physical and virtual experiments with granular materials consisting of spherical, cohesionless, not entirely elastic, and non-smooth particles under microgravity and vibration conditions [2]. The experiments revealed pronounced clustering effects in the granular material and identified certain patterns in the formation of heterogeneous structures. According to the authors of [2], the identified cluster structures are characterized by a non-uniform distribution of both the solid phase and non-uniform particles. They appear largely enigmatic in the absence of gravitational influence and require an explanation of the phenomenology of their physical mechanisms. The present work aims to provide a phenomenological explanation and develop a method for predicting the effects of cluster formation and non-uniform particle distributions under vibration influence on a granular medium under microgravity conditions.

2. Materials and Methods

2.1. The object of the study and its analysis

By analogy with work [2], monodisperse bronze particles and their binary mixtures with different component concentrations were used as model materials in this research. The sufficiently large particle size of the components (1 and 2 mm) allows us to characterize the model materials as non-cohesive granular media. The basic experimental information in this study was the results of physical and virtual experiments performed within the framework of work [2]. The virtual experiment was performed by simulating the displacement of particles as a result of their contact interactions during vibration oscillations using the finite element method (DEM). Under conditions of a low volume fraction of the solid phase (0.03–0.17), particle contacts are limited by their impact interactions, which are accompanied by the action of frictional forces and impact pulses. The frictional and impact pulse forces

are determined in proportion to the tangential and normal components of the relative velocity of the colliding particles, respectively.

The DEM modeling results are in good agreement with the results of a physical experiment supported by the European Space Agency (Parabolic Flight Campaign PFC64) using the VIP-Gran instrument. The instrument consists of a measuring cell loaded with granular material – a rectangular container (45 × 30 × 5 mm). The opposite sides of this container measuring 30 × 5 mm function as pistons and oscillate harmonically in antiphase with a frequency of 20 Hz and an amplitude of 3 mm.

The experiments revealed that at a small cell load of large particles (80 pcs.) with a solids fraction of $1 - \varepsilon = 0.05$ (the solids fraction is defined by the authors of this paper as the ratio of the particle volume to the cell volume) the granular medium (sample 1) behaves like a gas of solid particles. This is confirmed by the chaotic movement of the particles and, according to the authors [2], their uniform distribution throughout the volume. When the cell loading is increased to a volume fraction of $1 - \varepsilon = 0.089$, by adding a corresponding number of small particles (500 pcs.) to the cell containing large particles, a heterogeneous structure is formed in the granular medium (sample 2), with a cluster in the central zone of the cell having a high concentration of the solid phase and large particles. Conversely, the cell regions located near the vibrating surfaces are characterized by a low solid phase content and a high concentration of small particles. An increase in the volume fraction of the solid phase and the concentration of large particles in the cell leads to the cluster volume in its central zone increasing practically proportionally to the volume of the added particles. It is important to note that, according to visual analysis of the experimental data, in cells loaded with non-uniform particles, the zones bordering the vibrating surfaces contain exclusively small particles in a gaseous state of solid particles with an approximately equal distribution of their concentration in the direction of vibration.

2.2. Selection of research method and object of the study

The shortcomings of traditional methods of mathematical modeling of granular media dynamics based on finite element analysis (DEM) [19, 20] and the continuum approach [21, 22] fundamentally limit their predictive capabilities and are a factor determining the need to develop phenomenological models [20, 23]. According to [19, 24], phenomenological models of granular media dynamics require intensive development.

This paper develops a phenomenological model of the dynamics of the structural and kinematic parameters of a granular medium and the distribution of its non-uniform components under microgravity conditions and vibration action on it from the bounding surfaces [2]. The bounding surfaces are formed by two parallel plates, the dimensions of which, compared to the distance between them, are so large that the volume of the medium between them can be represented as an infinite plate. The surfaces perform harmonic oscillations in antiphase with complete coincidence of the vibration parameters. The listed characteristics of the object allow us to represent the problem being solved as one-dimensional and symmetrical.

The proposed phenomenological description establishes a relationship between the parameters of vibrational oscillations and a set of particle characteristics of a granular medium, with its parameters determining the conditions of dynamic particle interaction. This description is intended for use in predicting the distribution of particle fluctuation velocities and the fraction of voids (porosity) within a granular medium subjected to vibrational oscillations in the absence of gravitational influence, depending on the vibration parameters, the complex of physical and mechanical properties of the particles, and the volume fraction of the solid phase.

The description of the relationship between the structural and kinematic characteristics of a granular medium is based on the physical analogy of a granular medium in a rarefied state under conditions of weightlessness and vibrational oscillations with gas dynamics [25, 26]. The physical analogy suggests the existence of a relationship between the dilatancy of a granular medium and its pressure and granular temperature (the kinetic energy of the relative movements of particles) with a formal similarity of the relationship between the named parameters with the equation of gas dynamics:

$$p\,\bar{\varepsilon}(y) = \chi\,\theta(y), \qquad (1)$$

where p is the pressure of a granular medium (dispersion pressure according to Bagnold [27]) due to fluctuations of its particles under the action of vibrational oscillations; $\theta(y)$ is the local temperature value of the granular medium (kinetic energy of chaotic movements of particles); $\bar{\varepsilon}(y)$ is the dilatancy of the medium caused by the quasi-thermal movement of particles; χ is the coefficient of the state equation of state; y is the coordinate in the direction of vibrational oscillations.

Dilatancy of a granular medium is defined by the expression [26]

$$\bar{\varepsilon}(y) = \frac{\varepsilon(y) - \varepsilon_0}{1 - \varepsilon(y)}, \quad (2)$$

where ε_0 is the volume fraction of voids in the granular medium under stationary bed conditions, i.e., at $\theta(y) = 0$; $\varepsilon(y)$ is the local value of the fraction of voids in the volume of the medium at the nominal dispersion pressure p and granular temperature $\theta(y)$ caused by vibration action.

In defining a formal analogy between the state of a granular medium under intense relative motion of its particles and gas dynamics, the granular temperature parameter is of primary importance. In the traditional representation, temperature is expressed [28] as a parameter proportional to the averaged instantaneous value of the squared component of the particle velocity of chaotic fluctuations. In this paper, the granular temperature is represented as the kinetic energy of particles, caused by their relative motion during fluctuations during mutual collisions under the influence of vibrational oscillations [25, 26]. It should be noted that the definition of temperature as the kinetic energy of particles is used in a number of other studies [29, 30].

According to equation (1), its right-hand side expresses the kinetic energy of particles, which they possess due to their relative motion under the influence of vibrational oscillations. The left-hand side of the equation reflects the work performed by particles per unit volume of the solid phase, accompanied by the dilatancy effect, under the influence of vibrational oscillations. Consequently, the coefficient χ of the equation can be recognized as a parameter defining the relationship between the work performed by particles under the influence of vibrational oscillations, accompanied by the dilatancy effect, and the kinetic energy of the relative displacements of the particles.

Equation (1) is used to analyze the quasi-thermal effect of vibrational oscillations and the corresponding quasi-thermal flux in relation to their influence on the structural and kinematic characteristics of a granular medium and the kinetics of the mixing and separation processes of non-uniform particles. The quasi-thermal effect of vibrational action is estimated [25, 26] by local values of the kinetic energy of the particles (the temperature of the granular medium) under the assumption of the dominant role of the kinetic energy of chaotic particle fluctuations, neglecting the energy of their rotation around their own axes. This assumption is supported by the results of a study [31], according to which the role of the rotational energy of particles becomes significant only under conditions of high concentrations of "solid particle gas".

The component of the kinetic energy of particles with non-uniform density, generated by vibration and caused by the presence of a randomly distributed fluctuation velocity in the solid phase elements, is calculated as [25, 26]

$$\theta = \frac{1}{2}\rho(y)\langle V'(y)\rangle^2, \quad (3)$$

where $\rho(y)$ is the average particle density; $\langle V'(y)\rangle$ is the average absolute value of the instantaneous fluctuation velocity of conventionally uniform particles, which will be defined below as a function of the coordinate depending on the vibration parameters, the physical and mechanical properties of the particles, and the structural characteristics of the medium.

2.3. Evolution of the structural and kinematic characteristics of a granular medium under vibrational oscillations in the absence of gravity

The temperature of a granular medium θ is determined under the assumption of its properties. The granular medium is considered as a set of spherical non-smooth inelastic particles. During vibrational oscillations of the particles in the absence of gravity, the set of particles is in a state similar in physical properties to an elastic, compressible body. The validity of this assumption is substantiated by the mesoscopic properties of granular materials, according to which individual particles exhibit the properties of a solid, while a given set of particles, depending on the conditions of their interaction, can exhibit properties similar to those of substances in the liquid and gaseous states [32]. Harmonic oscillations generated in the medium by the surface bounding its volume will be accompanied by successive localized decreases and increases in volume with a frequency corresponding to the frequency of the vibrational oscillations. Successive compressions and increases in the volume of a medium are associated with the effects of supply and dissipation of quasi-thermal energy from vibrational oscillations [26].

The quasi-thermal flux $Q(y)$ generated by vibrating surfaces is expressed in accordance with the diagram shown in Fig. 1. The quasi-thermal flux emanating from the vibrating surfaces penetrates the granular medium bed, being directed opposite the

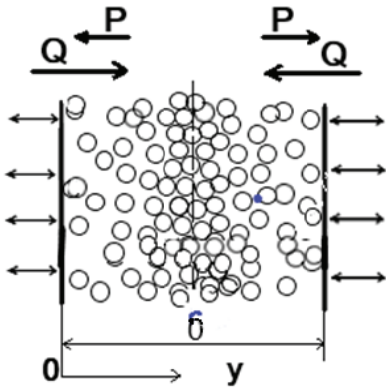

Fig. 1. Schematic diagram of quasi-thermal flux generation by vibrating surfaces in a granular medium in the absence of gravity

dispersion pressure vector p, and loses its intensity due to energy dissipation during the collision of non-smooth, inelastic particles. Quasi-thermal fluxes will be maximum near vibrating surfaces ($y = 0$), where the flux intensity is determined by the dispersion pressure of the medium and the characteristics of the vibrational oscillations.

In the presence of dissipation effects, contact between particles and the vibration source is systematically interrupted. The moment of interruption of contact between particles and the surface corresponds to the state of ultimate compression of the medium, when the surface coordinate is at its maximum. In this case, the moments of maximum compression of the granular medium will be determined as follows:

$$t_0 = \frac{n - 1 + 0.25}{\omega}, \qquad (4)$$

where n is the ordinal number and ω is the frequency of the vibrational oscillations.

At the moment of loss of contact with the surface, the medium transitions from a state of ultimate compression to a state of dilatancy. The intensity of dilatancy is determined by the velocity of the quasi-diffusion displacements of the particles. The contact of particles with the surface is resumed in the next period of oscillation in the collision mode during counter-movement. The coordinate of contact resumption and the corresponding time t_c in the oscillation period are determined by solving a system of equations describing the surface displacements in its harmonic oscillations y_v and the boundary y_m of the increasing volume of the medium in accordance with the quasi-diffusion mechanism. Assuming a small relative fraction of the volume of the medium in which contact occurs, the coordinate of contact resumption is determined by solving the system of equations:

$$y_m = A - \frac{1}{3}\langle V'(0)\rangle (t - t_0), \qquad (5)$$

$$y_v = A\sin(2\pi\omega t), \qquad (6)$$

where A is the amplitude of the vibrational oscillations ($A << \delta/2$), and $1/3\langle V'(0)\rangle$, and denotes the average value of the y – component of the particle fluctuation velocity in the granular medium adjacent to the vibrating surface.

The quasi-thermal flux generated in the granular medium by the vibrating surface can be expressed in the following integral formulation [25, 26]:

$$Q(0) = \int_{t_c}^{t_0} \omega p_y(0)\upsilon(t)dt, \qquad (7)$$

where the parameter $\upsilon(t) = 2\pi A\omega\cos(2\pi\omega t)$ determines the magnitude of the vibrating surface velocity during the oscillation period.

The dispersion pressure p_y, caused by particle fluctuations, is determined under the assumption that it is uniform in a limited volume of a rarefied granular medium in the absence of factors limiting the relaxation of internal stresses. In this case, the pressure within the volume of the granular medium can be assumed to be equal to its pressure on the vibrating surface. The magnitude of this pressure is expressed as a function of the intensity of the impulse action exerted on the granular medium by the vibrating surface. It is assumed that the change in the impulse of particles in contact with the vibrating surface during the oscillation period $1/\omega$ is equal to the impulse of the force acting on the surface. The analysis is performed under the assumption that contact between the particles and the surface occurs in a boundary bed which thickness is much smaller than the thickness of the bed of the medium enclosed between the vibrating surfaces. According to the findings in [11], this assumption ensures a stable condition for the formation of a state of the granular medium corresponding to a “gas of solid particles”.

Under this condition, the mass of particles in the boundary bed of the medium $\Delta\overline{m}(0)$ coming into contact with the vibrating surface per unit area during the oscillation period can be expressed as the product of the volume concentration of the solid phase in the boundary bed, the velocity of its quasi-diffusion movement in the direction of the vibrating surface, and the oscillation period.

$$\Delta m(0) = \overline{m}(0)(b(0)d(0))^{-3}\frac{1}{3}\langle V'(0)\rangle/\omega, \qquad (8)$$

where $\overline{m}(0)$ is the average value of the mass of a particle of a uniform granular medium in the boundary bed; $(b(0)d(0))^{-3}$ is the volume concentration of the number of particles in the boundary bed of the medium, where $b(y) = [\pi/(6(1-\varepsilon(y)))]^{0.33}$ is a geometric parameter determined depending on the local value of the void fraction $\varepsilon(y)$.

The change in the momentum of boundary bed particles is determined in accordance with the impact mechanism of their interaction with a vibrating surface. As a result of collision with the surface, particles experience an impact momentum proportional to the relative velocity of the colliding particles and the surface along the impact line. The relative velocity V_r is defined as the sum of the average values of the opposing moduli of the pre-impact velocity vectors of the normal *y* component of the quasi-diffusion flux of particles of a rarefied granular medium and a vibrating surface.

$$V_r = \frac{1}{3}\langle V'(0)\rangle + \frac{1}{t_0 - t_c}\int_{t_c}^{t_0} 2\pi A\omega\cos(2\pi\omega t)dt. \qquad (9)$$

Taking into account energy dissipation due to elastic deformations and friction [25, 26], the change in particle momentum upon collision with a unit area of the surface over one period of its oscillation is determined by the expression

$$\Delta m\Delta V_r = \Delta m(0)V_r\left(1+(1-k_E)\right)^{0.5}, \qquad (10)$$

where k_E is a parameter defining the average integral value of the portion of the particle kinetic energy that is dissipated during their collision in the oblique impact mode. The value of the parameter k_E is calculated based on a hypothesis that accounts for the specific features of head-on and sliding collisions of spherical particles by combining the Newtonian and Routhian hypotheses [25, 26, 33]. To calculate the parameter k_E, the coefficients of restitution *k*, friction μ, and the reduction coefficient of the tangential velocity component λ during particle collisions are required in the following form:

$$k_E = (1-k^2) + \frac{1}{2}\lambda - \frac{1}{8}\mu^2(1+k)^2 - \\ -\frac{1}{8}\lambda^2 + \frac{2}{\pi}\mu(1+k) - \frac{2}{3\pi}\mu\lambda(1+k). \qquad (11)$$

The reduction coefficient of the tangential velocity component during particle collisions λ is determined using the method proposed in [33]. Thus, the difference $1-k_E$ determines the magnitude of the modified coefficient of restitution, which takes into account the effects of elasticity and roughness, during the collision of non-smooth inelastic balls under conditions unregulated by the collision angle.

Since the change in momentum is equal to the momentum of the force causing this change, the average value of the pressure of the granular medium on the vibrating surface can be expressed as follows:

$$p_y = \Delta m(0)V_r\left(1+(1-k_E)\right)^{0.5}\omega. \qquad (12)$$

Thus, using expression (7) in combination with the last relation, it is possible to calculate the intensity of the quasi-thermal flux $Q(0)$ generated by a vibrating surface in the boundary bed of a rarefied granular medium. The main problem in implementing this approach is determining the average value of the particle fluctuation velocity in the boundary bed of a granular medium $\langle V'(0)\rangle$. In general, the fluctuation velocity should be determined [25, 34] based on the dissipative component of the energy balance for an element of the granular medium as a function of its structural characteristics, the parameters of the medium filling the space between the particles, and the properties of the particles. In this paper, the fluctuation velocity is determined by the temperature of the granular medium (3) as a function of the intensity of the quasi-thermal vibration flux [25, 26].

To determine the magnitude of the quasi-thermal flux of vibrational oscillations in the volume of a granular medium, the postulate [25, 26] was used, according to which the magnitude of the flux is calculated in direct dependence on the local values of the temperature of the granular medium $\theta(y)$ and the concentration of particles per unit surface area located in a plane perpendicular to the quasi-thermal flux $(b^{-2}(y)d^{-2}(y))$, and the frequency ω of the vibrational oscillations:

$$Q(y) = b^{-2}(y)d^{-2}(y)\theta(y)\omega. \qquad (13)$$

Due to the dissipation of energy during collisions, the magnitude of the quasi-thermal flux decreases during its penetration into the volume of the granular medium. As a result, the dynamics of the quasi-thermal flux of vibrational oscillations in a particle bed can be expressed as follows:

$$Q(y) = Q(0) - \int_0^y \Delta Q(t)\,dt, \qquad (14)$$

where $\Delta Q(y)$ is a parameter that determines the amount of energy dissipated per unit volume of the medium.

With insignificant resistance of the medium in the space between particles, the calculation of $\Delta Q(y)$ can only be performed taking into account the energy dissipated during elastic deformation and friction of the particles (11). In this case, based on postulate (13) and taking into account the energy dissipation flux, which is determined proportionally to the local value of the volume concentration of particles $(b(y)d(y))^{-3}$, a relationship has been formulated in [25, 26] that allows one to determine the intensity of the quasi-thermal flux of vibrations depending on the depth of its penetration into the volume of the medium

$$Q(y) = Q(0)\mathrm{e}^{-\int_0^y k_E (b(t)d(t))^{-1} dt}. \qquad (15)$$

Dependence (15) reflects the influence of the structural heterogeneity of a granular medium on the attenuation intensity of the quasi-thermal flux of vibrations and, according to Expression (11) of the physical and mechanical properties of the particles.

Given the known intensity of the local values of the quasi-thermal flux $Q(y)$, taking into account its relationship with the granular temperature in accordance with postulate (13), the temperature can be expressed as a function of the coordinate in the direction of the flux:

$$\theta(y) = Q(y)(b(y)d(y))^2 / \omega. \qquad (16)$$

Thus, to predict the local values of the quasi-thermal flux (15) and the granular temperature (16), it is necessary to have local values of the parameter $b(y) = [\pi/(6(1-\varepsilon(y)))]^{0.33}$, i.e. the geometric characteristic of the structure, and the average particle diameter

$$d(y) = (c(y)/\rho_1 d_1 + \\ + (1-c(y))/\rho_2 d_2)(c(y)/\rho_1 + (1-c(y))/\rho_2)^{-1}.$$

Determining these parameters requires knowledge of the local values of the void fraction $\varepsilon(y)$ and the concentration of nonuniform particles $c(y)$ in the volume of the granular medium.

In turn, determining the distribution of the volume fraction of voids $\varepsilon(y)$ using the equation of state (1) presupposes the presence of a temperature distribution profile of the granular medium $\theta(y)$. The distribution profiles of the physical parameters of the granular medium ($\varepsilon(y)$, $\theta(y)$) are formed during the evolution of the initial homogeneous distributions during successive periods of oscillation. To determine the profiles, their evolution is modeled during a successive transition from one profile to another and from period to period until the medium parameters in the subsequent period differ negligibly from the parameters in the previous period. To implement the algorithm in the first period of vibration oscillations, the quasi-heat flux $Q_1(y)$ and temperature profile $\theta_1(y)$ are determined for an initial homogeneous distribution of particles in the medium in the absence of chaotic movements $(V'(y) = 0)$ as follows. Using equation (7), with an initial homogeneous distribution of motionless particles in the medium, the intensity of the quasi-thermal flux in the boundary volume of the bed $Q_1(0)$ is determined, as well as the flux dynamics in the bed using (15) and the granular temperature distribution in the medium (16). The dispersion pressure is determined based on the fact that the mass of particles that will contact the vibrating surface in the first period of oscillation is calculated as

$$\Delta m_1(0) = \overline{m}(0)(b(0)d(0))^{-3} A, \qquad (17)$$

and the average velocity of particle impact with the vibrating surface for the first period of oscillation can be calculated as

$$\Delta V = \frac{1}{t_0}\int_0^{t_0} 2\pi A\omega\cos(2\pi\omega t)dt, \qquad (18)$$

where $t_0 = 0.25/\omega$ is the temperature distribution and dispersion pressure $p_1(y) = \mathrm{const}$ obtained for the first period of oscillation are used to determine the dilatancy $\overline{\varepsilon}_1(y)$ and void fraction distributions $\varepsilon_1(y)$ based on equation of state (1).

In all subsequent periods of vibration oscillation, the quasi-thermal flux $Q_i(y)$ and he granular temperature profile $\theta_i(y)$ are determined using a similar scheme, but taking into account the inhomogeneous distribution of the void fraction and, accordingly, the particle concentration obtained during the previous period using the previously presented expressions (15) and (16). When calculating the quasi-thermal flux generated by a vibrating surface $Q_i(0)$, information on the average particle fluctuation velocity $\langle V_i'(0)\rangle$ in the volume of the medium adjacent to the surface is required for each subsequent period. This velocity is calculated using the local temperature of the granular medium $\theta_{i-1}(0)$ obtained in the previous period, i.e., it is assumed that, according to (3)

$$\langle V_i'(0)\rangle = (2\theta_{i-1}(0)/\rho_{i-1}(0))^{0.5}. \quad (19)$$

The simulation is carried out until certain minimum permissible changes in the temperature profile are reached. Implementation of the described algorithm determines the distribution of the solid phase fraction and the kinetic energy of fluctuations of uniform particles of the granular medium under the influence of vibrational oscillations in microgravity conditions.

2.4. Modeling the effects of quasi-diffusion separation and clustering of particles of a granular medium under the influence of vibrational oscillations in microgravity conditions

Under the heterogeneity of the solid phase distribution in the gaseous state of solid particles, mass transfer fluxes are formed, leading to the redistribution of the nonuniform components of the mixture [25, 26]. Separation fluxes are formed due to differences in the velocities of quasi-diffusion movements of nonuniform particles. During impact interactions of such particles under conditions of a solid phase concentration gradient, particles with a high fluctuation velocity (less dense, smaller, more elastic and smooth) experience an excess momentum directed along the void fraction gradient [25, 26]. As a result, in a granular medium that is inhomogeneous in composition and structure and in a gaseous state of solid particles, the effect of quasi-diffusion separation occurs. Quasi-diffusion separation occurs under the action of a driving force defined as the relative magnitude of the gradient of the average distance s between particles $\partial \ln s(y)/\partial y$. As a result, the intensity of the quasi-diffusion separation flux of particles with a high fluctuation velocity is determined by the following expression [25, 26]

$$j_s = c(y)\rho_b(y)D_{\text{ds}}\frac{\partial \ln s(y)}{\partial y}, \quad (20)$$

where $c(y)$ is the concentration of the control component; ρ_b is the local value of the bulk density of the medium; D_{ds} is the quasi-diffusion separation coefficient; $s = (b/b_0 - 1)d(y)$ is the average distance between particles; b_0 is the geometric parameter b calculated (13) for the case $\varepsilon = 0.2595$ (dense hexagonal packing of particles).

The intensity of quasi-diffusion transport of particles is determined by the velocity of their fluctuations and the mean free path [35]. As established in [36], the mean free path of particles in a granular medium, in general, depends not only on the properties of the particles and their volume fraction, but also on the hydrodynamic conditions in the volume of the medium. In a one-dimensional problem, it is possible to exclude the influence of boundary conditions on the dynamics of particle displacements and, as a consequence, to neglect the influence of shear effects on the mechanism of their collisions. Under this condition, the coefficient of quasi-diffusion separation of particles by size and density is expressed as follows [36]

$$D_{\text{ds}} = \frac{(\overline{m}(c)\langle V'(y)\rangle)^2}{2\overline{F}}\left(\left(\frac{\overline{d}}{m_1 d_1}\right)^2 - \left(\frac{\overline{d}}{m_2 d_2}\right)^2\right), \quad (21)$$

where $\overline{m}(c)$ is the average value of the particle mass; m_i, d_i is the mass and diameter of the particles of the i-th component; $\overline{d}$ is the average local value of the particle diameter; $\overline{F} = \langle V'(y)\rangle / s(y)$ is the average value of the particle collision frequency.

To model the distribution dynamics of nonuniform particles $c(y, t)$ within a granular medium bed subjected to vibrational oscillations under microgravity conditions, a general equation for separation dynamics [25, 26] was used. In the absence of convection and gravitational segregation fluxes, this equation is written as follows:

$$\frac{\partial(c\rho_b)}{\partial t} = \frac{\partial}{\partial y}\left[\rho_b\left(D_{\text{dif}}\frac{\partial c}{\partial y} - cD_{\text{ds}}\frac{\partial \ln s}{\partial y}\right)\right]. \quad (22)$$

In the presented form, the dynamics of the distribution of particles of the control component of the mixture $c(y,\tau)$ is described as the result of the conjugation of quasi-diffusion flows of mixing and separation of nonuniform particles. The mixing flow intensity is defined [25, 26] as the product of the quasi-diffusion mixing coefficient and the concentration gradient of the control component. The quasi-diffusion mixing coefficient is calculated based on the local dilatancy $\overline{\varepsilon}(y)$ and temperature $\theta(y)$ of the vibro-fluidized granular medium, which are mutually correlated, as determined by the equation of state of the granular medium (1). Dilatancy and temperature of a granular medium are used, in accordance with their definitions (2) and (3), to express local values of the average distance between particles $s(y)$ and the average velocity of their fluctuations $\langle V'(y)\rangle$, followed by the calculation of the quasi-diffusive mixing coefficient

$$D_{\text{dif}} = 1/3\langle V'(y)\rangle s(y). \quad (23)$$

The distribution dynamics of nonuniform particles in a bed of a binary particle mixture subjected to vibrational oscillations under microgravity conditions was modeled by numerically integrating equation (22) using the Crank-Nicolson difference scheme [37]. The solution was obtained under the boundary condition

$$D_{\text{dif}} \frac{\partial c}{\partial y} = cD_{\text{ds}} \frac{\partial \ln s}{\partial y}\bigg|_{y=0,\delta/2} = 0 \qquad (24)$$

and an initial condition corresponding to a uniform distribution of control particles within the bed volume

$$c(y,0) = \bar{c}, \qquad (25)$$

where $\bar{c}$ is the average concentration of control particles in the mixture. A uniform initial distribution of cohesionless particles is assumed due to the assumption of an entropic process of equalization of the parameters of a rarefied granular medium under zero-gravity conditions.

3. Results and Discussion

The study was carried out using mathematical modeling of the structural and kinematic parameters and distribution of bronze balls with diameters of 1 and 2 mm in an unbounded (one-dimensional) flat bed 45 mm thick under the influence of vibration in the absence of gravity. The bed characteristics and the vibration parameters of the surfaces bounding it were assumed to be equal to the corresponding characteristics of the measuring cell in the second experiment [2] (see the "Materials and Methods" section). The modeling was performed under the assumption that the vibrating surfaces were made of bronze and their physical and mechanical properties corresponded to those of the particles (restitution coefficient $k = 0.9$, friction coefficient $\mu = 0.4$ [2]). The concentration of control large particles in the mixture ($c = 0.561$ kg·kg^{-1}) and the average value of the solid phase fraction in the bed volume (0.089) were determined based on the quantitative ratio of large (80 pieces) and small (500 pieces) particles and their total volume in the volume of the measuring cell under the conditions of Experiment 2 [2].

The mathematical modeling of the effects of clustering and particle separation by size was carried out using a method for determining structural and kinematic characteristics based on the equation of state of a granular medium (1) and a mathematical model of the dynamics of mass transfer processes for nonuniform particles (22). Equation (1) is used in combination with the models of generation (7) and dissipation (15) of quasi-thermal flux.

The coefficient χ of the equation of state of a granular medium (1) was determined by modeling the distribution of 80 uniform large ($d = 2$ mm) bronze particles in a measuring cell in suborbital experiment No. 1 [2]. It was found that the distribution of the solid phase and the corresponding dilatancy values $\bar{\varepsilon}(y)$ in the measuring cell is modeled with a coefficient χ in equation (1), which is close to 1. The resulting value $\chi = 1$ was used to model the dynamics of the solid phase distribution and the granular temperature under the influence of vibrational oscillations in a mixture of nonuniform particles.

Figure 2 shows the distributions of $\varepsilon(y)$ and $\theta(y)$ in the particle mixture bed. Particle vibrations are generated by harmonic surface oscillations with a coordinate of $y = 0$. The presented results were used to determine the vibration parameters that facilitate particle cluster formation in the absence of gravity (Fig. 3). Furthermore, the results were used to model the concentration distribution of large particles along the bed thickness (Fig. 4).

In order to identify the conditions facilitating the formation of a particle cluster, Figure 3 shows the dependences of the gradient of the solid phase fraction and the granular temperature of the medium on the penetration depth of vibration oscillations into the particle bed. A comprehensive analysis of these dependences, combined with visual experimental information (the Parabolic Flight Campaign (PFC64) study) [2], which clearly demonstrates the cluster boundaries, suggests that the formation of a particle cluster is evidenced by a sharp increase in the gradient of the solid phase fraction at a bed depth of 14 to 18 mm, followed by a sharp decrease in its values.

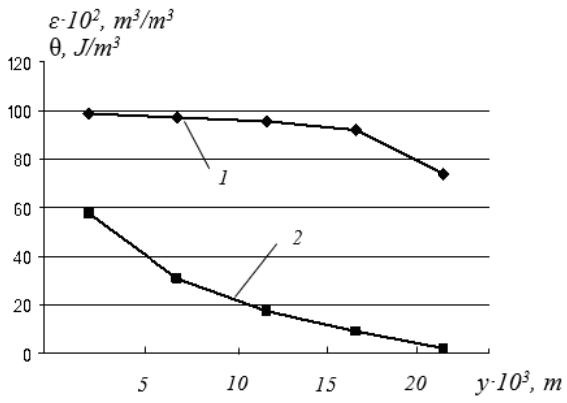

Fig. 2. Distribution of the volume fraction of voids *1* and the temperature of the granular temperature *2* in a bed of vibro-fluidized binary mixture of spherical bronze particles with diameters of 1 and $2 \cdot 10^{-3}$ m in the absence of gravity

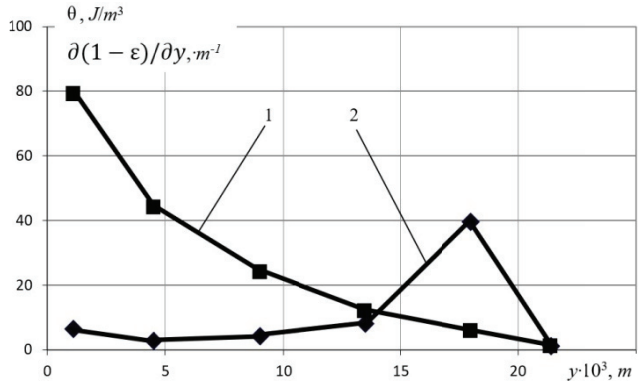

Fig. 3. Illustration of the physical conditions for particle cluster formation under vibrational action on a bed of a binary mixture of spherical bronze particles with a diameter of 1 and $2 \cdot 10^{-3}$ m in the absence of gravity: the temperature of the granular medium *1* and the gradient of the solid phase fraction *2* as functions of the coordinate in the direction of vibrational oscillations

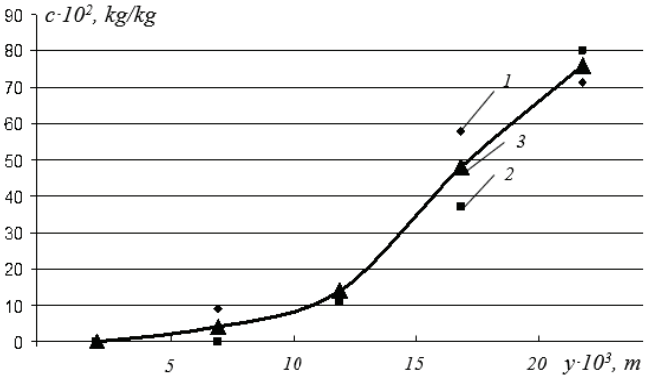

Fig. 4. Concentration distribution of large particles ($2 \cdot 10^{-3}$ m) mixed with small particles ($1 \cdot 10^{-3}$ m) in a vibro-fluidized bed of a binary mixture of spherical bronze particles under microgravity conditions: *1* – modeling results; *2* – experimental visual information [2]; *3* – trend line

Moreover, it is quite logical that the formation of a particle cluster occurs as the granular temperature approaches zero. As a result, the formation of a particle cluster is confirmed by a sharp increase in the gradient of the solid phase fraction at its boundary and low, close to zero, values of the gradient and granular temperature in the cluster volume. In this regard, it can be concluded that the main conditions for cluster formation during vibration exposure to a particle bed in a state of weightlessness are sufficiently high values of solid phase concentration and bed thickness, at which the quasi-thermal vibration flux has a limited penetration area. Consequently, a region forms within the particle bed in which the quasi-thermal vibration flux is close to zero.

The result of modeling the particle separation process by size during vibration exposure to a bed of their binary mixture under microgravity conditions is shown in Figure 4 in comparison with the experimental data obtained in [2]. The experimental data represent the result of averaging visual information regarding the distribution of large and small particles in the volume of the measuring cell presented in [2]. The averaging of visual information was carried out using a counting statistical method from fragments of the image of the measuring cell in Experiment 2, located to the left and right of its symmetry axis. Despite the noticeable discrepancy between some local calculated and experimental values, the concentration fields obtained by the modeling method based on equation (22) and experimentally [2] correspond to the trend line 3 common to them. One explanation for the presence of areas with a noticeable discrepancy between the calculated and experimental results in the concentration distributions may be the influence of the edge effect of the side walls of the measuring cell on the particle distribution under the experimental conditions. If the particle separation modeling was carried out under conditions of an unbounded bed (one-dimensional problem), then the relatively small distance between the side walls of the measuring cell compared to the particle size in the experiment [2] indicates the presence of features of a three-dimensional object.

A comprehensive analysis of the calculated and experimental concentration distributions shown in Figure 4 demonstrates that a phenomenological description of the vibroseparation process under microgravity conditions can be achieved using the quasi-diffusion separation effect [25, 26, 36]. Furthermore, based on the findings, it is possible to predict the high potential for technological application of the quasi-diffusion separation effect under microgravity conditions. This primarily applies to technologies for separating materials based on a range of particle physical and mechanical properties (size, density, roughness, and elasticity). The prospects for the technological use of the effect of quasi-diffusion separation under microgravity conditions are determined, on the one hand, by the wide possibilities of organizing intensive and stable quasi-diffusion interaction of nonuniform particles in a rarefied state (low proportion of solid phase) and, on the other hand, by the significant dependence of the rate of quasi-diffusion of particles on their properties.

4. Conclusion

Based on a phenomenological analysis of the state of a granular medium subjected to vibration in microgravity, an explanation for the physical nature of the phenomena and a method for predicting the effects of cluster formation and distribution of nonuniform particles have been proposed. The equation of state for a granular medium has been adapted to describe the structural and kinematic characteristics of a granular medium consisting of cohesionless spherical particles subjected to vibration in the absence of gravity. The conditions for cluster formation in a rarefied particle bed under the influence of vibrations of the surfaces bounding the bed have been determined. It has been established that cluster formation is due to a limited region of active penetration of the quasi-thermal vibration flux into the bed and the presence of a region with a quasi-thermal flux close to zero. A phenomenological description of the vibroseparation process in microgravity conditions is provided by analyzing the interaction of particles in a vibrofluidized bed based on the fundamental principles of diffusion kinetics. It has been established that the dynamics of the concentration distribution of nonuniform particles can be described analytically as the conjugation of fluxes initiated by quasi-diffusion effects of separation and mixing. A comparison of the modeling results with experimental data obtained during a suborbital flight (Parabolic Flight Campaign (PFC64)) using the VIP-Gran instrument [2] indicates good qualitative agreement.

5. Conflict of interest

The authors declare no conflict of interest.

References

1. Hestroffer D, Sánchez P, Staron L, Bagatin AC, et al. Small solar system bodies as granular media. *The Astronomy and Astrophysics Review*. 2019;27(1):6. DOI:10.1007/s00159-019-0117-5
2. Opsomer E, Noirhomme M, Vandewalle N, Falcon E, et al. Segregation and pattern formation in dilute granular media under microgravity conditions. *npj Microgravity*. 2017;3(1):1. DOI:10.1038/s41526-016-0009-1
3. Wurm G, Teiser J. Understanding planet formation using microgravity experiments. *Nature Reviews Physics*. 2021;3(6):405-421. DOI:10.1038/s42254-021-00312-7
4. Schneider N, Musiolik G, Kollmer JE, Steinpilz T, et al. *Experimental study of clusters in dense granular gas and implications for the particle stopping time in protoplanetary disks*. 2021. Available from: https://arxiv.org/abs/2103.03609 [Accessed 3 September 2025]
5. Führer F, Schwaak J, Brendel L, Wurm G, et al. Hybrid simulation method for agglomerate evolution in driven granular gases. *Astronomy & Astrophysics*. 2025;694:A191. DOI:10.1051/0004-6361/202451459
6. Hirabayashi M, Scheeres DJ. Analysis of asteroid (216) Kleopatra using dynamical and structural constraints. *The Astrophysical Journal*. 2013;780(2):160. DOI:10.1088/0004-637X/780/2/160
7. Brisset J, Colwell J, Dove A, Abukhalil S, et al. Regolith behavior under asteroid-level gravity conditions: low-velocity impact experiments. *Progress in Earth and Planetary Science*. 2018;5(1):73. DOI:10.1186/s40645-018-0222-5
8. Born P, Schmitz J, Sperl M. Dense fluidized granular media in microgravity. *npj Microgravity*. 2017;3(1):27. DOI:10.1038/s41526-017-0030-z
9. Opsomer E, Vandewalle N, Noirhomme M, Ludewig F. Clustering and segregation in driven granular fluids. *The European Physical Journal E*. 2014;37(11):115. DOI:10.1140/epje/i2014-14115-1
10. Opsomer E, Ludewig F, Vandewalle N. Phase transitions in vibrated granular systems in microgravity. *Physical Review E*. 2011;84(5):051306. DOI:10.1103/PhysRevE.84.051306
11. Sack A, Windows-Yule K, Heckel M, Werner D, et al. Granular dampers in microgravity: sharp transition between modes of operation. *Granular Matter*. 2020;22(2):54. DOI:10.1007/s10035-020-01017-x
12. Harth K, Kornek U, Trittel T, Strachauer U, et al. Granular gases of rod-shaped grains in microgravity. *Physical Review Letters*. 2013;110(14):144102. DOI:10.1103/PhysRevLett.110.144102
13. Noirhomme M, Cazaubiel A, Falcon E, Fischer D, et al. Particle dynamics at the onset of the granular gas-liquid transition. *Physical Review Letters*. 2021; 126(12):128002. DOI:10.1103/PhysRevLett.126.128002
14. Grasselli Y, Bossis G, Morini R. Translational and rotational temperatures of a 2D vibrated granular gas in microgravity. *The European Physical Journal E*. 2015;38(2):8. DOI:10.1140/epje/i2015-15008-5
15. Harth K, Kornek U, Trittel T, Strachauer U, et al. Granular gases of rod-shaped grains in microgravity. *Physical Review Letters*. 2013;110(14):144102. DOI:10.1103/PhysRevLett.110.144102
16. Huang Y, Zhu C, Xiang X, Mao W. Liquid-gas-like phase transition in sand flow under microgravity. *Microgravity Science and Technology*. 2015;27(3):155-170. DOI:10.1007/s12217-015-9424-2
17. Chen YP, Evesque P, Hou MY. Breakdown of energy equipartition in vibro-fluidized granular media in micro-gravity. *Chinese Physics Letters*. 2012;29(7):074501. DOI:10.1088/0256-307X/29/7/074501
18. Windows-Yule CRK, Parker DJ. Boltzmann statistics in a three-dimensional vibrofluidized granular bed: idealizing the experimental system. *Physical Review E*. 2013;87(2):022211. DOI:10.1103/PhysRevE.87.022211
19. Windows-Yule CRK, Tunuguntla DR, Parker DJ. Numerical modelling of granular flows: a reality check. *Computational Particle Mechanics*. 2016;3(3):311-332. DOI:10.1007/s40571-015-0083-2
20. Hill KM, Fan Y. Granular temperature and segregation in dense sheared particulate mixtures. *KONA*

Powder and Particle Journal. 2016;33:150-168. DOI:10.14356/kona.2016022

21. Duan Y, Jing L, Umbanhowar PB, Ottino JM, et al. General model for segregation forces in flowing granular mixtures. *Journal of Fluid Mechanics*. 2024;989:A17. DOI:10.1017/jfm.2024.483

22. Duan Y, Jing L, Umbanhowar PB, Ottino JM, et al. *Granular segregation across flow geometries: a closure model for the particle segregation velocity*. 2025. Available from: https://arxiv.org/pdf/2410.08350 [Accessed 3 September 2025]

23. Domnik B, Pudasaini SP, Katzenbach R, Miller SA. Coupling of full two-dimensional and depth-averaged models for granular flows. *Journal of Non-Newtonian Fluid Mechanics*. 2013;201:56-68. DOI:10.1016/j.jnnfm.2013.07.005

24. Forterre Y, Pouliquen O. Flows of dense granular media. *Annual Review of Fluid Mechanics*. 2008;40(1):1-24. DOI:10.1146/annurev.fluid.40.111406.102142

25. Dolgunin VN, Kudi AN, Ukolov AA, Tuev MA. Rapid granular flows on a vibrated rough chute: behaviour patterns and interaction effects of particles. *Chemical Engineering Research and Design*. 2017;122:22-32. DOI:10.1016/j.cherd.2017.03.038

26. Dolgunin VN, Kudi AN, Tuev MA. Mechanisms and kinetics of gravity separation of granular materials. *Physics-Uspekhi*. 2020;63(6):545-561. DOI:10.3367/UFNe.2020.01.038729

27. Bagnold RA. Experiments on a gravity-free dispersion of large solid spheres in a newtonian fluid under shear. *Proceedings of the Royal Society of London. Series A. Mathematical and Physical Sciences*. 1954;225(1160):49-63. DOI:10.1098/rspa.1954.0186

28. Brennen CE. *Fundamentals of multiphase flow*. Cambridge University Press; 2005. Vol. 9780521848046, p. 1-345. DOI:10.1017/CBO9780511807169

29. Baxter GW, Olafsen JS. The temperature of a vibrated granular gas. *Granular Matter*. 2006;9(1-2):135-139. DOI:10.1007/s10035-006-0019-x

30. Asmar BN, Langston PA, Walters JK, Matchett AJ, et al. Distinct element model of energy dissipation in vibrated binary particulate mixtures. *Particulate Science and Technology*. 2006;24(4):395-409. DOI:10.1080/02726350600934648

31. Gidaspow D. *Multiphase flow and fluidization: Continuum and kinetic theory description*. San Diego: Academic press; 1994. 467 p.

32. Nagel SR. Experimental soft-matter science. *Reviews of Modern Physics*. 2017;89(2):025002. DOI:10.1103/RevModPhys.89.025002

33. Dolgunin VN, Ivanov OO, Ukolov AA. Segregation kinetics of particles with different roughneses and elasticities under a rapid gravity flow of a granular medium. *Theoretical Foundations of Chemical Engineering*. 2009;43(2):187-195. DOI:10.1134/S0040579509020092

34. Shen H, Ackermann NL. Constitutive relationships for fluid-solid mixtures. *Journal of the Engineering Mechanics Division*. 1982;108(5):748-763. DOI:10.1061/JMCEA3.0002868

35. Ferziger JH, Kaper HG. *Mathematical theory of transport processes in gases*. Amsterdam: North-Holland Publ. House; 1972. 606 p.

36. Dolgunin V, Kudi A, Zhilo A, Kudi K, et al. Quasidiffusion effects in fast gravitational flows of cohesionless particles of granular matter. *Journal of Advanced Materials and Technologies*. 2024;9(4):296-311. DOI:10.17277/jamt.2024.04.pp.296-311

37. Marchuk GI. *Methods of numerical mathematics*. New York: Springer; 1975. 510 p.

38. Dolgunin VN, Kudi AN, Tarakanov AG. Structural inhomogeneity and effects of separation by size and density in gravity flow of granular materials. *Journal of Engineering Physics and Thermophysics*. 2022;95(2):484-494. DOI:10.1007/s10891-022-02505-y

Information about the authors / Информация об авторах

Viktor N. Dolgunin, D. Sc. (Eng.), Professor, Tambov State Technical University (TSTU), Tambov, Russian Federation; ORCID 0000-0002-6227-5224; e-mail: dolgunin-vn@yandex.ru

Konstantin A. Kudi, chief financial analyst, JSC "BCS Bank", Moscow, Russian Federation; ORCID 0009-0009-5068-2234; e-mail: kostya.kudi@mail.com

Andrey A. Zhilo, PhD Student, TSTU, Tambov, Russian Federation; ORCID 0000-0001-5033-8315; e-mail: zhilo97@mail.ru

Долгунин Виктор Николаевич, доктор технических наук, профессор, Тамбовский государственный технический университет (ТГТУ), Тамбов, Российская Федерация; ORCID 0000-0002-6227-5224; e-mail: dolgunin-vn@yandex.ru

Куди Константин Андреевич, главный финансовый аналитик, АО «БКС Банк», Москва, Российская Федерация; ORCID 0009-0009-5068-2234; e-mail: kostya.kudi@mail.com

Жило Андрей Андреевич, аспирант, ТГТУ, Тамбов, Российская Федерация; ORCID 0000-0001-5033-8315; e-mail: zhilo97@mail.ru

Received 10 September 2025; Revised 17 October 2025; Accepted 27 October 2025

Original papers
Nanostructured, nanoscale materials and nanodevices

УДК 543.424 DOI: 10.17277/jamt-2025-10-04-313-320

A study of the structure of carbon nanomaterials by Raman spectroscopy: analysis of spectra of commercial samples of graphite, nanotubes and carbon blacks

© Elena V. Kuzmina[a]✉, Elvina R. Gaifullina [a,b], Alena M. Ionina[a], Elena V. Karaseva[a], Vladimir S. Kolosnitsyn[a]

[a] *Ufa Institute of Chemistry of Ufa Federal Research Centre of the Russian Academy of Sciences, 69, Oktyabrya Av., Ufa, 450054, Russian Federation,*
[b] *Akmulla Bashkir State Pedagogical University, 3a, Oktyabrskoy Revolyutsii St., Ufa, 450077, Russian Federation*

✉ kuzmina@anrb.ru

Abstract: This paper summarizes the results of structural investigations of carbon nanomaterials using Raman spectroscopy. The conducted research revealed that the distances between defects are 26–43 nm in graphites, 12–16 nm in multi-walled carbon nanotubes (MWCNTs) and 11–15 nm in carbon black. It is shown that the Raman spectra of high-quality graphites and graphenes are characterized by a narrow G band (width less than 35 cm^{-1}), intensity ratio $I_{(D)}/I_{(G)} < 0.3$. The Raman spectra of carbon nanotubes are characterized by wide G bands (width > 50 cm^{-1}), high $I_{(D)}/I_{(G)}$ ratio (> 0.5) and the presence of 2D bands with a maximum position of about 2670 cm^{-1}. The Raman spectra of carbon blacks are characterized by a strongly broadened G band (width > 70 cm^{-1}), the $I_{(D)}/I_{(G)}$ ratio is close to 1 and more. The presence, position and width of 2D bands are sensitive to the structures of carbon materials. For ordered graphites, the position of the 2D band maximum is about 2680 cm^{-1}, and their width is < 85 cm^{-1}. For MWCNTs, the 2D band maximum is in the range of 2670–2690 cm^{-1}, and the band width is about 90–100 cm^{-1}. In the Raman spectra of carbon blacks, the 2D band may be absent; the position of the maximum may be shifted to the long-wave or short-wave regions, the 2D band is strongly broadened (width > 150 cm^{-1}).

Keywords: Raman spectroscopy; graphite; carbon nanotubes; carbon black.

For citation: Kuzmina EV, Gaifullina ER, Ionina AM, Karaseva EV, Kolosnitsyn VS. A study of the structure of carbon nanomaterials by Raman spectroscopy: analysis of spectra of commercial samples of graphite, nanotubes and carbon blacks. *Journal of Advanced Materials and Technologies*. 2025;10(4):313-320. DOI: 10.17277/jamt-2025-10-04-313-320

Исследование структуры углеродных наноматериалов методом спектроскопии комбинационного рассеяния: анализ спектров коммерческих образцов графитов, нанотрубок и саж

© Е. В. Кузьмина[a]✉, Э. Р. Гайфуллина [a,b], А. М. Ионина [a], Е. В. Карасева [a], В. С. Колосницын [a]

[a] *Уфимский Институт химии Уфимского федерального исследовательского центра Российской академии наук, пр. Октября, 69, Уфа, 450054, Российская Федерация,*
[b] *Башкирский государственный педагогический университет им. М. Акмуллы, ул. Октябрьской революции, 3а, Уфа, 450077, Российская Федерация*

✉ kuzmina@anrb.ru

Аннотация: В статье суммированы результаты исследований структуры углеродных наноматериалов методом спектроскопии комбинационного рассеяния (КР). В результате проведенных исследований установлено, что расстояния между дефектами в графитах находятся в диапазоне 26…43 нм, углеродных многостенных углеродных

нанотрубок (МУНТ) – 12…16 нм и саж 11…15 нм. Показано, что для КР-спектров высококачественных графитов и графенов характерны узкая G-полоса (ширина менее < 35 см$^{-1}$), соотношение интенсивностей $I_{(D)}/I_{(G)}$) < 0,3. Для КР-спектров углеродных нанотрубок характерны широкие G-полосы (ширина > 50 см$^{-1}$), высокое соотношение $I_{(D)}/I_{(G)}$ (> 0,5) и наличие 2D-полос с положением максимума около 2670 см$^{-1}$. Для КР-спектров саж характерно сильно уширенная G-полоса (ширина > 70 см$^{-1}$), соотношение $I_{(D)}/I_{(G)}$ близко к 1 и более. Наличие, положение и ширина 2D-полос чувствительны к структурам углеродных материалов. Для упорядоченных графитов положение максимума 2D-полос составляет порядка 2680 см$^{-1}$, а их ширина менее < 85 см$^{-1}$. Для МУНТ максимум 2D-полосы находится в диапазоне 2670…2690 см$^{-1}$, а ширина полосы порядка 90…100 см$^{-1}$. На КР-спектрах саж 2D-полоса может отсутствовать; положение максимума может быть смещено в длинноволновую или коротковолновую области, 2D-полоса сильно уширена (ширина > 150 см$^{-1}$).

Ключевые слова: спектроскопия комбинационного рассеяния; графит; углеродные нанотрубки; сажи.

Для цитирования: Kuzmina EV, Gaifullina ER, Ionina AM, Karaseva EV, Kolosnitsyn VS. A study of the structure of carbon nanomaterials by Raman spectroscopy: analysis of spectra of commercial samples of graphite, nanotubes and carbon blacks. *Journal of Advanced Materials and Technologies*. 2025;10(4):313-320. DOI: 10.17277/jamt-2025-10-04-313-320

1. Introduction

Carbon materials are widely used as components of electrodes in electrochemical energy storage devices such as supercapacitors, lithium-ion, and post-lithium-ion batteries. The properties of carbon materials strongly depend on their atomic structure, degree of ordering, type and concentration of defects, as well as the dimensional characteristics of their constituent elements [1–4].

Studying the structure of carbon nanomaterials is important for understanding their properties. Traditional analytical methods, such as electron microscopy and X-ray diffraction, provide valuable information about macrostructure and crystalline order [5–9]. However, these techniques do not fully describe the structure, degree of ordering, and defects of carbon materials. A comprehensive structural description of carbons requires the use of multiple complementary methods.

It is well known that Raman spectra (RS) of carbon materials are sensitive to the structure and allotropic form of carbon [9–11]. For this reason, Raman spectroscopy is widely applied to study the structural organization of carbons [12–20]. Raman spectra can provide information about the size of atomically ordered domains in carbon materials, their structure, type of mutual ordering, atomic geometry of boundaries, and many other important characteristics [9, 10, 21–28].

The shape of Raman spectra of carbons depends on several factors, including the presence of clusters of sp^2-hybridized carbon atoms, the degree of disorder, the presence of rings and chains composed of sp^2-hybridized carbon atoms, and the ratio of sp^2 to sp^3 hybridized carbon atoms [12, 29]. If the carbon material contains sp^2 carbon networks, the G band (~1580 cm^{-1}) appears in the Raman spectrum. In the presence of sp^3 and sp carbon networks, characteristic D (~1330 cm^{-1}, diamond) and D′ (1850–2100 cm^{-1}, linear chains of sp^2 carbon atoms) bands are observed [30]. Structurally ordered 3D graphites also exhibit a 2D (or G′) band in the 2500–2800 cm^{-1} region [30]. The 2D band corresponds to the second overtone of the D band [30].

The D band may show dispersion depending on the excitation energy [20]. However, the higher the degree of disorder, the smaller the D band dispersion – which is opposite to the behavior of the G band [29]. The full width at half maximum (hereafter referred to as the width) of the G band always increases with increasing disorder [31], while the position of the G band maximum shifts toward shorter wavelengths [19].

Broadening of the D band may indicate changes in the size of rings within graphene layers (with 5- and 7-membered rings appearing instead of 6-membered ones) [17].

In structurally disordered carbons, the maximum of the G band shifts toward the long-wavelength region as the excitation wavelength decreases (from the infrared to the ultraviolet range) [29]. The shift of the G band maximum position with changing laser wavelength depends on the degree of disorder in the carbon structure and on the configuration of the sp^2-hybridized carbon atoms.

Based on the shift of the G band maximum position with decreasing laser wavelength, carbons can be classified into two types:

Type 1. In materials containing only sp^2-hybridized rings, the G band shift does not exceed approximately 1600 cm^{-1}.

Type 2. In materials containing sp^2-hybridized chains (such as amorphous carbon and diamond-like carbon), the G band maximum shifts to the long-

wavelength region beyond 1600 cm^{-1} and may reach up to 1690 cm^{-1} when excited with radiation at a wavelength of 229 nm [29, 32, 33].

Thus, the position and shape of the bands in the Raman spectra of carbon materials can provide information about their structure. The G band characterizes the degree of disorder in the carbon material, and the relative intensity of the G peak increases with the number of graphene layers. The D band reflects the degree of structural disorder near the boundaries of microcrystalline regions, which reduces their symmetry.

The aim of this work was to study the microstructure of various commercial nanostructured allotropic forms of carbon materials using Raman spectroscopy.

2. Materials and Methods

2.1. Materials under study

The following carbon materials were used in this study:

(a) Graphites and graphene: Timrex® SLP50 (TIMCAL Graphite & Carbon); synthetic graphite (Dianshi); natural Korean graphite (NG-10); graphite (Alpha); multilayer graphene GLNP-0350 (GraphenLab).

(b) Carbon fibers and nanotubes: Nano fiber ENF 100AA-GFE (carbon nanofibers, Electrovac AG); Pyrograf II™ (carbon fiber HT grade, highly graphitic carbon nanofiber, Pyrograf Products, Inc.); MWCNT Graphistrength® U100 (Arkema); MWCNT Graphistrength® C100 (Arkema); MWCNT BAYTUBES® C70P (Bayer AG); MWCNT LUCANTM CP1001M (LG Chem); Taunit–MD (NanoTechCenter LLC).

(c) Carbon blacks: Ketjenblack® EC-600JD (Akzo Nobel Polymer Chemicals LLC); PRINTEX® XE2 (Degussa AG); Monarch® 1300 (Cabot Corp.); Monarch® 1400 (Cabot Corp.); Super P™ Li (TIMCAL Graphite & Carbon); activated carbon black Bau-MF.

2.2. Characterization methods

Raman spectra of the samples were obtained using an EnSpectr R532 Raman spectrometer equipped with a 532 nm laser operating at an optical power of 30 mW. The laser spot diameter was 0.6 μm. Spectra were recorded in the 150–6000 cm^{-1} range with a spectral resolution of 5–8 cm^{-1}.

The carbon materials were used without any preliminary treatment. Samples for Raman measurements were in powder form.

When processing the Raman spectra of the carbon materials, it was assumed that they belong to Stage 1 according to the classification proposed by Ferrari and Robertson**,** with an average interdefect distance L_D greater than 10 nm, which can be calculated using Equation (1) [9, 29, 32, 33]:

$$L_D^2 = \frac{4.3 \cdot 10^3}{E_L^4} \left[\frac{I_{(D)}}{I_{(G)}} \right]^{-1}, \quad (1)$$

where L_D is the average distance between defects (nm); E_L is the laser energy eV; $I_{(D)}$ and $I_{(G)}$ are the intensities of the D and G bands, respectively.

3. Results and Discussion

3.1. Raman spectra of graphites

In the Raman spectra of graphite samples (Fig. 1), three characteristic bands are observed: D, G, and 2D. The position of the G band maximum varies within the frequency range of 1563–1576 cm^{-1}, the D band within 1340–1342 cm^{-1}, and the 2D band within 2674–2690 cm^{-1}. All bands are relatively narrow and well defined. A weakly resolved D′ band can also be observed as a shoulder on the G band at 1620–1650 cm^{-1}. The intensity ratio $I_{(D)}/I_{(G)}$ does not exceed 0.2 (Table 1).

The relatively narrow width and position of the 2D band correspond to the structure of multilayer graphene or highly ordered graphite. The shape and position of the 2D band maximum confirm the predominance of sp^2 structures.

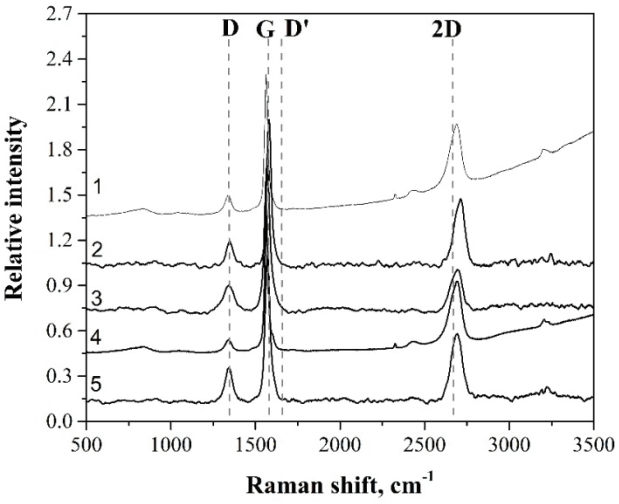

Fig. 1. Raman spectra of graphites and graphenes. Designations of carbon materials on the graph: *1* – Timrex SLP50; *2* – Alpha; *3* – NG-10; *4* – Graphene CLNP_0350; *5* – Dianshi

Table 1. Parameters of the microstructure of carbon materials calculated from Raman spectra

Samples	D band		G band		2D band		$\frac{I_{(D)}}{I_{(G)}}$	L_D, nm
	λ, cm^{-1}	FWHM, cm^{-1}	λ, cm^{-1}	FWHM, cm^{-1}	λ, cm^{-1}	FWHM, cm^{-1}		
Graphite and graphene								
Timrex SLP50	1339	45	1563	26	2683	77	0.13	34
Graphene GLNP-0350	1340	45	1564	26	2684	80	0.08	43
Dianshi	1342	50	1571	29	2690	78	0.22	26
Alpha	1341	89	1576	69	2674	83	0.14	32
NG-10	1342	75	1569	33	2687	81	0.16	30
Carbon nanotubes								
Taunit-MDTM	1341	68	1580	59	2693	89	0.56	16
Baytubes® C70P	1337	59	1573	69	2674	87	1.06	12
Graphistrength® U100	1335	71	1572	62	2670	94	1.03	12
Graphistrength® C100	1333	64	1569	70	2666	95	1.02	12
LUCAN TM CP1001M	1332	70	1569	77	2670	99	1.05	12
Carbon black								
PrintexXE2	1341	64	1576	73	2717	292	1.08	12
Super® Li	1338	81	1561	130	2541	356	0.69	15
Ketjenblack® EC-600JD	1329	85	1576	93	2655	174	1.11	11
Monarch 1300	1347	111	1572	149	n/a	n/a	0.77	14
Monarch 1400	1347	112	1575	133	n/a	n/a	0.69	15
BAU MF	1341	212	1562	147	n/a	n/a	1.03	12

The D band width is about 45 cm^{-1}, except for the NG-10 and Alpha samples, for which FWHM(D) values are 75 and 89 cm^{-1}, respectively. The G band width ranges from 26 to 30 cm^{-1}, except for the Alpha sample, which exhibits a width of 69 cm^{-1} (Table 1). The 2D band width for all graphite samples lies within 77–83 cm^{-1}.

It is worth noting that the Raman spectrum of the commercial graphene sample Graphene CLNP_0350 corresponds to that of well-ordered graphite.

3.2. Raman spectra of carbon nanotubes

The Raman spectra of MWCNTs exhibit D, D′, G, and 2D bands (Fig. 2). In addition to the main bands, broadened asymmetric bands are observed at approximately 850 and 1050 cm^{-1}, which are associated with defects, and a band at ~2950 cm^{-1} corresponding to a combination mode (D + G) induced by the presence of defects [30, 34].

The D band maxima of the carbon nanotubes are in the range 1332–1343 cm^{-1}, while the 2D band maxima are in the range 2666–2693 cm^{-1}. The G band maximum in the MWCNT spectra occurs within 1569–1586 cm^{-1}, which is characteristic for carbon nanotubes. The G band maximum of Taunit-MD™ (1580 cm^{-1}) is slightly shifted toward the long-wavelength region, likely due to the presence of amorphous carbon and/or the nanotube diameter. The positions of the G, D, and 2D bands are consistent with those expected for multi-walled carbon nanotubes.

The G bands are significantly broader than those of high-quality graphite or graphene (by a factor of 2–3). This is a typical feature of MWCNTs, attributed to their cylindrical geometry and the possible presence of defects or amorphous phases.

The intensity ratio $I_{(D)}/I_{(G)}$ is substantially higher than that of graphite or graphene (see Table 1). This is a distinguishing characteristic of MWCNTs

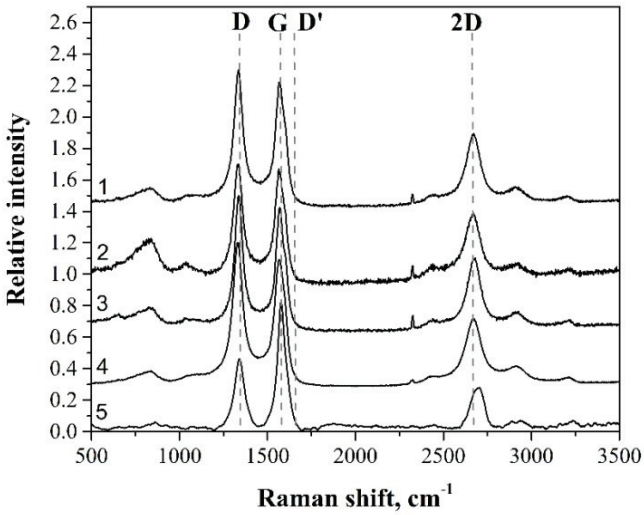

Fig. 2. Raman spectra of carbon nanotubes.
Designations of carbon materials on the graph:
1 – Graphistrength® U100; *2* – Graphistrength® C100;
3 – Baytubes® C70P; *4* – LUCAN TM CP1001M;
5 – TAUNIT-MD TM

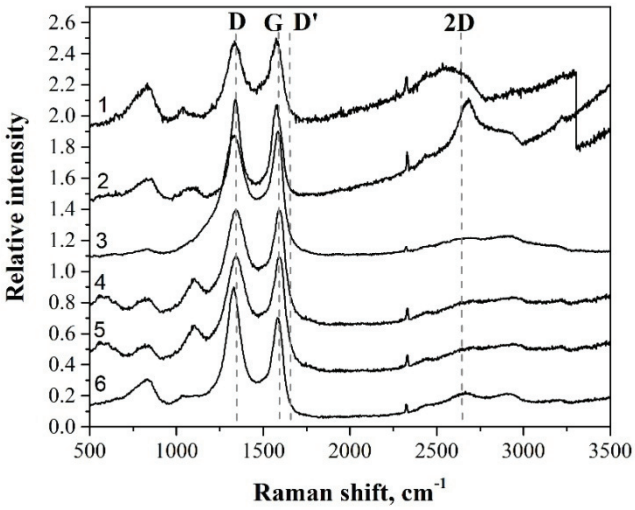

Fig. 3. Raman spectra of carbon blacks.
Designations of carbon materials on the chart:
1 – Super Li carbon black; *2* – PrintexXE2; *3* – Bau-MF;
4 – Monarch 1300; *5* – Monarch 1400;
6 – Ketjenblack® EC-600JD

and is related both to edge effects of the tubes and to the possible presence of defects or amorphous carbon. High values (1.02–1.06) for Graphistrength® and LUCAN™ CP1001M indicate either small nanotube diameters or a relatively high level of defects/impurities.

The calculated average interdefect distances L_D are significantly smaller than those of graphite (see Table 1), which is consistent with the nanoscale nature of MWCNTs and their characteristically high $I_{(D)}/I_{(G)}$ ratio.

3.3. Raman spectra of carbon blacks

The Raman spectra of carbon blacks are characterized by intense D and G bands, as well as a low-intensity, broad 2D band (Fig. 3). The D band maximum is located in the range of 1330–1347 cm^{-1}, while the G band maximum falls within 1560–1576 cm^{-1}. The 2D band is absent in the spectra of Monarch 1300, Monarch 1400, and Bau-MF carbon blacks.

Broadened asymmetric bands are also observed at approximately 850 and 1050 cm^{-1}, which are associated with defects. Notably, the relative intensity of these bands is higher than in carbon nanotubes, indicating a higher defect density in carbon blacks compared to nanotubes.

The G bands are significantly broadened, with widths ranging from 70 to 150 cm^{-1}. The intensity ratio $I_{(D)}/I_{(G)}$ is close to or exceeds 1, except for Super® Li and Monarch 1400. The 2D bands are also substantially broadened, with widths in the range of 170–360 cm^{-1}.

The calculated interdefect distances L_D are comparable to the crystallite sizes of MWCNTs and are significantly smaller than those of graphite (see Table 1).

The pronounced broadening of the G and 2D bands, the $I_{(D)}/I_{(G)}$ ratio close to unity, and the presence of bands at ~850 and 1050 cm^{-1} indicate high defect density and small crystallite size in these carbon blacks.

Thus, based on the analysis of the recorded Raman spectra of commercial carbon material samples, the following conclusions can be drawn:

– The Raman spectra of high-quality graphite and graphene are characterized by a narrow G band (width < 35 cm^{-1}) and an intensity ratio $I_{(D)}/I_{(G)} < 0.3$;

– The Raman spectra of carbon nanotubes are characterized by broad G bands (width > 50 cm^{-1}), a high $I_{(D)}/I_{(G)}$ ratio (> 0.5), and the presence of 2D bands with maxima around 2670 cm^{-1};

– The Raman spectra of carbon blacks exhibit a significantly broadened G band (width > 70 cm^{-1}), $I_{(D)}/I_{(G)}$ ratio close to or exceeding 1, and a 2D band that is either absent or strongly broadened (width > 150 cm^{-1}).

The presence, position, and width of the 2D bands are sensitive to the structure of the carbon materials.

In ordered graphites, the 2D band maximum is around 2680 cm^{-1}, and the width is less than 85 cm^{-1}.

In MWCNTs, the 2D band maximum lines in the range 2670–2690 cm^{-1}, with a width of approximately 90–100 cm^{-1}. In carbon blacks, the 2D band may be absent; its maximum can be shifted toward either the long- or short-wavelength region, and the band is strongly broadened (width > 150 cm^{-1}).

The $I_{(D)}/I_{(G)}$ ratio should only be compared for carbon materials of the same type. High values in graphite/graphene ($I_{(D)}/I_{(G)} > 0.2$) indicate the presence of defects, whereas for carbon nanotubes and carbon blacks, $I_{(D)}/I_{(G)}$ values of 0.5–1.0 are typical.

4. Conclusion

The Raman spectra of various carbon forms – graphite, nanotubes, and carbon blacks – were analyzed.

It was found that the average interdefect distances are:

– 26–43 nm for graphite;

– 12–16 nm for multi-walled carbon nanotubes;

– 11–15 nm for carbon blacks.

Carbon nanofibers and nanotubes occupy an intermediate position in terms of grain size and interdefect distance, having a less ordered structure compared to graphite but more ordered than carbon blacks.

Thus, analysis of the D, G, and 2D band parameters (position, width, intensity ratio) allows reliable classification of materials, assessment of structural perfection, crystallinity, and defect density, and comparative evaluation of commercial products. The G band width and 2D band characteristics are particularly informative.

5. Funding

The work was carried out as part of the State Assignment on the topic of Research Work at the Ufa Institute of Chemistry, Ufa Scientific Center, Russian Academy of Sciences, No. 124032600061-3.

6. Conflict of interest

The authors declare no conflict of interest.

References

1. Geim AK, Novoselov KS. The rise of graphene. *Nature Materials*. 2007;6(3):183-191. DOI:10.1038/nmat1849

2. Islam MH, Afroj S, Uddin MA, Andreeva DV, et al. Graphene and CNT-based smart fiber-reinforced composites: a review. *Advanced Functional Materials*. 2022;32(40):2205723. DOI:10.1002/adfm.202205723

3. Wu X, Mu F, Zhao H. Recent progress in the synthesis of graphene/CNT composites and the energy-related applications. *Journal of Materials Science & Technology*. 2020;55:16-34. DOI:10.1016/j.jmst.2019.05.063

4. Labunov VA, Tabulina LV, Komissarov IV, Trapov DV, et al. Features of graphene reduction from graphene oxide. *Zhurnal Fizicheskoy Khimii = Russian Journal of Physical Chemistry A*. 2017;(6):1018-1023. DOI:10.7868/S0044453717060176 (In Russ.)

5. Kang DS, Lee SM, Lee SH, Roh JS. X-ray diffraction analysis of the crystallinity of phenolic resin-derived carbon as a function of the heating rate during the carbonization process. *Carbon Letters*. 2018;27:108-111. DOI:10.5714/CL.2018.27.108

6. Lee SM, Lee SH, Roh JS. Analysis of activation process of carbon black based on structural parameters obtained by XRD analysis. *Crystals*. 2021;11(2):153. DOI:10.3390/cryst11020153

7. Bessonov VB. Microfocus X-ray tubes. *Journal of the Russian Universities*. *Radioelectronics*. 2021;24(5):6-21. DOI:10.32603/1993-8985-2021-24-5-6-21

8. Tan WH, Lee SL, Chong CT. TEM and XRD analysis of carbon nanotubes synthesised from flame. *Key Engineering Materials*. 2016;723:470-475. DOI:10.4028/www.scientific.net/KEM.723.470

9. Ferrari AC, Basko DM. Raman spectroscopy as a versatile tool for studying the properties of graphene. *Nature Nanotechnology*. 2013;8(4):235-246. DOI:10.1038/nnano.2013.46

10. Li Z, Deng L, Kinloch IA, Young RJ. Raman spectroscopy of carbon materials and their composites: graphene, nanotubes and fibres. *Progress in Materials Science*. 2023;135:101089. DOI:10.1016/j.pmatsci.2023.101089

11. Ziatdinov AM. Raman spectroscopy of nanoscale honeycomb carbon structures. *Vestnik Dal'nevostochnogo Otdeleniya Rossiyskoy Akademii Nauk*. 2020;(6(214)):27-40. DOI:10.37102/08697698.2020.214.6.003 (In Russ.)

12. Verzhbitskiy IA, Corato MD, Ruini A, Molinari E, et al. Raman fingerprints of atomically precise graphene nanoribbons. *Nano Letters*. 2016;16(6):3442-3447. DOI:10.1021/acs.nanolett.5b04183

13. Zhang J, Perrin ML, Barba L, Overbeck J, et al. High-speed identification of suspended carbon nanotubes using Raman spectroscopy and deep learning. *Microsystems & Nanoengineering*. 2022;8(1):19. DOI:10.1038/s41378-022-00350-w

14. Finnie P, Ouyang J, Fagan JA. Static and dynamic Raman excitation mapping of chirality-pure carbon nanotube films. *Communications Materials*. 2025;6(1):10. DOI:10.1038/s43246-024-00727-6

15. Lucchese MM, Stavale F, Ferreira EHM, Vilani C, et al. Quantifying ion-induced defects and Raman relaxation length in graphene. *Carbon*. 2010;48(5):1592-1597. DOI:10.1016/j.carbon.2009.12.057

16. Cançado LG, Monken VP, Campos JLE, Santos JCC, et al. Science and metrology of defects in graphene using Raman spectroscopy. *Carbon*. 2024;220:118801. DOI:10.1016/j.carbon.2024.118801

17. Liu X, Choi J, Xu Z, Grey CP, et al. Raman spectroscopy measurements support disorder-driven capacitance in nanoporous carbons. *Journal of the American Chemical Society*. 2024;146(45):30748-30752. DOI:10.1021/jacs.4c10214

18. Senda T, Tanaka F, Ishikawa T, Okino S, et al. Developing a novel evaluation technique of Raman spectra for pan-based carbon fibers using dependence of excitation wavelength and differential spectra. *Carbon*. 2025;234:119970. DOI:10.1016/j.carbon.2024.119970

19. Yuan R, Guo Y, Gurgan I, Siddique N, et al. Raman spectroscopy analysis of disordered and amorphous carbon materials: a review of empirical correlations. *Carbon*. 2025;238:120214. DOI:10.1016/j.carbon.2025.120214

20. Madito MJ. Revisiting the Raman disorder band in graphene-based materials: a critical review. *Vibrational Spectroscopy*. 2025;139:103814. DOI:10.1016/j.vibspec.2025.103814

21. Ribeiro-Soares J, Oliveros ME, Garin C, David MV, et al. Structural analysis of polycrystalline graphene systems by Raman spectroscopy. *Carbon*. 2015;95:646-652. DOI:10.1016/j.carbon.2015.08.020

22. Jorio A, Souza Filho AG. Raman studies of carbon nanostructures. *Annual Review of Materials Research*. 2016;46(1):357-382. DOI:10.1146/annurev-matsci-070115-032140

23. Eckmann A, Felten A, Mishchenko A, Britnell L, et al. Probing the nature of defects in graphene by Raman spectroscopy. *Nano Letters*. 2012;12(8):3925-3930. DOI:10.1021/nl300901a

24. Mohan AN, Manoj B, Ramya AV. Probing the nature of defects of graphene like nano-carbon from amorphous materials by Raman spectroscopy. *Asian Journal of Chemistry*. 2016;28(7):1501-1504. DOI:10.14233/ajchem.2016.19739

25. Cançado LG, Takai K, Enoki T, Endo M, et al. Measuring the degree of stacking order in graphite by Raman spectroscopy. *Carbon*. 2008;46(2):272-275. DOI:10.1016/j.carbon.2007.11.015

26. Cançado LG, Pimenta MA, Neves BRA, Dantas MSS, et al. Influence of the atomic structure on the Raman spectra of graphite edges. *Physical Review Letters*. 2004;93(24):247401. DOI: 10.1103/PhysRevLett.93.247401

27. Cançado LG, Takai K, Enoki T, Endo M, et al. General equation for the determination of the crystallite size la of nanographite by Raman spectroscopy. *Applied Physics Letters*. 2006;88(16):163106. DOI:10.1063/1.2196057

28. Bokobza L, Bruneel JL, Couzi M. Raman spectroscopy as a tool for the analysis of carbon-based materials (highly oriented pyrolitic graphite, multilayer graphene and multiwall carbon nanotubes) and of some of their elastomeric composites. *Vibrational Spectroscopy*. 2014;74:57-63. DOI:10.1016/j.vibspec.2014.07.009

29. Ferrari AC, Robertson J. Interpretation of Raman spectra of disordered and amorphous carbon. *Physical Review B*. 2000;61(20):14095-14107. DOI:10.1103/PhysRevB.61.14095

30. Pimenta MA, Dresselhaus G, Dresselhaus MS, Cançado LG, et al. Studying disorder in graphite-based systems by Raman spectroscopy. *Physical Chemistry Chemical Physics*. 2007;9(11):1276-1290. DOI:10.1039/B613962K

31. Ferrari AC, Rodil SE, Robertson J. Interpretation of infrared and Raman spectra of amorphous carbon nitrides. *Physical Review B*. 2003;67(15):155306. DOI:10.1103/PhysRevB.67.155306

32. Ferrari AC, Robertson J. Resonant Raman spectroscopy of disordered, amorphous, and diamondlike carbon. *Physical Review B*. 2001;64(7):075414. DOI:10.1103/PhysRevB.64.075414

33. Cançado LG, Jorio A, Ferreira EHM, Stavale F, et al. Quantifying defects in graphene via Raman spectroscopy at different excitation energies. *Nano Letters*. 2011;11(8):3190-3196. DOI:10.1021/nl201432g

34. Maslova OA, Ammar MR, Guimbretière G, Rouzaud JN, et al. Determination of crystallite size in polished graphitized carbon by Raman spectroscopy. *Physical Review B*. 2012;86(13):134205. DOI:10.1103/PhysRevB.86.134205

Information about the authors / Информация об авторах

Elena V. Kuzmina, Cand. Sc. (Chem.), Senior Scientist, Head of the Laboratory, Ufa Institute of Chemistry of Ufa Federal Research Centre of the Russian Academy of Sciences (UIC UFRS RAS), Ufa, Russian Federation, ORCID 0000-0002-3758-4762; e-mail: kuzmina@anrb.ru

Кузьмина Елена Владимировна, кандидат химических наук, старший научный сотрудник, заведующий лабораторией, Уфимский Институт химии Уфимского федерального исследовательского центра Российской академии наук (УФИХ УФИЦ РАН), Уфа, Российская Федерация; ORCID 0000-0002-3758-4762; e-mail: kuzmina@anrb.ru

Elvina R. Gaifullina, Laboratory Research Assistant, UIC UFRS RAS; Master's degree, Akmulla Bashkir State Pedagogical University, Ufa, Russian Federation; ORCID 0009-0005-3452-072X; e-mail: e.gaifullina02@mail.ru

Alena M. Ionina, Junior Scientist, PhD Student, UIC UFRS RAS, Ufa, Russian Federation; ORCID 0009-0005-4842-7294; e-mail: aionina27@xmail.ru

Elena V. Karaseva, Cand. Sc. (Chem.), Associate Professor, Leading Researcher, Head of Laboratory, UIC UFRS RAS, Ufa, Russian Federation; ORCID 0000-0002-8447-7230; e-mail: karaseva@anrb.ru

Vladimir S. Kolosnitsyn, D. Sc. (Chem.), Professor, Chief Scientist, Head of Department, UIC UFRS RAS, Ufa, Russian Federation; ORCID 0000-0003-1318-6943; e-mail: kolos@anrb.ru

Гайфуллина Эльвина Равилевна, лаборант-исследователь, УФИХ УФИЦ РАН; магистр, Башкирский государственный педагогический университет им. М. Акмуллы, Уфа, Российская Федерация; ORCID 0009-0005-3452-072X; e-mail: e.gaifullina02@mail.ru

Ионина Алена Михайловна, младший научный сотрудник, аспирант, УФИХ УФИЦ РАН, Уфа, Российская Федерация; ORCID 0009-0005-4842-7294; e-mail: aionina27@xmail.ru

Карасева Елена Владимировна, кандидат химических наук, доцент, ведущий научный сотрудник, заведующий лабораторией, УФИХ УФИЦ РАН, Уфа, Российская Федерация; ORCID 0000-0002-8447-7230; e-mail: karaseva@anrb.ru

Колосницын Владимир Сергеевич, доктор химических наук, профессор, главный научный сотрудник, заведующий отделом, УФИХ УФИЦ РАН, Уфа, Российская Федерация; ORCID 0000-0003-1318-6943; e-mail: kolos@anrb.ru

Received 12 August 2025; Revised 18 September 2025; Accepted 23 September 2025

Original papers
Nanostructured, nanoscale materials and nanodevices

УДК 53.087.4537.533.2 DOI: 10.17277/jamt-2025-10-04-321-328

A method for eliminating capacitive and noise components from a recorded signal in a field emission experiment

© Sergei A. Sokov[a]✉, Mikhail S. Nechaev[a], Boris E. Mutygullin[a], Anatoly G. Kolosko[a], Sergei V. Filippov[a], Eugeni O. Popov[a]

[a] *Ioffe Institute, 26, Politekhnicheskaya St., Saint Petersburg, 194021, Russian Federation*

✉ sokovclan@gmail.com

Abstract: The paper presents new methods for eliminating random and systematic errors that occur when registering the current-voltage characteristics of field cathodes in the high-voltage fast scanning mode. The methods are implemented in the LabVIEW graphical programming environment and integrated into the experimental installation software, which registers and processes field emission data in real time. The developed program consists of three modules. The first one eliminates the effect of constant interference on current and voltage signals. The second module eliminates the systematic sinusoidal error associated with the presence of capacitance in the measuring circuit. The third module reduces the effect on the signal of noise associated with measuring equipment, as well as fluctuations in the emission activity of the cathode. The resulting current-voltage characteristic is processed in semi-logarithmic coordinates using the Murphy-Good equation. As a result of the processing, the values of the effective parameters are obtained. A test experiment was conducted with a field cathode based on multi-walled carbon nanotubes grown by the plasma-assisted chemical vapor deposition (PECVD-method). The technique was also used to accurately evaluate the emission properties of various types of cathodes: those based on carbon nanoparticles, regular matrix tips, and single-pointed cathodes.

Keywords: field emission; carbon nanotubes; current-voltage characteristic; real-time data processing.

For citation: Sokov SA, Nechaev MS, Mutygullin BE, Kolosko AG, Filippov SV, Popov EO. A method for eliminating capacitive and noise components from a recorded signal in a field emission experiment. *Journal of Advanced Materials and Technologies*. 2025;10(4):321-328. DOI: 10.17277/jamt-2025-10-04-321-328

Метод устранения емкостной и шумовой составляющих из регистрируемого сигнала в полевом эмиссионном эксперименте

© С. А. Соков[a]✉, М. С. Нечаев[a], Б. Э. Мутыгуллин[a], А. Г. Колосько[a], С. В. Филиппов[a], Е. О. Попов[a]

[a] *Физико-технический институт им. А. Ф. Иоффе РАН, ул. Политехническая, 26, Санкт-Петербург, 194021, Российская Федерация*

✉ sokovclan@gmail.com

Аннотация: Представлены новые способы устранения случайных и систематических ошибок, возникающих при регистрации вольтамперных характеристик полевых катодов в режиме быстрого сканирования высоким напряжением. Методы реализованы в среде графического программирования LabVIEW и интегрированы в программное обеспечение экспериментальной установки, которая регистрирует и обрабатывает данные полевой эмиссии в режиме реального времени. Разработанная программа состоит из трех модулей. Первый устраняет влияние постоянной наводки на сигналы тока и напряжения. Второй модуль устраняет систематическую ошибку синусоидальной формы, связанную с наличием емкости в измерительной цепи. Третий модуль уменьшает влияние на сигнал шумов, связанных с измерительным оборудованием, а также флуктуациями эмиссионной активности катода. Результирующая вольтамперная характеристика подвергается обработке в полулогарифмических координатах с применением уравнения Мерфи–Гуда. В результате обработки получаются значения эффективных параметров. Тестовый эксперимент был проведен с полевым катодом на основе многостенных углеродных

нанотрубок, выращенных химическим осаждением из газовой фазы с использованием плазмы (метод PECVD). Методика также применялась для корректной оценки эмиссионных свойств катодов различного типа: на основе углеродных наночастиц, регулярных матриц острий и одноострийных катодов.

Ключевые слова: полевая эмиссия; углеродные нанотрубки; вольтамперная характеристика; обработка данных в режиме реального времени.

Для цитирования: Sokov SA, Nechaev MS, Mutygullin BE, Kolosko AG, Filippov SV, Popov EO. A method for eliminating capacitive and noise components from a recorded signal in a field emission experiment. *Journal of Advanced Materials and Technologies*. 2025;10(4):321-328. DOI: 10.17277/jamt-2025-10-04-321-328

1. Introduction

Conducting an experiment to study the properties of field cathodes is a complex process that requires careful attention to detail. This includes ensuring the necessary vacuum conditions, precisely setting the interelectrode distance, applying a high voltage to the sample in order to obtain field emission, and recording experimental data. The analysis of the collected information can be done both after the experiment has been completed [1–3] or in real-time [4]. The results of the experiment are typically the current-voltage characteristics (I-V characteristics), as well as estimates of the microscopic effective parameters of the emitter derived from these I-V characteristics, such as the emission area and field enhancement factor [5].

The main problem in measuring I-V characteristics is the impact of various factors that cause distortion of the collected data. Such distortions are usually caused by random or systematic errors [6]. Random errors usually have a normal distribution. An example would be noise in the measuring circuit caused by external electric fields [7], or noise caused by temperature fluctuations [8], or the spread of geometric parameters of the emitter [9].

Systematic errors are not random in nature and in some cases can be described by a mathematical function, such as a phase shift of the detected signal or leakage currents [10, 11] resulting from the presence of capacitive elements in the measuring circuit.

Various approaches are employed to minimize the impact of random and systematic errors. This includes improving the measurement system, such as reducing power source noise or shielding external leads. Another approach is to incorporate preliminary signal correction into the processing of experimental data. The correction can be achieved by identifying the sources of inaccuracy and finding the error profile that can then be subtracted from the signal. This approach is particularly useful when it is not possible to minimize the error by improving the experimental setup.

An example of mathematical correction of data was presented in [14]. The fluctuations in the values of the experimental I-V characteristics when calculating effective parameters led to a random error. It was possible to minimize the impact of this error by averaging the fluctuating values of the parameters.

This paper presents methods for correcting the I-V characteristics, which make it possible to eliminate parasitic components of the signal in real-time – the constant impact of the power supply and variable capacitive of the measuring circuit. Additionally, it averages the data obtained, eliminating noise contribution.

2. Materials and Methods

2.1. Model sample

The model sample (field emitter) was a multi-tip structure based on multiwalled carbon nanotubes (CNTs) formed by PECVD (plasma-enhanced chemical vapor deposition) at the National Research University of Electronic Technology (MIET) [15]. The substrate was a tungsten plate measuring 9×4 mm^2. The nanotube parameters were length $L \sim 3$ μm and diameter $D \sim 13$ nm. The emitting surface consisted of randomly arranged nanotubes protruding above the surface.

The experiment was conducted under high vacuum conditions with a pressure of $\sim10^{-7}$ Torr. The distance between the electrodes was $d_{sep} = 270$ μm. The experiment was conducted with voltage amplitude of up to 3 kV.

2.2. Experimental setup for multi-channel and high-speed data acquisition

Error correction methods were developed for an experimental setup that allows recording the characteristics of field emitters and calculating the values of effective parameters in real time [14]. Figure 1 shows its block diagram.

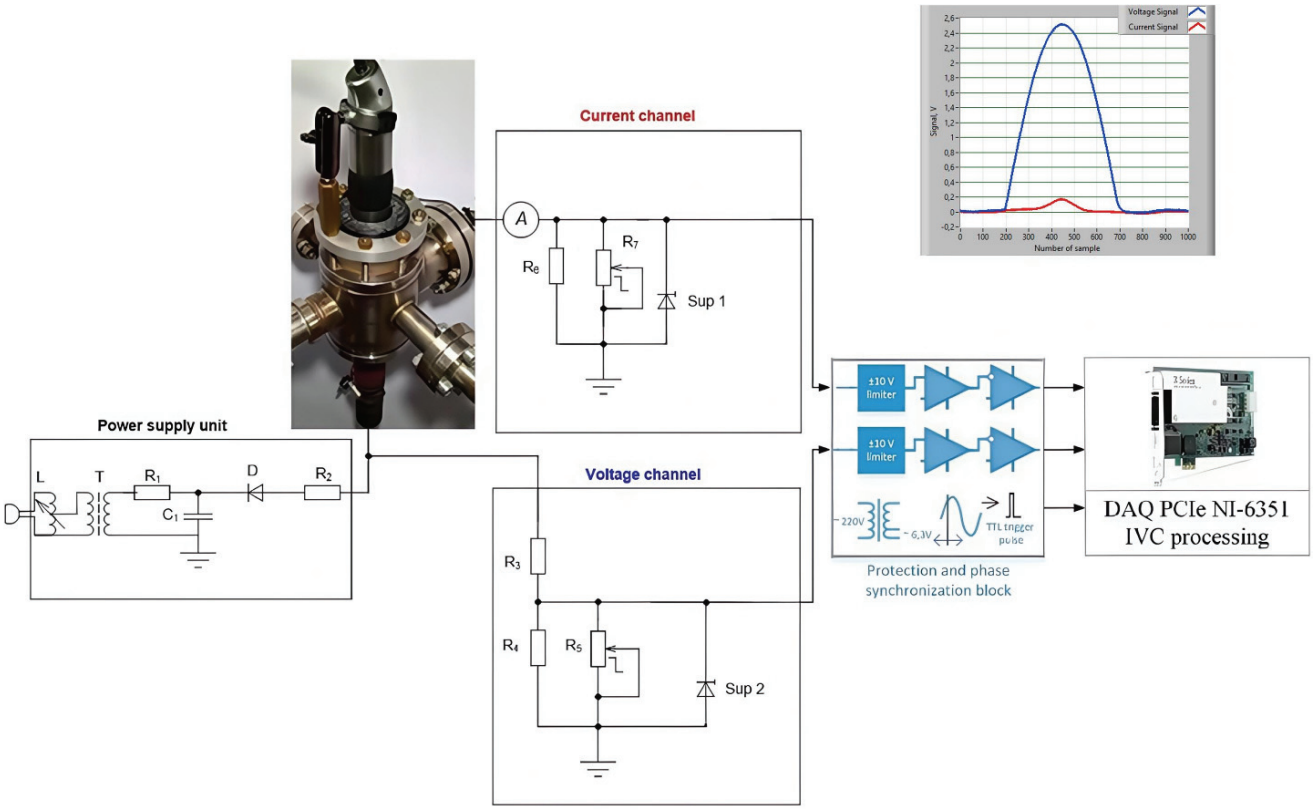

Fig. 1. A block diagram of multi-channel and high-speed data acquisition

A high-voltage power supply based on a Mosrentgen AII-70 X-ray transformer supplies half-sinusoidal voltage pulses to the cathode (fast scanning mode), so that one 10-ms pulse produces a single I-V characteristic.

The voltage and current on the sample are measured from the terminals of resistive dividers. The dividers include resistor boxes, allowing the division ratio to be adjusted and ensuring signal amplitude compatibility with the recording equipment.

To protect against voltage surges, which may occur, for example, as a result of vacuum breakdown in the measurement chamber, a cascade of operational amplifiers is installed between each divider and the data acquisition board.

The cascade's output voltage range is limited to ±10 V, which matches the input parameters of the NI DAQ 6351 data acquisition board.

The board is installed in a workstation to perform analog-to-digital conversion of half-sinusoidal voltage pulses and corresponding emission current pulses, and to read these digitized signals using multifunctional software implemented in the LabVIEW graphical programming environment.

A trailing-edge detector for half-sinusoidal voltage pulses is used to synchronize signal digitization with the power supply frequency. Synchronizing rectangular pulses are fed through a separate channel to the data acquisition board.

For each voltage and current pulse digitized by the board, graphs of their profiles, as well as the dependence of current on voltage, are displayed on the workstation screen. A fragment of the I-V characteristic is plotted on a separate graph in semilogarithmic coordinates. This fragment is processed in real time, obtaining linear regression coefficients and calculating effective parameters: the field enhancement factor (FEF) and the field emission area (FEA). The analysis is performed in Murphy-Good coordinates: $Y = \ln(I/U^{2-\eta/6})$, $X = 1/U$, which correspond to modern field emission theory [16]. Here $\eta(\varphi) = b_{\mathrm{FN}} c_S^2 \varphi^{-1/2}$, $b_{\mathrm{FN}} = 6.83 \cdot 10^9$ $\mathrm{eV}^{-3/2} \cdot \mathrm{V} \cdot \mathrm{m}^{-1}$ is the second Fowler–Nordheim constant, $c_S^2 = 1.44 \cdot 10^{-9}$ eV^2 $\mathrm{m} \cdot \mathrm{V}^{-1}$ is the Schottky constant, φ is the work function of the emitter surface, which is ~4.6 eV for CNTs. The effective parameters are collected in separate data arrays, which are displayed on the screen as two graphs: FEF(t) and FEA(t) as functions of time.

3. Results and Discussion

To solve the problem of eliminating random and systematic errors when recording voltage and current values, three software modules were developed and integrated into the general software for recording and analyzing I-V characteristics.

The first module is designed to subtract from the signal profile the constant systematic error caused by electromagnetic interference from the power supply. The second module is designed to eliminate the systematic error that varies with voltage level. The third module is required to reduce I-V characteristic noise at low voltages.

Figure 2*a* shows a graph of the time course of a voltage pulse generated by the recording system in the absence of voltage at the emitter. The first software module accumulates and averages the profiles of these signals, which yields the constant systematic error shape. The averaging time is specified by the user. For example, approximately 100 packets (arrays of pulse values) are recorded in 10 s. The resulting error profile is stored and subtracted in real time from each subsequent packet of values in the experiment.

This procedure is performed for both voltage and current pulses. Figure 2*b* shows the corrected signal, along with the resulting constant systematic error profile.

As a result, the current value spread is reduced from 10^{-5} to 10^{-7} A, leaving behind noise from the measuring equipment and power supply.

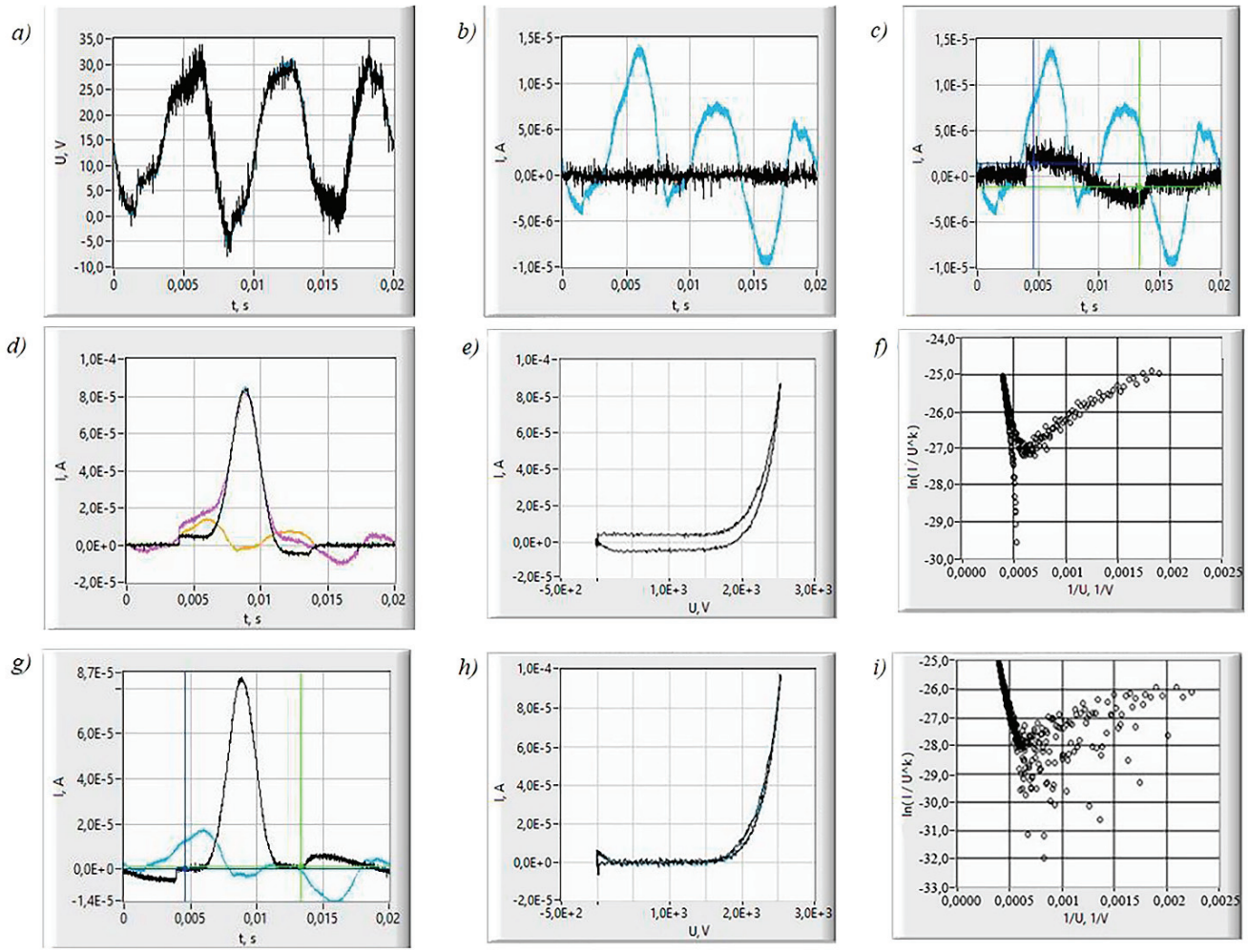

Fig. 2. Correction of the I-V characteristic by subtracting the capacitive and noise components: *a* is the voltage input signal before the scanning pulse is applied; *b* is the current input signal after subtracting the constant mains current (black) and before subtracting (blue); *c* is the current signal before a noticeable emission occurs, which shows a sinusoidal addition of a systematic error, the edges of which are highlighted the blue and green cursors; the remaining figures show the pulse of the emission current corresponding to the I-V characteristic and I-V characteristic-FN: *d*, *e*, *f* – before subtracting the sinusoidal component; *g*, *h*, *i* – after correction

After this initial correction, voltage is applied to the test sample. As the voltage level increases, the contribution of the changing systematic error becomes visible on the current pulse profile graph. This error has a sinusoidal shape and increases with the voltage amplitude. This error significantly affects the recorded values at low emission currents (~1 μA) and appears even before noticeable field emission occurs (see Fig. 2*c*).

The influence of the variable error on the recorded emission current signal is manifested in the form of a skew in the pulse profile (Fig. 2*d*), the hysteresis on the I-V characteristic (Fig. 2*e*), as well as the divergence of the falling and growing branches on the I-V characteristic-FN curve (Fig. 2*f*).

By varying the elements of the measuring circuit, it was found that this variable contribution is due to the fact that there is a capacitive element in the data acquisition board. The second software module allows the experimenter to calculate and eliminate the contribution of this error. By manually controlling the cursors, two points are selected on the graph of the current pulse profile at which the applied voltage is so low that the emission current is significantly absent or does not exceed the noise level (Fig. 2*c*). Based on the current values at these points, the correction parameters are calculated, which has a sinusoidal shape:

$$y = A\sin(\omega t - \varphi), \tag{1}$$

where A is amplitude, φ is the phase shift.

The parameters are calculated as follows:

$$\varphi = 2\pi f t_{\max}, \tag{2}$$

where $f = 50$ Hz is the frequency of scanning pulses; $t_{\max}$ is the time point corresponding to the maximum pulse amplitude (located automatically);

$$A = \frac{(y_1 - y_2)}{\sin(\omega x_1 - \phi) - \sin(\omega x_2 - \phi)}, \tag{3}$$

where (x_1, y_1), (x_2, y_2) are coordinates of the points set by the cursors, $\omega = 2\pi f$.

After subtracting the sinusoidal correction, the dependencies take on a more accurate form: the current pulse becomes more symmetrical (Fig. 2*g*), the hysteresis in the I-V characteristic curve practically disappears (Fig. 2*h*), and the convergence of the I-V characteristic and FN branches increases at low voltages (Fig. 2*i*).

After subtracting the constant and variable systematic errors, noise remains in the recorded signal, which also has a significant impact on the evaluation of the effective parameters [17]. This noise is associated both with the measuring system and with the influence of random processes on the cathode emission activity, such as the deposition of residual atmospheric particles on the emitter surface [18]. In the low-current range, noise causes the corrected current signal to be negative in some places, which complicates the construction of a trend line in semilogarithmic coordinates and requires the removal of this section of the I-V characteristic from the analysis. A special function in the signal recording and analysis software allows automatic selection of the I-V characteristic section for analysis corresponding to the linearity specified by the experimenter (maximum average deviation from the Residue trend line).

Reducing the impact of noise (random error) is the task of the third module. This module sums and averages the values of current and voltage pulse packets, displaying the average I-V characteristic and the number of averaged signals in real time. This makes it possible to select a longer section for regression analysis (see Fig. 3*ab*) and obtain effective parameter values with greater accuracy.

The effective parameters obtained in real time as a result of I-V characteristic averaging cease to fluctuate (see Fig. 3*cd*).

Processing the I-V characteristic of the carbon nanotube cathode using the modules described above resulted in an adjustment of the field enhancement factor from FEF = 937 ± 28 to FEF = 889 ± 3 (a 5 % decrease), and the emission area values from FEA = 52 ± 37 nm^2 to FEA = 80 ± 3 nm^2 (an increase of 54 %). The range of the I-V characteristics selected for the analysis was limited to a maximum Residue = 0.01. The obtained FEF value corresponds to theoretical concepts of emission from carbon nanotubes [19].

It should be noted that the presented method of I-V characteristic correction leads to similar improvements in the shape of the I-V characteristic not only in the case of the considered cathode made of multi-walled CNTs, but also for other samples investigated on the same experimental setup. We applied the method to study the following types of samples: nanocomposites of carbon particles in a polymer matrix (single-walled CNTs and graphene [14], $FEF_{SWCNT} = 1700$, $FEF_G = 450$); arrays of tips created by lithography (silicon [20], $FEF_{Si} = 250$); macroscopic blade cathodes (silicon [21], $FEF_{blade} = 190$). CNTs demonstrate consistently high FEF values of the order of 1000.

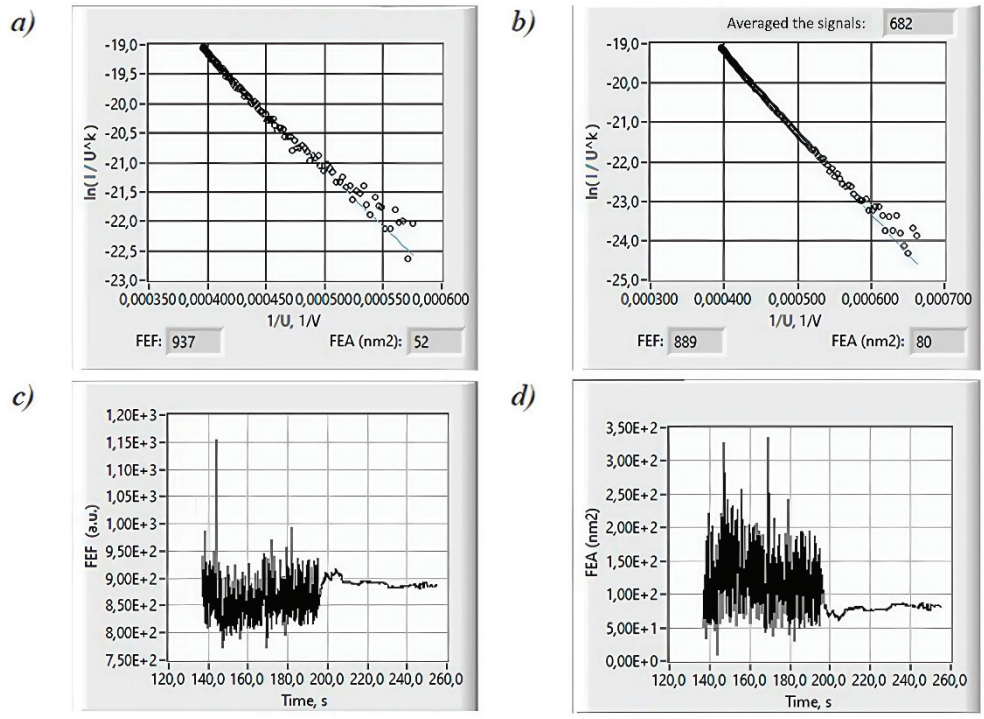

Fig. 3. Elimination of the noise component of the signals:
a – I-V characteristic-FN before averaging; *b* – I-V characteristic-FN after averaging;
time dependence: *c* – field enhancement factor FEF; *d* – emission area FEA

4. Conclusion

Software modules for correcting experimental I-V characteristics of field cathodes have been developed. The modules are integrated into the software of a multichannel data acquisition system with fast high-voltage cathode scanning and real-time data processing.

The developed method for eliminating random and systematic errors associated with noise and capacitive interference allows for correction of incoming data before real-time processing. As a result of the correction, the I-V characteristic becomes smoother, its hysteresis is reduced, and the range of measured currents increases (from 100 nA).

The method was tested in an experiment with a field cathode based on CNTs grown using PECVD. The correction resulted in a 5 % decrease in the field enhancement factor and a 54 % increase in the emission area.

5. Funding

The study was conducted under the State Assignment No. FFUG-2024-0031.

6. Conflict of interests

The authors declare no conflict of interest.

References

1. Kyritsakis A, Djurabekova F. A general computational method for electron emission and thermal effects in field emitting nanotips. *Computational Materials Science*. 2017;128:15-21. DOI:10.1016/j.commatsci.2016.11.010

2. Allaham MM, Knápek A, Mousa MS, Forbes RG. User-friendly method for testing field electron emission data: technical report. In: *Proceedings - 34th International Vacuum Nanoelectronics Conference (IVNC), 05-09 July 2021, Lyon, France:* IEEE; 2021. pp. 1-2. DOI:10.1109/IVNC52431.2021.9600769

3. Chubenko O, Baturin SS, Kovi KK, Sumant AV, et al. Locally resolved electron emission area and unified view of field emission from ultrananocrystalline diamond films. *ACS Applied Materials & Interfaces*. 2017; 9(38):33229-33237. DOI:10.1021/acsami.7b07062

4. Kopelvski MM, Galeazzo E, Peres HEM, Ramirez-Fernandez FJ, et al. Potentialities of a new dedicated system for real time field emission devices characterization: a case study. In: *Proceedings - 4th International Symposium on Instrumentation Systems, Circuits and Transducers (INSCIT), 26-30 August 2019, Sao Paulo, Brazil*: IEEE; 2019. p. 1-5. DOI:10.1109/inscit.2019.8868705

5. Gotoh Y, Kawamura Y, Niiya T, Ishibashi T, et al. Derivation of length of carbon nanotube responsible for electron emission from field emission characteristics.

Applied Physics Letters. 2007;90(20). DOI:10.1063/1.2740199

6. Reichert I, Olney P, Lahmer T. Influence of the error description on model-based design of experiments. *Engineering Structures*. 2019;193:100-109. DOI:10.1016/j.engstruct.2019.05.002

7. Ayari A, Vincent P, Perisanu S, Poncharal P, et al. Is the linear relationship between the slope and intercept observed in field emission S-K plots an artifact? *Journal of Vacuum Science & Technology B*. 2024;42(5). DOI:10.1116/6.0003828

8. Funayama K, Tanaka H, Hirotani J, Shimaoka K, et al. Noise modeling in field emission and evaluation of the nano-receiver in terms of temperature. *IEEE Access*. 2019;7:57820-57828. DOI:10.1109/access.2019.2913692

9. Persaud A. Analysis of slope-intercept plots for arrays of electron field emitters. *Journal of Applied Physics*. 2013;114(15). DOI:10.1063/1.4825051

10. Ji X, Yutong S, Yongjiao S, Wenxin Y, et al. Study on electrical properties and structure optimization of side-gate nanoscale vacuum channel transistor. *Journal of Physics D: Applied Physics*. 2020;53(13):135301. DOI:10.1088/1361-6463/ab642f

11. Di Bartolomeo A, Giubileo F, Iemmo L, Romeo F, et al. Leakage and field emission in side-gate graphene field effect transistors. *Applied Physics Letters*. 2016;109(2). DOI:10.1063/1.4958618

12. Koochack Zadeh M, Hinrichsen V, Kuivenhoven S. Measurement of field emission current during switching of capacitive current in vacuum. *Proceedings – International Symposium on Discharges and Electrical Insulation in Vacuum, ISDEIV (2010), 30 August 2010 – 03 September 2010, Braunschweig, Germany*: IEEE; 2010. p. 249-252. DOI:10.1109/deiv.2010.5625786

13. Arkhipov AV. Hysteresis of pulsed characteristics of field emission from nanocarbon films. *Technical Physics*. 2005;50(10):1353. DOI:10.1134/1.2103285

14. Popov EO, Kolosko AG, Filippov SV, Terukov EI, et al. Comparison of macroscopic and microscopic emission characteristics of large area field emitters based on carbon nanotubes and graphene. *Journal of Vacuum Science & Technology B*. 2020;38(4):043203.. DOI:10.1116/6.0000072

15. Kitsyuk EP, Vasilevskaya YO, Volovlikova OV, Eganova EM, et al. Catalytic particles formation from thin nickel films for the synthesis of multi-walled carbon nanotubes. *Carbon*. 2024;229:119509. DOI:10.1016/j.carbon.2024.119509

16. Popov EO, Kolosko AG, Filippov SV. A test for compliance with the cold field emission regime using the elinson-schrednik and forbes-deane approximations (Murphy-good plot). *Technical Physics Letters*. 2020;46(9):838-842. DOI:10.1134/s1063785020090096

17. Kolosko AG, Filippov SV, Popov EO. Influence of current-voltage characteristic processing methods on the value of effective parameters of field cathodes. *Fizika tverdogo tela = Physics of the Solid State*. 2023;65(12):2162. DOI:10.61011/FTT.2023.12.56749.5126k (In Russ.)

18. Jarvis JD, Andrews HL, Brau CA, Choi BK, et al. Adsorbate modification of emission from diamond field emitters and carbon nanotubes. In: *Proceedings of the 2009 Free-Electron Laser Conference*, *23-28 August 2009, Liverpool, UK*.

19. Popov EO, Kolosko AG, Chumak MA, Filippov SV. Ten approaches to define the field emission area. *Technical Physics*. 2019;64(10):1530-1540. DOI:10.1134/s1063784219100177

20. Djuzhev NA, Demin GD, Filippov NA, Evsikov ID, et al. Development of technological principles for creating a system of microfocus X-ray tubes based on silicon field emission nanocathodes. *Technical Physics*. 2019;64(12):1742-1748. DOI:10.1134/s1063784219120053

21. Masalov SA, Popov EO, Kolosko AG, Filippov SV, et al. Liquid-metal field electron source based on porous gap. *Technical Physics*. 2017;62(9):1424-1430. DOI:10.1134/s1063784217090171

Information about the authors / Информация об авторах

Sergei A. Sokov, Laboratory Assistant, Ioffe Institute, St.-Petersburg, Russian Federation; ORCID 0009-0005-5585-418X; e-mail: sokovclan@gmail.com

Mikhail S. Nechaev, Laboratory Assistant, Ioffe Institute, St.-Petersburg, Russian Federation; ORCID 0009-0008-3238-1668; e-mail: msnechaev@stud.etu.ru

Boris E. Mutygullin, Laboratory Assistant, Ioffe Institute, St.-Petersburg, Russian Federation; ORCID 0009-0003-7975-3151; e-mail: borlin93@gmail.com

Соков Сергей Александрович, лаборант, Физико-технический институт им. А. Ф. Иоффе РАН, Санкт-Петербург, Российская Федерация; ORCID 0009-0005-5585-418X; e-mail: sokovclan@gmail.com

Нечаев Михаил Сергеевич, лаборант, Физико-технический институт им. А. Ф. Иоффе РАН, Санкт-Петербург, Российская Федерация; ORCID 0009-0008-3238-1668; e-mail: msnechaev@stud.etu.ru

Мутыгуллин Борис Эдуардович, лаборант, Физико-технический институт им. А. Ф. Иоффе РАН, Санкт-Петербург, Российская Федерация; ORCID 0009-0003-7975-3151; e-mail: borlin93@gmail.com

Anatoly G. Kolosko, Cand. Sc. (Phys. and Math.), Senior Researcher, Ioffe Institute, St.-Petersburg, Russian Federation; ORCID 0000-0002-6073-6808; e-mail: agkolosko@mail.ru

Sergei V. Filippov, Cand. Sc. (Phys. and Math.), Senior Researcher, Ioffe Institute, St.-Petersburg, Russian Federation; ORCID 0000-0001-5325-2226; e-mail: f_s_v@list.ru

Eugeni O. Popov, D. Sc. (Phys. and Math.), Leading Researcher, Ioffe Institute, St.-Petersburg, Russian Federation; ORCID 0000-0003-2226-6304; e-mail: e.popov@mail.ioffe.ru

Колосько Анатолий Григорьевич, кандидат физико-математических наук, старший научный сотрудник, Физико-технический институт им. А. Ф. Иоффе РАН, Санкт-Петербург, Российская Федерация; ORCID 0000-0002-6073-6808; e-mail: agkolosko@mail.ru

Филиппов Сергей Владимирович, кандидат физико-математических наук, старший научный сотрудник, Физико-технический институт им. А. Ф. Иоффе РАН, Санкт-Петербург, Российская Федерация; ORCID 0000-0001-5325-2226; e-mail: f_s_v@list.ru

Попов Евгений Олегович, доктор физико-математических наук, ведущий научный сотрудник, Физико-технический институт им. А. Ф. Иоффе РАН, Санкт-Петербург, Российская Федерация; ORCID 0000-0003-2226-6304; e-mail: e.popov@mail.ioffe.ru

Received 24 June 2025; Revised 23 July 2025; Accepted 28 July 2025

Original papers
Nanostructured, nanoscale materials and nanodevices

УДК 004+531-2+535+620-22 DOI: 10.17277/jamt-2025-10-04-329-341

Topological laser thermodynamics in technologies for controlling the functional characteristics of high-entropy alloys with dendritic surface structures

© Darya D. Tumarkina[a], Oleg Ya. Butkovsky[a], Dmitry N. Bukharov[a]✉, Irina V. Burakova[b], Alexander E. Burakov[b], Sergey M. Arakelian[a]

[a] *Vladimir State University, 87, Gorky St., Vladimir, 600000, Russian Federation,*
[b] *Tambov State Technical University, Bld. 2, 106/5, Sovetskaya St., Tambov, 392000, Russian Federation*

✉ buharovdn@gmail.com

Abstract: This paper examines the laser thermodynamics of topological structures – dendrites – obtained by laser ablation of several high-entropy alloys using laser pulses. Laser experimental synthesis schemes and parameters for producing dendritic structures in various high-entropy alloys are discussed. For various configurations of such structures, the possibilities for controlling the functional characteristics of dendritic samples (electrophysics and optics) for potential technological applications are analyzed within nanocluster/island topological models. Thermodynamic conditions for targeted dendritic synthesis are modeled and evaluated under various experimental conditions with laser irradiation from a Gaussian radiation source using the Matlab Laser Toolbox approximation. The thermodynamic conditions for the synthesis of dendritic systems formed from high-entropy alloys are studied using analytical estimates of the temperature field. The procedure performed allowed us to estimate the actual melting temperatures for the components of the nanostructured high-entropy alloy. Models of dendritic structures in the diffusion approximation under diffusion-limited aggregation were proposed. Their electrical conductivity was estimated using simulations of the current-voltage characteristics within the tunneling and hopping approximations, as well as the enhancement of the electric field on fractal structures at their inhomogeneous boundaries. The developed models were implemented in MATLAB and were directly related to the parameters of the actual synthesis scheme, and the estimates obtained using them were consistent with the actual values.

Keywords: laser thermodynamics; high-entropy alloys; topological surface structures; directed synthesis of dendrites; controlled functional characteristics.

For citation: Tumarkina DD, Butkovsky OYa, Bukharov DN, Burakova IV, Burakov AE, Arakelian SM. Topological laser thermodynamics in technologies for controlling the functional characteristics of high-entropy alloys with dendritic surface structures. *Journal of Advanced Materials and Technologies*. 2025;10(4):329-341. DOI: 10.17277/jamt-2025-10-04-329-341

Топологическая лазерная термодинамика в технологиях управления функциональными характеристиками высокоэнтропийных сплавов с поверхностными дендритными структурами

© Д. Д. Тумаркина[a], О. Я. Бутковский[a], Д. Н. Бухаров[a], И. В. Буракова[b], А. Е. Бураков[b], С. М. Аракелян[a]

[a] *Владимирский государственный университет имени Александра Григорьевича и Николая Григорьевича Столетовых, ул. Горького, 87, Владимир, 600000, Российская Федерация,*
[b] *Тамбовский государственный технический университет, ул. Советская, 106/5, пом. 2, Тамбов, 392000, Российская Федерация*

✉ buharovdn@gmail.com

Аннотация: Рассматривается лазерная термодинамика топологических структур – дендритов, полученных при воздействии лазерных импульсов на поверхность ряда высокоэнтропийных сплавов в процессе лазерной абляции. Рассмотрены схемы лазерного экспериментального синтеза и его параметры для получения дендритных структур

высокоэнтропийных сплавов различного характера. Для разных конфигураций таких структур в рамках нанокластерных/островковых топологических моделей проанализированы возможности управления функциональными характеристиками образцов с дендритами (электрофизика и оптика) для возможных технологических применений. Смоделированы и оценены термодинамические условия направленного синтеза дендритов при разных условиях эксперимента с лазерным воздействием от Гауссового источника излучения в рамках приближения Matlab Laser Toolbox. Проведено исследование особенностей термодинамических условий синтеза дендритных систем, образованных из высокоэнтропийных сплавов на основе аналитических оценок поля температуры. Проведенная процедура позволила оценить реальные температуры плавления для компонент наноструктурированного высокоэнтропийного сплава. Предложены модели дендритных структур в диффузионном приближении в рамках диффузионно-ограниченной агрегации, для которых приведена оценка их электропроводимости с помощью моделирования вольтамперных характеристик в рамках туннельного и прыжкового приближений, а также усиления электрического поля на неоднородных границах фрактальных структур. Разработанные модели реализованы в среде MATLAB и имеют непосредственную связь с параметрами реальной схемы синтеза. Оценки, выполненные с их помощью, не противоречат реальным величинам.

Ключевые слова: лазерная термодинамика; высокоэнтропийные сплавы; топологические поверхностные структуры; направленный синтез дендритов; управляемые функциональные характеристики.

Для цитирования: Tumarkina DD, Butkovsky OYa, Bukharov DN, Burakova IV, Burakov AE, Arakelian SM. Topological laser thermodynamics in technologies for controlling the functional characteristics of high-entropy alloys with dendritic surface structures. *Journal of Advanced Materials and Technologies*. 2025;10(4):329-341. DOI: 10.17277/jamt-2025-10-04-329-341

1. Introduction

The effect of laser radiation on the surface of a solid material is a multifactorial and controllable process under conditions of selected laser beam sizes and pulse durations, particularly when producing inhomogeneous dendritic surface structures.

This dimensional processing of the surface by laser radiation results in a topological modification of its structure under conditions of complex interactions between different phases of the substance during the development of nonlinear gas- and hydrodynamic processes with different spatiotemporal parameters, including micro- and nanoscale clusters. The emergence of such dynamic small-scale instabilities radically alters the thermodynamic phase and structural states of the medium, with parameters whose local values differ from those tabulated for bulk samples.

This specific feature of the laser experiment is of particular interest for complex/composite compounds, particularly high-entropy alloys (HEAs) of varying elemental/chemical composition [1, 2]. Precisely by applying laser radiation, it is possible to control the thermodynamic conditions for the formation of localized 3D columnar-dendritic structures of a fractal type, for example, on the metal surface of a sample, given the specific conditions of non-stationary energy exchange between light radiation, electronic states, and the lattice parameters of the solid. All this determines the final temperature regime and phase state of the medium with controlled functional characteristics.

This controlled laser radiation effect on a metal surface is particularly unique when applied in a sequence of laser pulses (multi-pulse mode). This allows for the selection of a specific time delay between pulses and the recording of the fundamental processes of sequential heating and cooling of the material, depending on the thermodynamic energy parameters of the alloy components, with specific melting conditions and the required deformation/pit configurations on the surface (including at the melting front). This also enables the time-lapse recording of the material's solidification conditions, including amorphization and crystallization processes, as well as oxidation under transient conditions.

Of fundamental importance in this case is the emerging localized thermophysical source, often moving in different regions on the material's surface. Its spatiotemporal characteristics require specialized analysis and modeling to ultimately produce a stable structure with the desired functional and structural properties of a 2D thin-film system of varying thickness.

Under conditions where the laser beam is scanned across the surface, dendrites in the melted zone form at a certain angle to the sample surface due to an additional temperature gradient along the direction of the laser beam's movement across the surface. Physical significance, in terms of thermal heating, is typically derived from a dimensionless control parameter such as the product of the laser focal spot size on the surface of the metal alloy and its absorptivity.

These issues are addressed in this paper for HEA of different chemical composition with a laser-induced dendritic structure. Emphasis is placed on the

fractal nature of the resulting configurations in terms of the thermodynamic and thermophysical processes that drive their development, along with the corresponding energy potentials for mixing thermodynamic quantities for alloys (in particular, entropy and enthalpy). This ultimately determines the structural and functional characteristics of samples with such synthesized surface topological structures. To analyze these characteristics, depending on the specific experimental conditions of the laser experiment, the authors conduct numerical modeling of the thermophysical processes that lead to various similar structural configurations on the surface.

2. Methods and approaches

This section briefly discusses schemes for obtaining a number of topological configurations that arise on the surface of a material under the influence of laser beams, and simple models of the electrophysical characteristics of such structures.

2.1. Laser action on the surface of a material and analysis of the implementation of inhomogeneous structures of the dendritic/fractal type on it

Initially, solid-phase laser modification of the surface of various metal-containing materials occurs under the influence of laser radiation. However, this laser ablation process occurs over a relatively narrow range of laser power values. Therefore, to determine the upper energy limit, above which melting of the sample is observed, we simulated the metal sample while scanning the laser beam. This allows us to subsequently calculate the configuration and composition of the resulting spatially distributed structure at the end of laser surface modification.

Since in typical cases for a metal surface the thermal diffusion length (~1 mm) ($l_d \sim \sqrt{D\tau}$, $D \sim 10^{-5}$ m^2s^{-1} is thermal diffusion coefficient, $\tau \sim 0.1$ s is exposure time, then $l_d \sim 10^{-3}$ m) along the normal to the surface during the exposure time of the laser beam is much greater than the absorption length of the laser radiation (~10 μm), then the heat source can be considered superficial, which determines the direction of heat flow from this source.

A model of the laser heating process under conditions of surface film formation has been considered in many papers [1, 2]. The authors used calculations in the Matlab environment using library functions implemented in Matlab Laser Toolbox [3]. The intensity distribution $I(x, y)$ of laser radiation in the form of a Gaussian beam on the plane of the irradiated film (XOY) was specified as:

$$I(x,y) = \frac{8P}{\pi d_f^2} \exp\left[-\left(\frac{2\sqrt{2}}{d_f} \right)^2 \left(x^2 + y^2 \right) \right], \qquad (1)$$

where P is laser radiation power, W; d_f is beam diameter at the target surface, m.

The temperature field $T(x, y)$ of a moving surface heat source (its current coordinates are marked with a prime) in the quasi-stationary case can be represented as:

$$T(x,y) = \int_{-\infty}^{\infty} \int AI(x',y')W(x,y,x',v)dx'dy', \qquad (2)$$

where $W(x,y,x',v) = \frac{1}{2\pi KR} \exp\left(-\frac{v}{2a}(x - x' + R) \right)$,

and $R = \sqrt{x^2 + y^2}$, A – absorption capacity in a material, K is thermal conductivity, $W \cdot (m \cdot K)^{-1}$, $a = K/\rho c_p$ is thermal diffusivity, $m^2 \cdot s^{-1}$, v is scanning speed, $m \cdot s^{-1}$, ρ is medium density, $kg \cdot m^{-3}$ and c_p is specific heat capacity of the material, $J \cdot (kg \cdot K)^{-1}$.

Expression (2) is calculated, for example, using the fast Fourier transform [4].

Using expressions (1) and (2), we calculated the temperature field distribution on the target surface (the specific chemical composition of the HEA is shown below in Fig. 1) in a square, flat computational domain measuring 400 μm. These calculations allowed us to establish an upper limit for the laser power beyond which sample melting occurs. At laser power levels of no more than 10 W, the maximum calculated temperature field values did not exceed the numerical values for melting to occur, i.e., surface deformation – in our case, nanomodification – occurred.

In order to study the physics of the processes occurring during such laser modification of the surface, detailed experiments were previously carried out with well-studied materials, the processes in which can be considered as test ones within the framework of an analogy for the case of HEA materials studied by us in this article: semiconductors, in particular, lead telluride, PbTe [5]; metallic ones, in particular, from the noble metals silver Ag, gold Au and their alloys [6]; metal-carbon and diamond-like compounds of different compositions [7–9]. In this case, the emphasis is placed on various schemes and modes of laser modification of the surface with controlled synthesis

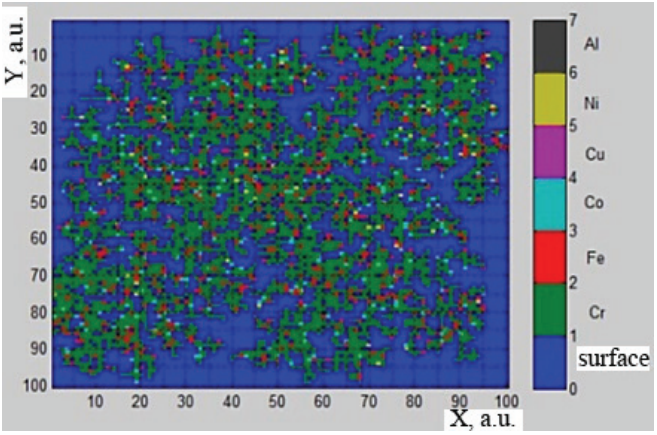

Fig. 1. Representative image of HEA dendritic nanostructures, with their chemical composition depicted by different colors (in relative units)

of topological cluster structures of a certain fractal-type configuration in thin-layer systems on a solid surface. Modeling of the occurring thermal diffusion processes and the implementation of inhomogeneous topological structures of different configurations on the surface of the material are possible using solutions of the two-dimensional diffusion equation [10].

Since, in principle, such methods and approaches for synthesizing such heterogeneous and disordered structures are quite universal, they are also feasible for our problem of HEA with dendrite formation, at least during the initial stage of exposure to a laser pulse with a specific time profile. Basic approaches for such consideration are provided in (Supplementary materials 1).

A typical view of the dendritic microstructure we obtained for HEA is shown in Fig. 1, which shows an image of the dendritic configuration taking into account the HEA elemental composition (shown on the scale on the right in the figure, with the corresponding color). This composition was determined using X-ray microanalysis. The image is given in relative units, taking into account model processing of the image.

We previously considered a number of examples of model heterogeneous nanostructures [8, 9] using certain parameters, including fractal dimension, and taking into account the height of the formed dendrites, which were also recorded in the AFM imaging experiment.

These models allow us to estimate the sizes of the formed dendrites. Converting to absolute sizes, taking into account the 10 nm side length of the computational domain cell, we obtain minimum coverage circle radii for the bases of the formed dendritic clusters in the order of 100–400 nm.

The dimensions of the crystallized metal blocks after laser ablation are several tens of nanometers, which is an order of magnitude smaller than the inhomogeneities in the original sample. The cladding processes for a pre-applied alloy coating to the sample surface, followed by its solidification after rapid cooling, are not considered here. It can be argued that the formation of high-energy electron transport dendrites on the surface of, for example, stainless steel, is an adiabatic thermodynamic process of their synthesis [10]. Dendrites are precursors to the formation of crystalline structures.

2.2. Electrical conductivity models

Existing approaches to assessing the functional characteristics of this type of dendritic structure, in particular, models of electrical conductivity of disordered structures, which include nanocluster/ island surfaces with nanoclusters, are determined by the surface structure and its dendritic features. In general, to assess the electrical properties of heterogeneous structures of various configurations – nanocluster/island films/dendrites with disconnected topology, where there is no continuous conductivity path – the electric current between adjacent nanoclusters is considered. Within this approach, nanoclusters/islands are represented as potential wells, and the spaces between them act as potential barriers [11].

The emission of charge carriers into the surrounding medium or onto the substrate itself, as well as direct or hopping electron tunneling, forms the mechanism for charge transfer between nanoclusters of different configurations located on a solid surface.

Isolating the conductivity path in such a structure within the framework of the applied approach [12] allows us to evaluate the current-voltage (I–V) characteristics of the system (the dependence of current I on voltage U).

Depending on their topological features, such surface cluster structures with dendrites can be divided into two types of samples: those with a fairly dense arrangement of dendrites and those with a sparse structure.

In the first type of samples, topological clusters are connected to each other by "bridges," forming a connected topology that allows for the identification of a continuous current path with percolation-type electrical conductivity [5]. The I–V characteristic for this case is calculated using the standard relation (Ohm's law).

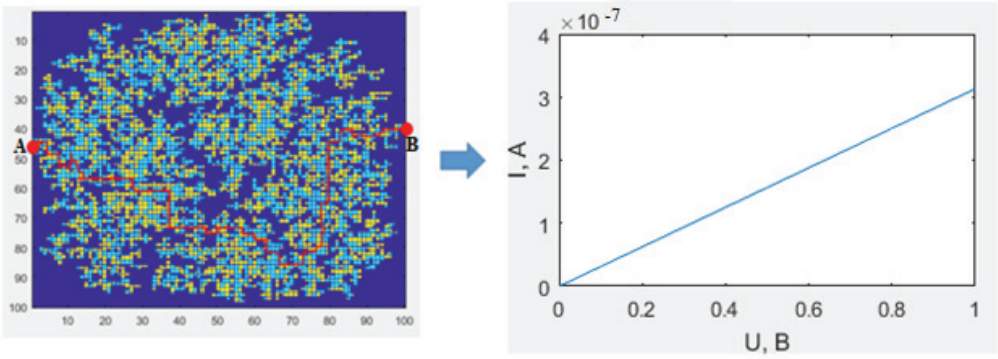

(a) *(b)*

Fig. 2. Model of a HEA film with a highlighted conductivity path *AB* (*a*);
I–V characteristics of the film for path *AB* with a test grain size of 10 nm (*b*)

The second type of samples possess fairly large distances between nanoclusters/islands and can be characterized by dielectric conductivity mechanisms, in which the electrical conductivity cluster forms a disconnected set, resulting in the absence of a continuous current path, and hopping electrical conductivity mechanisms in various manifestations [7, 11].

For these cases, mathematical modeling of the electrophysical properties of such dendritic structures is well known and has also been performed by the authors [8, 12]. The general scheme of such a process is based on DLA (diffusion-limited aggregation) modeling for percolation-type electrical conductivity [8, 10].

Figure 2 shows a model of a nanocluster/island HEA-nanofilm possessing this percolation type of conductivity, with a distinguished conductivity path and the corresponding I–V characteristic. The structure (Fig. 2*a*) was modeled on a computational domain of 100×100 relative units, within the framework of the DLA model, with a value of the probability of adhesion (*s*) of particles during their agglomeration equal to 0.5, and a random initial distribution of 10 seed particles at an equal concentration of HEA elements. In the film structure, specified points of microcontacts for voltage application (*A* and *B* points) are distinguished. Using the Lee wave algorithm [9, 12, 13], a continuous conductivity path is realized, taken as the shortest trajectory of electron motion in the nanofilm (*AB* broken line), the length of which *L* is 163 relative units. To calculate the current-voltage characteristics in test model units, the size of the structure granule corresponding to the cell size of the calculation region was chosen equal to d_{m1} = 10 nm.

Thus, hopping conductivity is realized as a process of charge carrier transport through localized centers [7, 13].

For a random distribution of localization centers, the electrical resistance R_{03} takes the form [14, 15]:

$$R_{03} = \frac{\pi\hbar a}{3.84q^2}\exp\left(\frac{1.24}{aN^{1/3}}\right), \qquad (3)$$

where N is concentration of localization centers m^{-3}, q is electron charge C, $\hbar$ is reduced Planck constant.

In connection with this approach (its basic principles are analyzed in (Supplementary materials 2), it is useful to briefly examine the model of electric field amplification in fractal structures such as those shown in Figs. 1 and 2*a*. As can be seen, in their simplest model representation, they include arbitrarily oriented elements in the form of variously sized fragments of long branches with fractal segments at their ends.

Thus, this analysis demonstrates that, using model samples and the proposed approximation, it is possible to achieve a relative enhancement of the electric field by several orders of magnitude, taking into account the entire perimeter of the branched fractal figure in a specific region of the coating when measured with a certain cross-section of the microcontact end. This effect is analogous to the well-known phenomenon of the realization of supersonic Raman scattering (SERS) with enhancement on a rough surface, used, in particular, in the diagnostics of extremely low concentrations of dyes on such surfaces [11, 16–18].

3. Results and Discussion

3.1. General characteristics of thermophysical laser action in the experiment

When using laser heating in HEA, it is necessary to consider the specific nonlinear temperature dependence of the material's characteristics and the microstructure of the resulting objects. This is the

subject of separate research, particularly in terms of potential applications, which is beyond the scope of this article.

This section presents the calculation results for processes in an HEA system under laser irradiation of the material surface, using fairly universal fundamental approaches to the thermodynamic description of laser heating. We also analyze some aspects of the conditions for the formation of inhomogeneous structures on the surface of samples in the corresponding temperature ranges under laser irradiation of materials (if necessary, these conditions can be adjusted for the specific elemental composition of the HEA in different schemes).

We will take into account the technologically important multi-pulse nature of radiation with a repetition rate of laser pulses f in the form of a simple dependence:

$$I(t) = I_0(t)(1-\cos f\,t),$$

where $I_0(t)$ is a slowly changing function over time, taking into account the difference in amplitudes in the sequence of pulses/peaks of different origin in each pulse [1, 2, 19, 20].

Then, in the one-dimensional approximation of the propagation of the thermal field along the *OX* axis in the quasi-stationary case, when the current value of t is considered within the general envelope of the laser pulse duration, for the temperature *T* we have [20]:

$$T(x,t) = \left(\frac{2w_0\sqrt{\beta t}}{a}\right)\mathrm{ierfc}\left[\frac{x}{2\sqrt{\beta t}}\right], \qquad (4)$$

w_0 is energy density of laser radiation flux, J·m^{-3}; β is thermal diffusivity coefficient, $\beta = a/(c\rho)$ m^2·s^{-1}; *a* is thermal conductivity, W·(m·K)$^{-1}$; ρ is density, kg·m^{-3}; *c* is specific heat capacity, J·(kg·K)$^{-1}$; and parameter

$$\mathrm{ierfc} = \int_z^\infty \mathrm{erf}\,c(z)\,dz = \left(\frac{1}{\pi^{1/2}}\right)\mathrm{e}^{-z^2} - z\,\mathrm{erfc}(z)$$

is the integral of the probability integral function. It is assumed that the radius of the laser heating spot focused on the material, r_f is much greater than the spatial scale of thermal diffusivity, β, for the time being considered, *t* .

The paper examines dendrite growth perpendicular to the sample surface, and the parameter *x* determines its height.

For example, an estimate for iron yields a value of *x* ~50 μm.

On the surface of a thin plate $x = 0$, i.e. when its thickness *h* is much smaller than the radial dimensions of the laser heating region under consideration $r = r_f$ and under the condition that $t \le 0.2\,r_f^2/\beta$, instead of expression (4) we have a simpler relationship:

$$T(0,t) = \frac{\left(\frac{w_0 t}{ch}\right)(1-4\beta t)}{r_f^2}\exp\left(-\frac{r_f^2}{4}\beta t\right). \qquad (5)$$

The analysis of the problem shows that the maximum heating temperature depends on two dimensionless parameters: a nonlinear function of temperature and the material's density. Moreover, for short periods of time, i.e., at the onset of the laser pulse, the temperature field in the material is determined by the energy flux density distribution function w_0 on the sample surface, for which the result of the one-dimensional heating problem with a constant heat source, multiplied by the value of w_0, is applicable.

The fundamental parameter in the problem under consideration is the required value of the laser radiation flux density *q*, at which the maximum temperature $T_{\max}$ is reached on the sample surface by the end of the laser pulse and at which melting of the material occurs. Without dwelling on the corresponding analytical relations (these processes are considered, for example, in [21]), we will immediately present numerical estimates of the critical values q_c based on these relations for the onset of melting of the material at normal pressure. In particular, for steel (SHX-15) with thermal conductivity $\alpha = 0.51$ W·(cm·K)$^{-1}$, volumetric heat capacity $c = 0.15$ cm^2·s^{-1}, $q_c = 3.5\cdot10^3$ W·cm^{-2} we have achieved the value $T_{\max} = 1808$ K with a laser pulse duration of 1 ms. With a duration of 10^{-8} s the required value q_c for melting the material $q_c = 1.8\cdot10^5$ W·cm^{-2}.

In this case, q_c increases for different materials with increasing melting point, thermal conductivity, and specific heat capacity. However, the q_c value decreases with increasing laser pulse duration. For example, for titanium, $T_{\max} = 2073$ K, $a = 0.15$ W·(cm·K)$^{-1}$, $c = 0.06$ cm^2·s^{-1}. For the noted laser pulse durations of 1 ms and 10^{-8} s, we have q_c, values of $3.0\cdot10^3$ W·cm^{-2} and $1.0\cdot10^5$ W·cm^{-2}, respectively.

When considering the rate of movement of temperature phase transition boundaries (along the

time coordinate), which determine dendrite growth, in this non-stationary problem, the region where exponential growth toward a fixed value of a given melting temperature is of fundamental importance.

However, during multi-pulse laser irradiation of a material, for example, for a pair of successive pulses, two parameters must be evaluated: the heating rate from the first pulse and the subsequent cooling of the material until the arrival of the second pulse, with a certain time delay δt (Supplementary materials 1). Then, according to the physics of the phenomenon under consideration, the heating and subsequent cooling of the material from the first pulse is limited in time by the arrival of the next pulse with a selectable delay δt, which determines the role of the time duration t of the dendrite growth process under the influence of the first pulse.

Thus, it becomes possible to regulate the modes of thermophysical processes during multi-pulse exposure of laser radiation to materials with controlled production of different dendritic configurations over time, and this can also be done in different areas of the surface with a given scanning of the laser beam over the surface.

3.2. Features of HEA systems

The above discussion applies to a material with a homogeneous elemental composition. Therefore, for HEA, a comprehensive analysis must be conducted, taking into account thermal diffusion effects for the various chemical components of the alloy. It also takes into account that the maximum laser heating temperature shifts toward a less thermally conductive material to a greater extent the longer the laser pulse duration [10, 20].

We consider several of the obtained dependencies within the framework of the general approach outlined above. In doing so, we will significantly simplify the problem for the case of only two consecutive laser pulses with specific characteristics acting on the HEA (with the formation of dendrites).

In this model, we will assume that laser radiation induces two layers in depth with defined boundaries, taking into account the sequential heating and cooling processes [22]. The first layer (with an average thickness of about 1 μm) has a columnar-dendritic structure, mainly of martensite; the second has a fine-grained structure with retained austenite (with average grain sizes of up to twenty micrometers and a temperature gradient across the depth of the laser-impact zone of the order of several tens of micrometers). Their characteristics are determined by the rates of amorphization, crystallization, and heat-diffusion processes in the material for different HEA components, as well as by the laser irradiation modes with a time interval between two successive pulses.

Furthermore, when exposed to millisecond-duration laser pulses in an air atmosphere, metal oxidation processes occur (with oxide film thicknesses of up to fractions of a micrometer). The kinetics of metal oxidation depends on the thermal effect of laser radiation integrally (on a two-component system), taking into account the growth of the oxide component. These phenomena are well known in materials science [23, 24], but are discussed below with corresponding numerical estimates for a specific HEA composition.

The subject of the study is HEA with chemical elements in AISI 304 stainless steel, with their percentage concentrations presented in Table 1 [25], before laser irradiation. A series of experiments were conducted with this material under double-pulse irradiation in the non-uniform laser pulse (M-pulse) model [22]. This multicomponent material decomposes at a temperature of 1067 K. However, here we are specifically talking about HEA-type alloy, since it requires comparable concentrations of its constituent chemical elements.

According to [22], on such a substrate, where HEA is located, the areas of formation of dendrites with their most uniform distribution over the surface are realized in the temperature range [608–800 K].

Our analysis of the scheme of this two-pulse action on the material led to the results presented in Table 2 and in Figs. 3 and 4 for the selected parameters of the laser experiment.

Using Matlab, the authors obtained a temperature distribution field on a stainless steel substrate under parabolic growth conditions (Fig. 5).

Table 1. Concentrations of chemical elements (wt. %) in stainless steel AISI 304

C	Cr	Ni	Si	Mn	S	P	N
0.08	18–20	8–10.5	1	2	<0.03	0.045	0.06

Table 2. Temperature of the substrate with formed HEA (stainless steel) depending on the time of exposure to 2-pulse laser ablation

t, ms	0	3/2	3	9/2	6
$T(t)$, °C	300	469	433	506	300

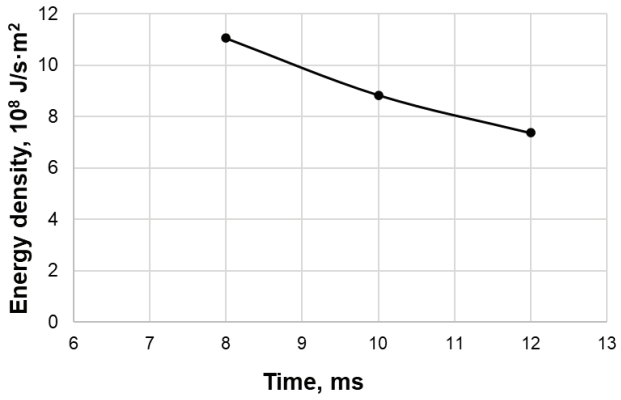

Fig. 3. Dependence of the laser energy density acting on the sample on the exposure time as a result of 2x ablation on the surface of a stainless steel substrate with formed HEA

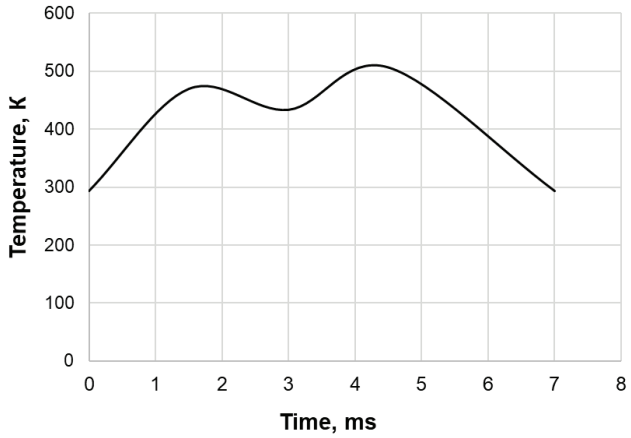

Fig. 4. Dependence of the temperature of the stainless steel substrate with the formed HEA on the total time of exposure to two laser ablation pulses

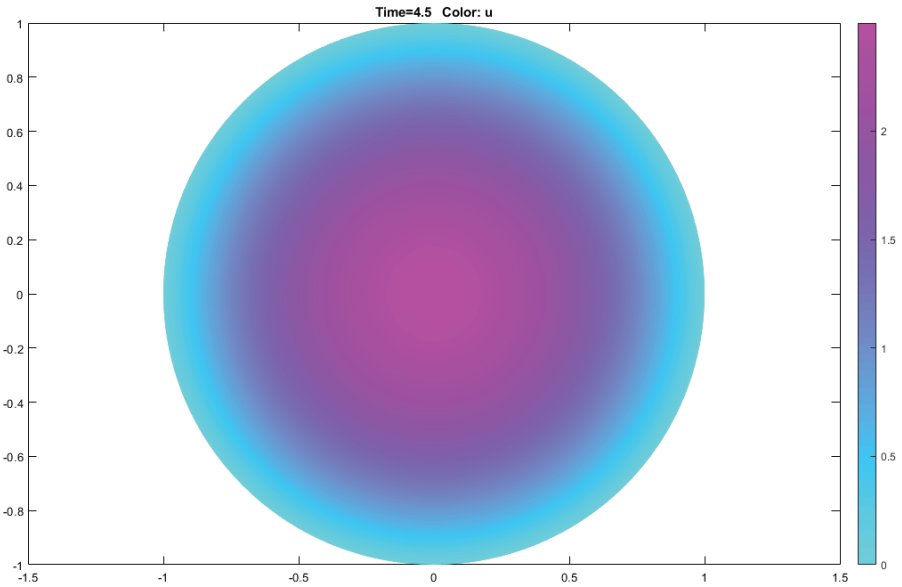

Fig. 5. Temperature field on a stainless steel substrate with HEA formed as a result of 2-pulse ablation. Calculations were performed in Matlab; with an exposure time of 1 ms, a temperature of 335 °C is reached; with an exposure time of 1.5 ms, this corresponds to 608 °C; with an exposure time of 3 ms, this corresponds to 964 °C

The initial conditions for the calculation were the initial and final temperatures of the laser exposure, and the total exposure time intervals (on the left side of the figure) were 1, 1.5, 3 ms (shown in different colors on the right scale).

In the above-described two-pulse laser irradiation scheme, the concentration of each HEA impurity was calculated for the temperature gradient formed during the second pulse, and the melting temperature of each impurity was also calculated. This can be accomplished using Fick's second law [10, 20, 24]:

$$\frac{C_x}{C_0} = 1 - \mathrm{erf}\frac{x}{2\sqrt{D\tau}}, \qquad (6)$$

where C is concentration of diffusing substance in a film with thickness x, m^{-3}; C_0 is initial concentration of the diffusing substance in the liquid, m^{-3}; erf is error function with tabulated values [26]; x is layer thickness, m; D is diffusion coefficient, $m^2 \cdot s^{-1}$; τ is diffusion time, s. This makes it possible to calculate the concentration of impurities after exposure to the first laser pulse.

Diffusion coefficient values D in HEA for each ion (Cr^+, Ni^+, Mn^+, C^+, Fe^+) are tabulated [20] and are equal to: $D(Cr^+) = 0.01 \cdot 10^{-4}$ $m^2 \cdot s^{-1}$; $D(Ni^+) = 21.9 \cdot 10^{-4}$ $m^2 \cdot s^{-1}$; $D(Mn^+) = 7.5 \cdot 10^{-4}$ $m^2 \cdot s^{-1}$; $D(C^+) = 0.33 \cdot 10^{-4}$ $m^2 \cdot s^{-1}$; $D(Fe^+) = 0.0062 \cdot 10^{-4}$ $m^2 \cdot s^{-1}$.

Given the processes of laser oxidation, the dependence of the thickness $h(r, t)$ of the oxide film on the temperature on the surface of stainless steel was obtained under the assumption of a parabolic law of its growth [23, 24, 27]:

$$h(r,t) = \sqrt{2t\omega_0(-Q/T(r))}, \quad (7)$$

where $h(r, t)$ is film thickness, m; t is laser pulse duration, s; r is transverse coordinate, m; Q is oxidation activation temperature, equal to approximately 1143 K; $T(r)$ is maximum heating temperature, K; ω_0 is parabolic constant of the oxidation growth rate, which under dry oxygen conditions at temperature ~1100 K is equal to 0.027 $\mu m^2 \cdot h^{-1}$ [23, 24].

Thus, at a stainless steel surface temperature of 1860 K and a laser pulse duration of 6 ms, the oxide film thickness is 0.7 nm.

The melting point of the stainless steel components involved in dendrite formation was also calculated.

According to [28–30], difference in chemical potentials of components is $\Delta\mu = -q(T_0 - T)/T_0$, where T_0 is melting point of the components, K; T is phase transition temperature. According to [22, 31] it equals to 1067 K, and we have that $q = \frac{\sum \mu_i n_i}{T}$ is latent heat of phase transition, where is concentration of the i-th component of HEA. Taking into account each concentration n_i the HEA component: $\sum n_i = \frac{k}{s} \rho S_{surf}$, where k is Boltzmann constant, $J \cdot K^{-1}$; S is surface entropy, $J \cdot (K \cdot m)^{-2}$; ρ is dendrite distribution density, m^{-2}; S_{surf} is surface area, m^2.

On the other hand, $\Delta\mu$ is an additive quantity, therefore $\Delta\mu_i = \mu_{li} - \mu_{si} = q(T_0 - T)/T_0$ is the difference in chemical potentials of the i-th component, which is equal to the difference in chemical potentials for the liquid and solid states of the component, T_i is melting point of the component, K. In this case $\sum \mu_i n_i = \Delta G$ [30], where G is the Gibbs free energy unit, J. Therefore, we arrive at the expression [31]: $q\frac{T_0 - T}{T_0 T R} = \frac{1}{n}$, where n is the number of particles of a given component.

Let us consider the concentrations of the HEA components in the oxide film [23, 24].

For the differential $d\gamma$ from the surface tension of a flat surface, we have according to [30]:

$$d\gamma = -M_1 d\mu_1 - M_2 d\mu_2 - \ldots - M_6 d\mu_6,$$

where M_i is the excess number of moles of the i-th component ($i = 1, \ldots, 6$) per unit area of the interfacial layer.

Then we write:

$$x_1 d\mu_1 + x_2 d\mu_2 + x_3 d\mu_3 + x_4 d\mu_4 + x_5 d\mu_5 + x_6 d\mu_6 = 0,$$

where x_i is molar fractions of components.

Thus, for a separate (in particular) component $i = 6$, we have

$$d\gamma = \left[M_6 - \frac{x_6}{x_1 M_1 + x_2 M_2 + x_3 M_3 + x_4 M_4 + x_5 M_5} \right] d\mu_6$$

or, introducing the appropriate notation, we have $d\gamma = M_{6(12345)} d\mu_6 = M_{6(12345)} R T\, d \ln c_6$, where R is universal gas constant, $J \cdot (mol \cdot K)^{-1}$; T is the melting point of the 6th component K; c_6 is the concentration of the 6th component, m^{-1}.

Similar equations are valid for all components. Since the alloy is equimolar (high-entropy), we assume that $M_1 = M_2 = \ldots = M_6$. However, in HEA, the proportions of each component range from 0.05 to 0.3, depending on the total number of components – N. This corresponds to the generally accepted concept of HEA and can be a controlling parameter, along with chemical composition and concentrations, in the synthesis of specific HEA.

From here, for $d\mu_i$ we obtain:

$$d\mu_i = \frac{\Delta G_i}{n_i} = RT \ln \frac{n s}{k}. \quad (8)$$

In this case, if we consider the thermal decomposition reaction as endothermic, we can determine the amount of heat required for melting each impurity, taking into account the heat input from laser heating and melting. We will express this in terms of temperature based on the relationship between the concentrations of substances in the liquid layer:

$$n = \frac{R T_0 T}{q(T_0 - T)}.$$

Then from [30–32]:

$$\frac{\Delta G_i (T_0 - T)}{T_0 T} = RT d \ln \frac{T_0 T}{T_0 - T}.$$

Now we can find the melting temperatures of the particles for the HEA elements of interest to us (Cr, Ni, Mn, C, Fe).

Let us assume that as a result of oxidative destruction, an atomic monolayer of impurities is formed on the surface of stainless steel. Then, from the phenomenological thermodynamic model for describing the melting temperature of nanoparticles of materials [32], we obtain the following two expressions

$$4\pi\left(\frac{\delta}{2}\right)^2 d = \frac{4}{3}\pi\left(\frac{\delta}{2}\right)^3, \quad (9)$$

where δ is Tolman's constant, m; d is atomic monolayer height, m;

$$T_m = T_m^{(\infty)} \exp\left(-\frac{4\delta}{\delta + 2R}\right), \quad (10)$$

where $T_m^{(\infty)}$ is melting point of a bulk sample, K; r_0 is radius of a particle/cluster (in our case, an atom), m.

The obtained melting temperatures of massive samples $T_m^{(\infty)}$ [30, 32] and the atomic radii$r_0$of metals are given in Table 3 [33].

Using the data from Table 3, we obtain the calculated values of the melting temperatures T_m, but for the nanoparticles of the HEA components. This gives the following numerical values: for C – 129 K, for Cr – 90 K, for Fe – 74 K, for Ni – 74 K, for Mn – 64 K. For different HEA elements, we have the following values of n: 0.13 for C; 0.09 for Cr; 0.07 for Fe; 0.07 for Ni; 0.06 for Mn.

Thus, using the proposed approach, it is possible to estimate the actual melting temperatures of the components of nanostructured HEA. This will determine their potential use in various applications for specific purposes.

Table 3. Data on the melting temperature of massive samples T_m for HEA of the elemental composition under consideration

Chemical element	$T_m^{(\infty)}$, K	r_0, nm
C	3800	0.091
Cr	2150	0.130
Fe	1806	0.126
Ni	1725.4	0.135
Mn	1517	0.132
O	1860	0.386

3.3. Prospects and background for the application of nanostructured HEAs

Such high-entropy perovskites of the dendritic fractal type hold great promise for various applications, particularly in electrophysics.

According to the physics of the phenomenon itself, the reduction of a metal (stainless steel) from a perovskite modeled on experimental data results in the formation of an oxide film on the dendrite surface. Upon reduction, this perovskite transforms into a martensite structure. This occurs due to the interaction of the perovskite (essentially an ore [34]) with atmospheric carbon monoxide. This assumption is based on the fact that the carbon content in the crystal lattice increases. Moreover, according to the same work [34], the charge in the oxide lattice is compensated, so there are no free electrons in the oxide lattice, and charge transfer within the lattice is carried out only by ionic displacements. With a change in the structure of the electric field in the medium, only paired, and therefore neutral, thermal objects are formed in the ionic lattice of the perovskite – interstitial defects and Frenkel defects, or Schottky defects. Therefore, the electrical conductivity of such a lattice is due to the presence of defects, and such a formed oxide is characterized by conductivity similar to superionic conductors. However, the difference lies in the rapid mixing of particles and vacancies due to the thermal effect, and therefore "short-lived" conductivity occurs in oxides.

The temperature at which high electrical conductivity appears is determined by the Tammann melting point [1, 2, 10, 20]: $(0.5 – 0.8)T_m$ (essentially room temperature, according to Table 2 and Fig. 4, where the first temperature gradient corresponds to the melting of the stainless steel surface), at which surface diffusion begins to transform into bulk diffusion. It is at this temperature that significant interaction between oxides and carbon occurs. All components of the carbon that make up the perovskite will participate in this conductivity.

4. Conclusion

In this article, we analyzed the structural features of high-entropy alloys with laser-induced dendritic structures using topological laser thermodynamics approaches and models of surface laser structures of various configurations. The laser methods for influencing the material surface with the implementation of inhomogeneous dendritic/fractal structures were considered. As a result, existing approaches for considering thermophysical processes

in such topological structures were briefly analyzed. The diffusion processes and implementation of inhomogeneous topological structures of various configurations on the material surface with the formation of dendrites in a laser experiment were simulated. When examining the effects of laser thermodynamics of HEA systems, we estimated the numerical values of the thermodynamic parameters in nanostructured samples, in contrast to the values for tabulated bulk samples. Details of calculations based on the various algorithms used were provided. This makes it possible to mathematically model the electrical properties of dendritic structures using a nanocluster/island nanofilm model, estimating the local field enhancement in the resulting dendritic structures. The analysis and estimated calculations presented in this paper, taking into account the thermodynamic conditions and criteria for the existence of HEA, specifically the ranges of numerical values of entropy and enthalpy, differences in the mole fractions of elements, and latent heats of fusion, suggest the possibility of a perovskite-like high-entropy compound and its martensitic transformation. This requires further verification in future studies.

5. Supplementary Materials

https://disk.yandex.ru/i/zkKkS1WLVHZkUw

6. Conflict of interest

The authors declare no conflict of interest.

References

1. Panchenko VYa. *Laser technologies of materials processing: modern problems of fundamental research and applied developments*. Moscow: FIZMALIT; 2009. 664 p. (In Russ.)
2. Grigor′yants AG, Shiganov IN, Misyurov AI. *Technological processes of laser processing: Studies. Handbook for universities*. Moscow: BMSTU Publ. House; 2006. 664 p. (In Russ.)
3. Römer GRBE, Huis In ’T Veld AJ. Matlab laser toolbox. *Physics Procedia*. 2010;5:413-419. DOI:10.1016/j.phpro.2010.08.068
4. Kandidov VP, Chesnokov SS, Shlenov SA. *Discrete Fourier transform. Study guide*. Moscow: Lomonosov MSU Publ. House; 2019. 88 p. (In Russ.)
5. Bukharov DN, Osipov AV, Arakelyan SM, Kucherik AO. Graph-analytical model of the electrical conductivity of a semiconductor island plumbum telluride nanofilm. *Journal of Physics: Conference Series*. 2019; 1331:012008. DOI:10.1088/1742-6596/1331/1/012008
6. Arakelyan SM, Khudaberganov TA, Istratov AV, Osipov AV, Khor′kov KS. Topological laser-induced quantum states in nanocluster structures: fundamental effects and possible applications (electrophysics and optics). *Optika i spektroskopiya = Optics and Spectroscopy*. 2019;127(7):125-136. (In Russ.)
7. Garnov SV, Abramov DV, Bukharov DN, Khudaiberganov TA, et al. Electrophysics of carbon 1d structures obtained in a laser experiment: models and demonstration. *Uspekhi Fizicheskih Nauk = Physics-Uspekhi*. 2024;194(2):115-137. DOI:10.3367/UFNr.2023.12.039620 (In Russ.)
8. Bukharov DN, Tumarkina DD, Kucherik AO, Tkachev AG, et al. Structure control of metal-carbon composites with different nanotopological configurations and electrical conductivity characteristics in a laser experiment. *Journal of Advanced Materials and Technologies*. 2024;9(3):207-235. DOI:10.17277/jamt.2024.03.pp.207-235
9. Bukharov DN, Kucherik AO, Arakelian SM. Nanocluster fractal electrical conductivity in thin films on a solid surface: dimensional model of different configurations and demonstration of results in a laser experiment. *Journal of Advanced Materials and Technologies*. 2023;8(3):227-251. DOI:10.17277/jamt.2023.03.pp.227-251
10. Trakhtenberg LI, Mel′nikova MYa. *Metal/semiconductor containing nanocomposites*. Moscow: Technosphere; 2019. 624 p. (In Russ.)
11. Arakelyan SM, Kucherik AO, Prokoshev VG, Rau VG, Sergeyev AG. *Introduction to femtonanophotonics: fundamental principles and laser methods for the controlled production and diagnosis of nanostructured materials: a textbook*. Moscow: Logos; 2020. 744 p. (In Russ.)
12. *Practical recommendations for the development of printed circuit boards*. Available from: https://btpit36.ru/pluginfile.php/5733/mod_resource/content/2/samspcbguide_ce_1.1.pdf [Accessed 21 June 2025]
13. Shumilin AV, Bel′tyukov YaM. The effect of nonequilibrium correlations on the effective resistance between centers in the theory of hopping conduction. *Fizikat verdogo tela = Physics of the Solid State*. 2019; 61(11):2116-2121. DOI:10.21883/FTT.2019.11.48416.509 (In Russ.)
14. Kuvayskova YuE. *Algorithms of discrete mathematics: a textbook*. Ulyanovsk: UlGTU Publ. House; 2017. 99 p. ISBN 978-5-9795-1635-6 (In Russ.)
15. Korchagin SA, Terin DV, Klinayev YuV. Modeling of a fractal composite and investigation of its electrical characteristics. *Matematicheskoye modelirovaniye i chislennyye metody*. 2017;13(1):22-31. (In Russ.)
16. Bonch-Bruyevich VL. Problems of the electron theory of disordered semiconductors. *Uspekhi fizicheskikh nauk = Physics-Uspekhi*. 1983;140(4):583-637. DOI: 10.3367/UFNr.0140.198308b.0583 (In Russ.)
17. Cao M, Chen J, Sun X, Xie F, Li B. Theoretical predictions and experimental verifications of SERS detection in colorants. *RSC Advances*. 2023;13(22):15086-15098. DOI: 10.1039/D3RA01584J

18. *Detecting and identifying food colorants with SERS. Spectroscopy online*. Available from: https://www.spectroscopyonline.com/view/detecting-and-identifying-food-colorants-sers [Accessed 21 June 2025]

19. Tkachenko LA, Repina AV. *The theory of unsteady heat transfer: A textbook*. Kazan: Kazan University Publ. House; 2017. 139 p. (In Russ.)

20. Rykalin NN, Uglov AA, Zuyev IV, Kokora AN. *Laser electron beam processing of materials: A reference book*. Moscow: Mashinostroyeniye; 1985. 496 p. (In Russ.)

21. Libenson MN, Yakovlev EB, Shandybina GD. *Interaction of laser radiation with matter (power optics). Part II. Laser heating and destruction of materials. Study guide*. Saint-Petersburg: ITMO Publ. House; 2014. 181 p. (In Russ.)

22. Antonov DN, Burtsev AA, Butkovskiy OYa. Distribution of dendrites produced on the surface of steel as a result of exposure to laser radiation. *Zhurnal tekhnicheskoy fiziki = Technical Physics*. 2016;86(1):110-115. (In Russ.)

23. Unutulmazsoy Y, Merkle R, Fischer D, Mannhart J, Maie, J. The oxidation kinetics of thin nickel films between 250 and 500 °C. *Physical Chemistry Chemical Physics*. 2017;19(13):9045-9052. DOI:10.1039/C7CP00476A

24. Vorobev AH. *Diffusion problems in chemical kinetics. Study guide*. Moscow: Lomonosov MSU Publ. House; 2003. 98 p. (In Russ.)

25. AISI 304 *Stainless steel characteristics*. Available from: https://inoxtrade.ru/info/commoninfo/item100590/aisi-304/ [Accessed 21 June 2025]

26. *Special functions*. Available from: https://www.tutorialspoint.com/python/special_functions.htm [Accessed 21 June 2025]

27. Sergeyev NA, Ryabushkin DS. *Physics of nanosystems: monograph*. Moscow: Logos; 2016. 192 p. (In Russ.)

28. Borlakov KhSh, Kochkarova PA. Fractal dimension as a thermodynamic parameter. *Izvestiya vuzov. Severo-Kavkazskiy region. Yestestvennyye nauki*. 2006;3:50-52. (In Russ.)

29. Aleshin MP, Tumarkina DD, Oparin ES, Bukharov DN, et al. Models and structures in the electrophysics of high-entropy alloys with laser-induced fractal surface objects. *Physics of Metals and Metallography*. 2024;125(9):970-985. DOI:10.1134/S0031918X24601574

30. Suzdalev IP. *Nanotechnology: Physico-chemistry of nanoclusters, nanostructures and nanomaterials*. Moscow: LIBROKOM Publ. House; 2019. 592 p. (In Russ.)

31. Tumarkina DD, Butkovskiy OY, Bolachkov AV, Burtsev AA. Surface topology of mixing entropy resulting from two-pulse laser ablation of stainless steel. *Fiziko-khimicheskie aspekty izucheniya klasterov, nanostruktur i nanomaterialov*. 2023;15:869-878. DOI:10.26456/pcascnn/2023.15.869 (In Russ.)

32. Rekhviashvili SH, Kishtikova EV. On the melting temperature of nanoparticles and nanostructured substances. *Pis'ma v zhurnal tekhnicheskoy fiziki = Technical Physics Letters*. 2006;32(10):50-55. (In Russ.)

33. *Atomic radii*. Available from: https://dpva.ru/Guide/GuidePhysics/Length/AtomicRadius [Accessed 21 June 2025]

34. Spivak LV, Shchepina NE. Polymorphic transformations in iron and zirconium. *Technical Physics*. 2020;65:1100-1105. DOI:10.1134/S1063784220070221

35. Pochtenny AE. *Jump conductivity under direct current in intrinsic and doped organic semiconductors: monograph*. Minsk: BGTU Publ. House; 2016. 171 p. (In Russ.)

36. Blinova NA, Filippov MV. Method of finding a path in a labyrinth in the presence of interference. *Novyye informatsionnyye tekhnologii v avtomatizirovannykh sistemakh*. 2019;22:46-50. (In Russ.)

37. Krevchik VD, Semenov MB, Krevchik PV. Quantum tunneling with dissipation: an application to tunnel transport for semiconductor quantum dots in a combined AFM / STM system under external electric field conditions (review). Part II. *Izvestiya vysshikh uchebnykh zavedeniy. Povolzhskiy region. Fiziko-matematicheskie nauki*. 2020;(4):132-185. DOI:10.21685/2072-3040-2020-4-9 (In Russ.)

38. Simonyan ES, Medvedeva OA, Medvedev SN. Creation of maze with multiple solutions, search for all solutions and editing them. *Modelirovaniye, optimizatsiya i informatsionnyye tekhnologii*. 2019;7(2(25)):365-381. DOI:10.26102/2310-6018/2019.25.2.030 (In Russ.)

39. Krasnov ES. Methodology for evaluating path-finding algorithms in a maze to select a mobile robot movement strategy. *Izvestiya Tul'skogo gosudarstvennogo universiteta. Tekhnicheskiye nauki*. 2012;11(2):179-187. (In Russ.)

40. Moskalev PV. Analysis of the structure of a percolation cluster. *Zhurnal tehnicheskoy fiziki = Technical Physics*. 2009;79(6):1-7. (In Russ.)

41. Moshnikov V.A., Nalimova S.S., Seleznev B.I. Gas-sensitive layers based on fractal-percolation structures. *Semiconductors*. 2014;48(11):1499-1503. DOI:10.1134/S1063782614110177

42. Montaldi J, Smolyanov OG. Feynman path integrals and Lebesgue–Feynman measures. *Doklady Mathematics*. 2017;96(1):368-372. DOI:10.1134/S1064562417040226

43. Tsitsiashvili GSh, Osipova MA, Losev AS. Derivation of asymptotic constants for the disconnection probability of a planar weighted graph. *Prikladnaya diskretnaya matematika*. 2014;2:97-100. (In Russ.)

44. Kuznetsov VM, Khromov VI. Fractal representation of the Debye theory for studying the heat capacity of macro-and nanostructures. *Technical Physics*. 2008; 53(11):1401-1406. DOI:10.1134/S1063784208110029

45. Goryachev NS, Kukushkin VI, Belik AY, Rybkin AY, et al. Using SERS and SEF spectroscopy to detect fullerene-dye dyads in water and biological structures. *Bulletin of the Russian Academy of Sciences: Physics*. 2022;86(4):418-422. DOI:10.3103/S1062873822040116

Information about the authors / Информация об авторах

Darya D. Tumarkina, Teaching Assistant, Vladimir State University (VlSU), Vladimir, Russian Federation; ORCID 0009-0007-5496-4234; e-mail: tumarkina.darya@mail.ru

Oleg Ya. Butkovsky, D. Sc. (Phys. and Math.), Professor, VlSU, Vladimir, Russian Federation; ORCID 0000-0001-6052-666X; e-mail: OYButkovskiy@fa.ru

Dmitry N. Bukharov, Cand. Sc. (Phys. and Math.), Associate Professor, VlSU, Vladimir, Russian Federation; ORCID 0000-0002-4536-8576; e-mail: buharovdn@gmail.com

Irina V. Burakova, Cand. Sc. (Eng.), Associate Professor, Tambov State Technical University (TSTU), Tambov, Russian Federation; ORCID 0000-0003-0850-9365; e-mail: iris_tamb68@mail.ru

Alexander E. Burakov, Cand. Sc. (Eng.), Associate Professor, Acting Head of the Department, TSTU, Tambov, Russian Federation; ORCID 0000-0003-4871-3504; e-mail: m-alex1983@yandex.ru

Sergey M. Arakelian, D. Sc. (Phys. and Math.), Professor, Independent Researcher, Vladimir, Russian Federation; ORCID 0000-0002-6323-7123; e-mail: arak@vlsu.ru

Тумаркина Дарья Денисовна, ассистент, Владимирский государственный университет имени А. Г. и Н. Г. Столетовых (ВлГУ), Владимир, Российская Федерация; ORCID 0009-0007-5496-4234; e-mail: tumarkina.darya@mail.ru

Бутковский Олег Ярославович, доктор физико-математических наук, профессор, ВлГУ, Владимир, Российская Федерация; ORCID 0000-0001-6052-666X; e-mail: OYButkovskiy@fa.ru

Бухаров Дмитрий Николаевич, кандидат физико-математических наук, доцент, ВлГУ, Владимир, Российская Федерация; ORCID 0000-0002-4536-8576; e-mail: buharovdn@gmail.com

Буракова Ирина Владимировна, кандидат технических наук, доцент, Тамбовский государственный технический университет (ТГТУ), Тамбов, Российская Федерация; ORCID 0000-0003-0850-9365; e-mail: iris_tamb68@mail.ru

Бураков Александр Евгеньевич, кандидат технических наук, доцент, и. о. заведующего кафедрой, ТГТУ, Тамбов, Российская Федерация; ORCID 0000-0003-4871-3504; e-mail: m-alex1983@yandex.ru

Аракелян Сергей Мартиросович, доктор физико-математических наук, профессор, независимый исследователь, Владимир, Российская Федерация; ORCID 0000-0002-6323-7123; e-mail: arak@vlsu.ru

Received 21 August 2025; Revised 04 October 2025; Accepted 10 October 2025

Original papers
Materials for energy and environment, next-generation photovoltaics, and green technologies

УДК 661.965+544.723.2 DOI: 10.17277/jamt-2025-10-04-342-350

Hydrogen separation from gas mixtures: evaluation of adsorbent performance using the IAST model

© Nikita S. Krysanov[a], Elena A. Berdonosova[a], Semen N. Klyamkin[a]✉

[a] *Lomonosov Moscow State University, 1/3, Leninskie Gory, Moscow, 119991, Russian Federation*

✉ klyamkin@highp.chem.msu.ru

Abstract: Samples of commercial adsorbents – activated carbon (AC), zeolite (ZS), and silica gel (SG) – were studied in the adsorption processes of hydrogen, methane, nitrogen, carbon dioxide, and carbon monoxide in order to assess their efficiency for hydrogen purification from gas impurities. The composition and morphology of the materials were characterized using scanning electron microscopy and energy-dispersive X-ray microanalysis. Textural properties (specific surface area and pore structure) were determined from nitrogen cryosorption data using the BET, Gurvich, and BJH models. Adsorption isotherms were obtained for all studied gases at pressures up to 25 atm and temperatures ranging from 0 to 50 °C. Isosteric heats of adsorption and ideal selectivities for the "impurity gas – hydrogen" pairs were calculated. To evaluate the behavior of the studied adsorbents toward multicomponent gas mixtures, simulations were performed using the Ideal Adsorbed Solution Theory (IAST). This approach revealed that in real mixtures, the selectivity $S_{IAST}(CO_2/H_2)$ increases by a factor of 1.5–3 compared to the values estimated from single-gas data.

Keywords: hydrogen; pressure swing adsorption; adsorbents; Ideal Adsorbed Solution Theory (IAST).

For citation: Krysanov NS, Berdonosova EA, Klyamkin SN. Hydrogen separation from gas mixtures: evaluation of adsorbent performance using the IAST model. *Journal of Advanced Materials and Technologies*. 2025;10(4):342-350. DOI: 10.17277/jamt-2025-10-04-342-350

Выделение водорода из газовых смесей: оценка эффективности адсорбентов с применением модели IAST

© Н. С. Крысанов[a], Е. А. Бердоносова[a], С. Н. Клямкин[a]✉

[a] *Московский государственный университет имени М. В. Ломоносова, Ленинские горы, 1/3, Москва, 119991, Российская Федерация*

✉ klyamkin@highp.chem.msu.ru

Аннотация: Образцы коммерческих адсорбентов активированного угля AC, цеолита ZS и силикагеля SG были исследованы в процессах адсорбции водорода, метана, азота, углекислого и угарного газа для оценки эффективности их использования при очистке водорода от газовых примесей. Методами сканирующей электронной микроскопии и энергодисперсионного микроанализа охарактеризованы состав и морфология материалов. Текстурные характеристики (удельная поверхность и характер пористости) рассчитаны по моделям БЭТ, Гурвича и BJH на основе данных по криосорбции азота. Для всех изученных газов построены изотермы адсорбции в области давлений до 25 атм при температурах от 0 до 50 °C, определены изостерические теплоты адсорбции, рассчитаны идеальные селективности в парах «примесный газ – водород». Для оценки поведения изученных адсорбентов по отношению к многокомпонентным газовым смесям проведено моделирования с использованием теории идеальных адсорбированных растворов (IAST). Данный подход позволил установить, что в реальных смесях селективность $S_{IAST}(CO_2/H_2)$ увеличивается в 1,5–3 раза по сравнению с расчетами по данным для индивидуальных газов.

Ключевые слова: водород; короткоцикловая адсорбция; адсорбенты; теория идеальных адсорбированных растворов (IAST).

Для цитирования: Krysanov NS, Berdonosova EA, Klyamkin SN. Hydrogen separation from gas mixtures: evaluation of adsorbent performance using the IAST model. *Journal of Advanced Materials and Technologies*. 2025;10(4):342-350. DOI: 10.17277/jamt-2025-10-04-342-350

1. Introduction

At present, the main method for producing hydrogen is its extraction from the products of natural gas steam reforming or purification of by-product gases from oil refineries [1, 2]. Three primary methods are currently used for separating hydrogen-containing gas mixtures: partial condensation, pressure swing adsorption (PSA), and membrane gas separation [3].

Hydrogen purification is most commonly carried out by pressure swing adsorption (PSA)**,** which is based on the preferential adsorption of impurities when a gas mixture is passed under high pressure through an adsorbent bed, followed by desorption upon pressure reduction [4, 5]. Activated carbons, zeolites, and silica gels are typically used as adsorbents in PSA systems [6, 7].

Activated carbon is a highly porous carbon material obtained from various precursors such as coal, petroleum, or plant-based sources. Different activation methods yield carbons with a wide range of pore volumes, structures, and surface chemical compositions. The average pore size varies from 35 Å to 2050 Å. For example, BPL-grade activated carbon has a surface area of 1100 $m^2 \cdot g^{-1}$ and a pore volume of 0.7 $cm^3 \cdot g^{-1}$, making it suitable for hydrogen purification by PSA [8].

Zeolites are aluminosilicates with a three-dimensional framework of $[XO_4]$ tetrahedra, where X = Al or Si. They are classified according to their Si/Al ratio: type A zeolites (Si/Al ~ 1.0), type X (Si/Al ~ 1.0–1.5), and type Y (Si/Al ~ 1.5–3.0). In industry, calcium-exchanged zeolite 5A – with a pore size of 5 Å and a surface area of 460–480 $m^2 \cdot g^{-1}$ is commonly used for hydrogen purification [9–11].

Silica gel is a porous amorphous form of silicon dioxide with an interconnected pore network. Depending on the synthesis method, it can have micropores (S_{sp} ~ 700–800 $m^2 \cdot g^{-1}$), mesopores (S_{sp} ~ 520 $m^2 \cdot g^{-1}$), or macropores (S_{sp} ~ 320 $m^2 \cdot g^{-1}$). The Sorbead® H grade of silica gel, containing 3–4 % aluminum oxide, has a surface area of 750 $m^2 \cdot g^{-1}$ and a pore volume of 0.5 $cm^3 \cdot g^{-1}$, making it an effective adsorbent for hydrogen purification [12, 13].

The evaluation of hydrogen purification efficiency on each adsorbent was performed using simulations based on the Ideal Adsorbed Solution Theory (IAST). The IAST assumes that adsorbed molecules form an ideal solution on the adsorbent surface. In this model, the adsorbent is considered thermodynamically inert with a constant surface area, and adsorption is described through the Gibbs approach [14]. It has been shown that IAST-based modeling provides results more rapidly than grand canonical Monte Carlo simulations [15]. For the calculations, a specialized Python-based program under the MIT license (pyIAST) was used [16].

The aim of this work is to characterize the adsorbents AC, SG, and ZS, and to evaluate their performance in hydrogen separation from gas mixtures using the IAST model.

2. Materials and Methods

2.1. Initial materials

For characterization, specific samples of commercial adsorbents provided by the scientific and industrial company Grasys (Moscow) were selected for testing: activated carbon AC, silica gel SG, and zeolite ZS. These materials are considered potential alternatives to the adsorbents currently used in industrial PSA units.

2.2. Research methods

The morphology of the materials was examined using a TESCAN Vega3 XM scanning electron microscope (SEM) at an accelerating voltage of 10 kV. Both secondary and backscattered electron detectors were employed, and the sample surfaces were gold-coated to ensure electrical conductivity. Elemental composition was determined using an Oxford Instruments INCA X-act energy-dispersive (EDX) microanalyzer.

X-ray diffraction (XRD) data were collected at room temperature using a Thermo ARL X'TRA powder diffractometer with CuKα radiation (λ = 1.5405 Å). Measurements were performed in reflection geometry using a semiconductor Peltier detector, over a 2θ range of 5° to 65° with a scanning rate of 0.5°·min^{-1}.

The porous structure of the samples was investigated by nitrogen cryosorption at –196 °C using an IMC Prosurf-v1220 instrument. Prior to measurements, the samples were degassed under vacuum ($5.0 \cdot 10^{-3}$ mmHg) and activated at different temperatures: 200 °C for activated carbon, 130 °C for silica gel, and 150 °C for zeolite. The specific surface area was calculated using the BET model in the relative pressure range of (0.05–0.35)p/p_0, while the total pore volume was determined by the Gurvich method at 0.97 p/p_0. The pore size distribution was derived using the BJH method.

Excess gas adsorption on the sorbent surface was measured by the volumetric (Sieverts) method. Adsorbent granules (3–5 g) were placed in an

autoclave, which was degassed to $5.0 \cdot 10^{-3}$ mmHg and activated at specific temperatures. After cooling, the autoclave was placed in a thermostat to achieve thermal equilibrium. Temperature control was maintained using an ice bath and a high-precision water thermostat, with temperature stability of ±0.2, ±0.3, and ±0.1 °C depending on the experiment.

The autoclave volume was calibrated using helium. For measurements conducted at non-room temperatures, the volumes of the apparatus parts held at different temperatures were accounted for. The amount of adsorbed gas was determined from manometric measurements by calculating the difference between the introduced gas mass m_0 and the residual mass m_1. The difference between the masses m_0 and m_1 yielded the mass of the adsorbed gas Δm. Gas densities were obtained from the Thermophysical Properties of Fluid Systems database [17].

Uncertainties in pressure and temperature measurements resulted in adsorption errors of ±0.032 mmol·g^{-1} for CO_2, CO, CH_4 и N_2 and ±0.017 mmol·g^{-1} for H_2 at 25 atm.

To describe the excess adsorption isotherms, high-degree polynomial fits were applied using OriginPro software, with a coefficient of determination $R^2 > 0.9998$**.** The isosteric heat of adsorption for CH_4, CO_2, N_2, CO и H_2 was determined from the slope of the isosteres, which relate the logarithm of equilibrium gas pressure to the reciprocal of temperature at constant adsorption. The uncertainty in the isosteric heat Q_{isost} was estimated using the least squares method**.** Measurements were conducted for the adsorption of each of the five gases at three temperatures: 0, 22, and 50 °C.

3. Results and Discussion

To determine the chemical composition and surface morphology, the adsorbent samples were analyzed using energy-dispersive X-ray spectroscopy and SEM.

The high oxygen content in the activated carbon AC (8 wt. %) indicates the presence of oxygen-containing functional groups. The silica gel SG showed a lower oxygen content (42 wt. %) and an elevated carbon content (11 wt. %), which may be attributed to surface contamination during synthesis. The chemical composition of the zeolite ZS corresponds to that of calcium zeolite A (Si:Al ~ 1.0).

Figure 1 presents SEM-images of the adsorbent particle surfaces at both low and high magnifications.

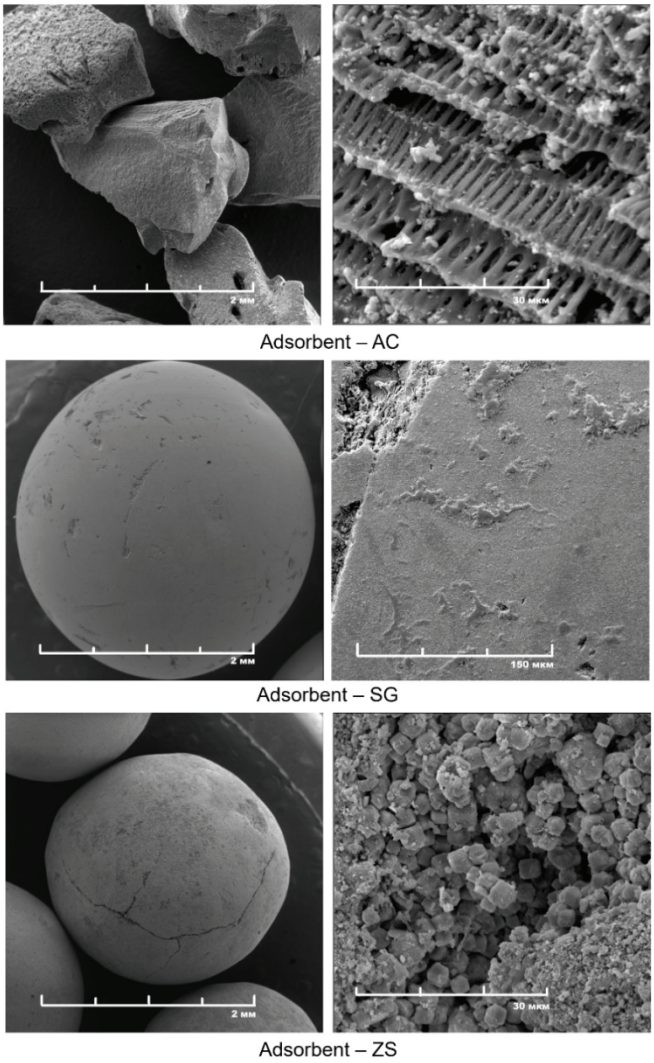

Fig. 1. SEM-images of the adsorbent surfaces

The activated carbon granules have sizes of approximately 1.5–2.0 mm, featuring an irregular surface and layered structure. In contrast, the silica gel SG and zeolite ZS granules exhibit a rounded shape with diameters of about 2.5–3.0 mm; their surfaces also display defects, chips, and cracks.

The classification of the adsorbents as crystalline or amorphous materials was performed using X-ray diffraction (XRD) analysis.

The XRD pattern of the activated carbon shows two broad peaks at 23° and 43°, corresponding to the (002) and (100) reflections of graphite. The average widths of these peaks were used to calculate the crystallite dimensions along the basal plane L_a and perpendicular to it L_c using the Scherrer equation [18].

The obtained values, $L_a = 3.51$ nm and $L_c = 1.02$ nm, indicate the presence of nanosized graphite crystallites within the activated carbon.

Table 1. Adsorption characteristics of the studied sorbents

Adsorbent	Activated carbon AC	Silica Gel SG	Zeolite ZS
S_{sp}, $m^2 \cdot g^{-1}$	994	741	408
V_{pore}, $cm^3 \cdot g^{-1}$	0.44	0.40	0.25
Fraction, %:			
micropore	92	79	88
mesopore	7	20	9
macropore	1	1	3

The XRD pattern of the zeolite ZS exhibits a series of narrow, intense peaks, confirming its crystalline nature. Analysis of the diffraction data showed that zeolite ZS crystallizes in a cubic unit cell (space group $Fm\bar{3}m$) with a lattice parameter of $a = (2.34 \pm 0.02)$ Å, consistent with calcium zeolite 5A ($Fm\bar{3}m$, $a = 12.32$ Å) [19].

The specific surface area (S_{sp}, $m^2 \cdot g^{-1}$) of the adsorbents was measured by nitrogen cryosorption and processed using the BET theory. The total pore volume (V_{pore}, $cm^3 \cdot g^{-1}$) and pore size distribution were determined from the BET isotherms using the Gurvich and BJH methods, respectively. The adsorption characteristics calculated from the isotherm data are presented in Table 1.

The obtained values of specific surface area and pore volume are consistent with literature data for similar adsorbents [20]. The activated carbon AC exhibits the largest surface area and porosity, whereas the zeolite ZS shows the smallest values of S_{sp} and V_{pore}. A high proportion of micropores is an important criterion for the effective use of a material as an adsorbent.

All three sorbents – activated carbon AC, silica gel SG, and zeolite ZS – are characterized by predominantly microporous structures. The activated carbon AC possesses the highest fraction of micropores, while the silica gel SG has the lowest.

Excess gas adsorption measurements were carried out at three different temperatures: 0, 22, and 50 °C. The adsorbates selected for the study were H_2 and its most common impurities – CO_2, CO, N_2 and CH_4. The excess adsorption isotherms of these gases on the sorbents at room temperature (22 °C) are shown in Fig. 2.

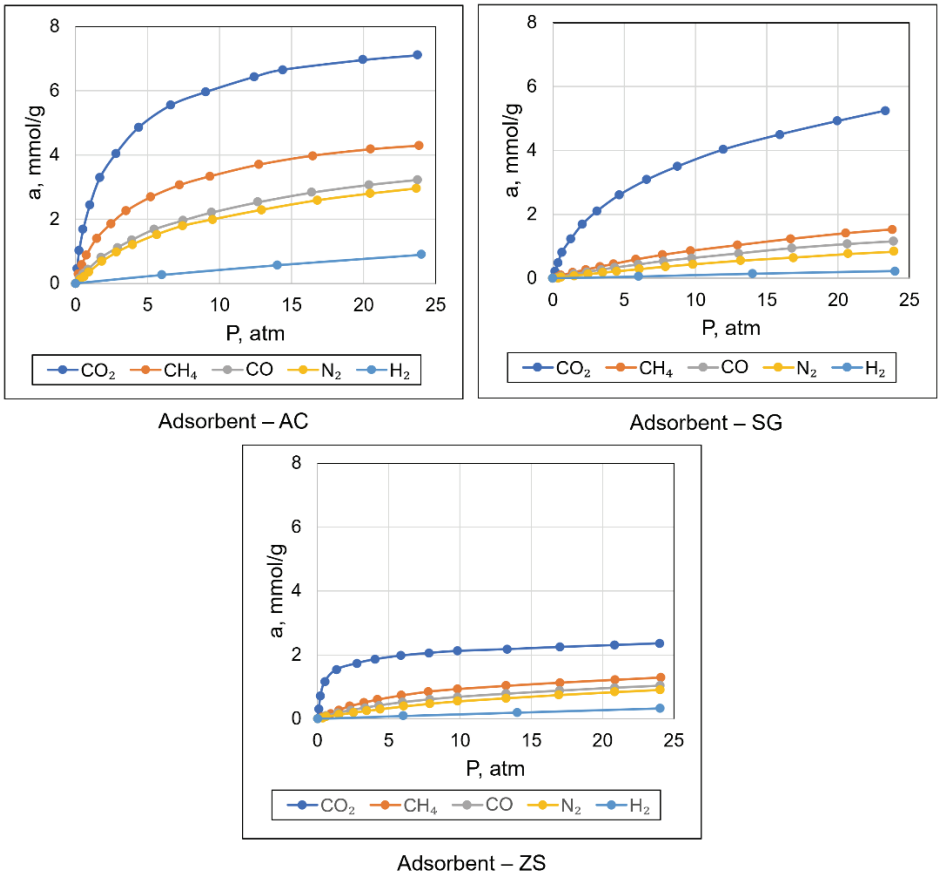

Fig. 2. Isotherms of excess gas adsorption on adsorbents at 22 °C

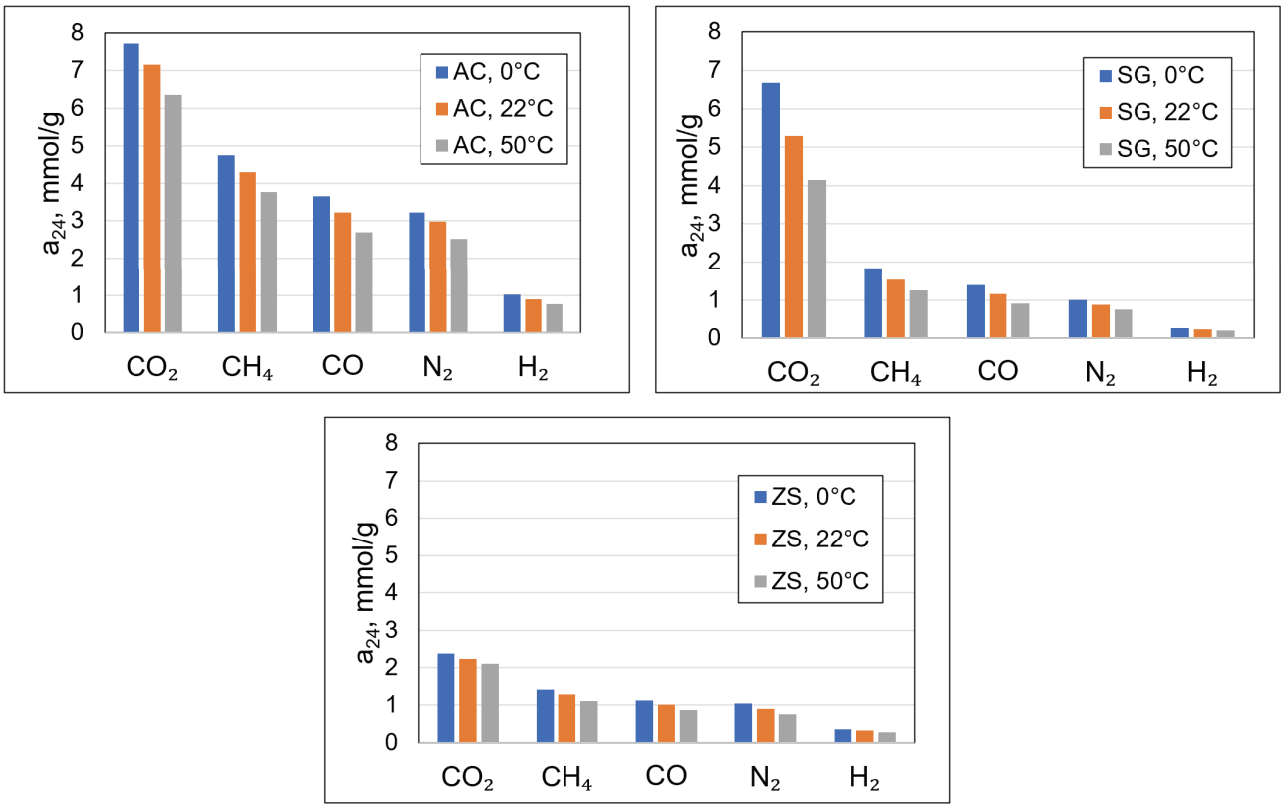

Fig. 3. Values of excess gas adsorption a_{24} at pressure P = 24 atm

For each of the three sorbents, the adsorption isotherms of methane (CH_4), carbon dioxide (CO_2), nitrogen (N_2), and carbon monoxide (CO) correspond to Type I isotherms according to the Brunauer classification [21]. The linear region of these isotherms lies within the pressure range up to 1–2 atm. The hydrogen adsorption isotherms on all sorbents are nearly linear and are well described by Henry's law.

For each gas adsorbent pair, the values of excess adsorption at the maximum pressure of 24 atm were determined and are presented in Fig. 3 on the same scale. The a_{24} values for a given gas/adsorbent pair decrease with increasing temperature, indicating the exothermic nature of the adsorption process.

The adsorption capacities of the gases for each adsorbent decrease in the following order: $CO_2 >> CH_4 > CO > N_2 >> H_2$, which is consistent with literature data for activated carbons [1] and silica gels [22]. For strongly polar zeolites, however, the adsorption sequence commonly reported in the literature is $CO_2 >> CO > CH_4 > N_2 >> H_2$ [1]. The deviation observed for the zeolite ZS may be attributed to a low number of adsorption sites for the polar CO and the highly polarizable CO_2 molecules with large quadrupole moments.

The calculated isosteric heats of adsorption in the temperature range 0 to 50 °C for CH_4, CO_2, CO, N_2, and H_2 are presented in Table 2.

Table 2. Values of isosteric heats of adsorption Q_{isost} for the studied gases

Gas	Adsorbent	Q_{isost}, kJ·mol^{-1}
CH_4	AC	15.5–17.5
	SG	15.3–16.9
	ZS	14.2–17.2
CO_2	AC	20.2–23.2
	SG	18.3–20.4
	ZS	13.5–25.5
N_2	AC	10.9–13.7
	SG	7.1–11.9
	ZS	9.0–12.6
CO	AC	13.8–16.1
	SG	11.3–15.7
	ZS	10.2–15.2
H_2	AC	4.1–6.3
	SG	3.8–5.2
	ZS	3.8–5.8

Based on the obtained adsorption isotherms for each impurity gas (CH_4, CO_2, N_2, and CO), the ideal selectivity coefficients relative to hydrogen were calculated as follows:

$$S_{\text{id}}(\text{X/H}_2) = \frac{a(\text{X})_{P,T}}{a(\text{H}_2)_{P,T}}, \quad (1)$$

where $a(\text{X})_{P,T}$ and $a(\text{H}_2)_{P,T}$ are the excess adsorptions of gas X and hydrogen H_2 on a given adsorbent at temperature *T* and pressure *P*.

The values of the ideal selectivity coefficients for each gas on activated carbon AC correlate well with literature data for BPL carbon. However, for zeolite ZS, the selectivities for CH_4/H_2 and N_2/H_2 pairs were found to be four times lower than those for commercial zeolite 5A; for CO/H_2, almost 16 times lower; and for CO_2/H_2, about two orders of magnitude lower than reported values. This reduction is attributed to a limited number of available adsorption sites capable of binding impurity gases on the adsorbent surface [1]. It is possible that the studied sorbents require more rigorous activation conditions than those recommended by the manufacturer and used in this work.

For the ideal selectivity coefficients $S_{\text{id}}(\text{X/H}_2)$, a decrease with increasing pressure *P* was observed, indicating higher gas separation efficiency at lower pressures. This behavior is due to the different shapes of the excess adsorption isotherms for impurity gases (Type I, according to Brunauer's classification) and for hydrogen (linear isotherm).

At low pressures, the ideal selectivity relative to hydrogen increases with decreasing temperature**.** This is associated with the higher heat of adsorption of impurity gases compared to hydrogen, leading to a greater increase in excess adsorption of the impurity gas under identical pressure conditions.

The ideal selectivity coefficients $S_{\text{id}}(\text{X/H}_2)$ account only for gas adsorption at equal partial pressures on pure adsorbents. Therefore, to model gas behavior in real multicomponent mixtures**,** other approaches must be applied–such as calculations using the IAST.

The IAST allows for the calculation of the excess adsorption of each gas component in a mixture based on their partial pressures in the gas phase and the adsorption isotherms of the pure gases.

The IAST selectivity coefficient for gas separation was calculated using the following equation, which accounts for the gas composition in the mixture:

$$S_{\text{IAST}}(\text{X/H}_2) = \frac{a_{\text{IAST}}(\text{X})\,\varphi(\text{H}_2)}{a_{\text{IAST}}(\text{H}_2)\,\varphi(\text{X})}, \quad (2)$$

where $\varphi(\text{X})$ and $\varphi(\text{H}_2)$ are the volume fractions of gas X and hydrogen in the gas mixture being separated, and $a_{\text{IAST}}(\text{X})$ and $a_{\text{IAST}}(\text{H}_2)$ are the real adsorption values obtained from the IAST model calculations.

The active adsorption sites on the surface are initially occupied by the most strongly adsorbed component (CO_2), followed by gases in the order $CH_4 > CO > H_2$. The competition for adsorption sites is also influenced by the composition of the equilibrium gas mixture above the adsorbent.

At present, the key method for hydrogen production is its purification using adsorption-based techniques from the products of natural gas steam reforming. The gas mixture (mixture 1) obtained after cooling of the reaction stream has the following composition: 70–80 % H_2, 15–25 % CO_2, 3–6 % CH_4, 1–3 % CO, and small amounts of N_2 impurities.

To perform a preliminary selection of the adsorbent and determine the optimal conditions for hydrogen purification from impurities in *gas mixture 1*, IAST modeling was applied to a *model gas mixture* with the following composition: 73.5 % H_2, 20 % CO_2, 4.5 % CH_4, and 2.0 % CO. This composition corresponds to the average impurity content of CO_2, CH_4, and CO in the real gas *mixture 1* subjected to purification.

Below is a comparison of the ideal selectivity coefficients with the IAST separation selectivity coefficient**s** in the Henry's law region (Table 3) and at a pressure of 20 atm (Table 4).

For each sorbent in the Henry's law region ($P < 1$ atm), the selectivity coefficient according to IAST for the CO_2/H_2 pair, $S_{\text{IAST}}(CO_2/H_2)$, is higher than the ideal selectivity $S_{\text{id}}(CO_2/H_2)$ at 0, 22, and 50°C. This is due to the preferential adsorption of carbon dioxide, which has the greatest affinity for the sorbent. The largest difference between $S_{\text{IAST}}(CO_2/H_2)$ and $S_{\text{id}}(CO_2/H_2)$ is observed for zeolite ZS, which effectively adsorbs carbon dioxide in the low-pressure region. This is reflected in the shape of the corresponding excess adsorption isotherm.

For CH_4 and CO, the values of $S_{\text{IAST}}(\text{X/H}_2)$ are comparable to $S_{\text{id}}(\text{X/H}_2)$. Recalculation using the IAST model has almost no effect on selectivity, since the adsorption values of CO, CH_4, and H_2 decrease to a similar extent due to competition with the more strongly adsorbed CO_2.

Table 3. Comparison of ideal selectivity coefficients S_{id} and IAST selectivity coefficients S_{IAST} in the Henry's law region

Adsorbent	Gas	0 °C		22 °C		50 °C	
		$S_{id}(X/H_2)$	$S_{IAST}(X/H_2)$	$S_{id}(X/H_2)$	$S_{IAST}(X/H_2)$	$S_{id}(X/H_2)$	$S_{IAST}(X/H_2)$
AC	CO_2	90.0	113.4	72.8	83.2	54.8	62.5
	CH_4	38.3	36.9	32.2	30.5	32.2	21.4
	CO	20.0	17.0	15.1	12.9	11.9	9.4
SG	CO_2	104.3	157.2	99.9	125.7	93.2	103.0
	CH_4	12.8	14.6	12.3	13.5	11.8	12.6
	CO	10.7	12.4	9.3	10.1	8.0	8.8
ZS	CO_2	80.1	216.1	75.1	188.7	69.9	127.3
	CH_4	15.3	20.2	12.4	13.9	9.5	9.7
	CO	8.4	10.1	8.0	9.2	7.7	8.0

Table 4. Comparison of ideal selectivity coefficients S_{id} and selectivity coefficients according to IAST S_{IAST} at 20 atm

Adsorbent	Gas	0 °C		22 °C		50 °C	
		$S_{id}(X/H_2)$	$S_{IAST}(X/H_2)$	$S_{id}(X/H_2)$	$S_{IAST}(X/H_2)$	$S_{id}(X/H_2)$	$S_{IAST}(X/H_2)$
AC	CO_2	8.9	57.3	8.7	46.8	8.5	32.9
	CH_4	5.4	11.8	5.3	11.4	5.1	11.3
	CO	4.0	5.0	3.9	4.8	3.8	4.7
SG	CO_2	28.9	105.4	25.3	84.2	22.2	61.8
	CH_4	7.7	7.6	7.1	7.4	6.5	7.1
	CO	5.9	4.6	5.4	4.4	4.7	4.2
ZS	CO_2	8.3	70.7	7.9	65.8	7.6	54.0
	CH_4	4.4	4.6	4.3	4.4	4.2	4.3
	CO	3.5	4.2	3.4	3.6	3.2	3.1

For the gas separation selectivity coefficients calculated by IAST, $S_{IAST}(X/H_2)$ in the Henry's law region – as across the entire pressure range – a decrease in selectivity is observed with increasing temperature. Therefore, lowering the process temperature can enhance the efficiency of gas mixture separation.

As with the ideal selectivity coefficients $S_{id}(X/H_2)$, the IAST selectivity coefficients $S_{IAST}(X/H_2)$ also decrease with increasing total mixture pressure (Table 4), indicating that gas separation is more effective in the low-pressure region. However, separation at low pressures is practically impossible in the case of pressure swing adsorption (PSA) processes, since desorption typically occurs in the low-pressure range, while adsorption takes place at higher pressures – from 8 to 28 atm.

Depending on the total gas mixture pressure and experimental temperature, the most effective sorbent for CO_2 removal can be either zeolite ZS ($P < 12$ atm at 22 °C) or silica gel SG ($P > 12$ atm at 22 °C). Activated carbon AC can be used for the most effective removal of CO and CH_4 impurities from gas mixtures.

Thus, from the standpoint of real gas separation selectivity calculated using IAST theory, hydrogen purification from impurities is most effective at the lowest possible temperature and under low-pressure conditions. Under these conditions, zeolite ZS is the

most efficient for removing CO_2 impurities, while activated carbon AC is most effective for removing CH_4 and CO. For gas mixture separation at higher pressures (above 12 atm, which is closer to real operating conditions), silica gel SG is preferable for CO_2 removal, and activated carbon AC remains the best option for CH_4 and CO removal.

4. Conclusion

The surface morphology and structure of commercial adsorbents – activated carbon AC, silica gel SG, and zeolite ZS – have been studied. All of these materials belong to the class of microporous materials, with a micropore fraction ranging from 79 to 92 %. The highest specific surface area ($S_{sp} = 994$ $m^2 \cdot g^{-1}$) and pore volume ($V_{pore} = = 0.44$ $cm^3 \cdot g^{-1}$) are observed for AC, while the lowest values are found for ZS ($S_{sp} = 408$ $m^2 \cdot g^{-1}$, $V_{pore} = 0.25$ $cm^3 \cdot g^{-1}$). Excess adsorption isotherms for hydrogen and impurity gases (CO_2, CH_4, CO, N_2) were measured at temperatures from 0 to 50 °C and pressures up to 25 atm. It was found that the highest adsorption occurs on AC, and the adsorption order of gases follows the trend: $CO_2 >> CH_4 > CO > N_2 >> >> H_2$. The highest isosteric heats of adsorption for most gases were observed for activated carbon AC, which possesses the largest S_{sp} and V_{pore} values. Calculations of adsorption selectivity coefficients for impurity gas/hydrogen pairs using the IAST model show that S_{IAST} (CO_2/H_2) increases by a factor of 1.5–3 compared to S_{id} (CO_2/H_2), while for other gases, the coefficients are comparable.

5. Funding

The study was carried out within the framework of state assignment No. 122012400186-9.

6. Acknowledgements

The authors thank JSC Grasys for providing the adsorbent samples.

7. Conflict of interest

The authors declare no conflict of interest.

References

1. Sircar S, Golden TC. Purification of hydrogen by pressure swing adsorption. *Separation Science and Technology*. 2000;35(5):667-687. DOI:10.1081/SS-100100183

2. Kozlov S, Fateyev V. *Hydrogen energy: current state, problems, prospects*. Moscow: Gazprom VNIIGAZ; 2009. 518 p. (In Russ.)

3. Du Z, Liu C, Zhai J, Guo X, et al. A review of hydrogen purification technologies for fuel cell vehicles. *Catalysts*. 2021;11(3):393. DOI:10.3390/catal11030393

4. Zhang R, Shen Y, Tang Z, Li W, et al. A review of numerical research on the pressure swing adsorption process. *Processes*. 2022;10(5):812. DOI:10.3390/pr10050812

5. Grande CA. Advances in pressure swing adsorption for gas separation. *ISRN Chemical Engineering*. 2012;2012:1-13. DOI:10.5402/2012/982934

6. Lopes FVS, Grande CA, Rodrigues AE. Fast-cycling VPSA for hydrogen purification. *Fuel*. 2012;93: 510-523. DOI:10.1016/j.fuel.2011.07.005

7. Shah G, Ahmad E, Pant KK, Vijay VK. Comprehending the contemporary state of art in biogas enrichment and CO_2 capture technologies via swing adsorption. *International Journal of Hydrogen Energy*. 2021;46(9):6588-6612. DOI:10.1016/j.ijhydene.2020.11.116

8. Sircar S, Golden TC, Rao MB. Activated carbon for gas separation and storage. *Carbon*. 1996;34(1):1-12. DOI:10.1016/0008-6223(95)00128-X

9. Cundy CS, Cox PA. The hydrothermal synthesis of zeolites: history and development from the earliest days to the present time. *Chemical Reviews*. 2003;103(3):663-702. DOI:10.1021/cr020060i

10. Sadighi S., Soleymani R. Synthesis of 5A molecular sieve for hydrogen purification in pressure swing adsorbers. *2nd Iran National Zeolite Conference (2INZC)*. 2015. p. 27-8.

11. Orsikowsky-Sanchez A, Franke C, Sachse A, Ferrage E, et al. Gas porosimetry by gas adsorption as an efficient tool for the assessment of the shaping effect in commercial zeolites. *Nanomaterials*. 2021;11(5):1205. DOI:10.3390/nano11051205

12. Yan KL, Wang Q. Adsorption characteristics of the silica gels as adsorbent for gasoline vapors removal. *IOP Conference Series: Earth and Environmental Science*. 2018;153(2):022010. DOI:10.1088/1755-1315/153/2/022010

13. *BASF: Sorbead®*. Available from: https://chemical-catalysts-and-adsorbents.basf.com/global/en/adsorbents/sorbead-for-ccs [Accessed 09 Jule 2025]

14. Myers AL, Prausnitz JM. Thermodynamics of mixed-gas adsorption. *AIChE Journal*. 1965;11(1):121-127. DOI:10.1002/aic.690110125

15. Frenkel D, Smit B. *Understanding molecular simulation: from algorithms to applications*. San Diego: Academic Press; 2002. 638 p. (Computational science series).

16. Simon CM, Smit B, Haranczyk M. PyIAST: ideal adsorbed solution theory (IAST) python package. *Computer Physics Communications*. 2016;200:364-380. DOI:10.1016/j.cpc.2015.11.016

17. *National institute of standards and technology*. Thermophysical properties of fluid systems n.d. Available from: https://webbook.nist.gov/chemistry/fluid/ [Accessed 17 May 2025].

18. Keppetipola NM, Dissanayake M, Dissanayake P, Karunarathne B, et al. Graphite-type activated carbon from coconut shell: a natural source for eco-friendly non-volatile storage devices. *RSC Advances*. 2021;11(5):2854-2865. DOI:10.1039/D0RA09182K

19. Chen L, Wang YW, He MY, Chen Q, et al. Facile synthesis of 5A zeolite from attapulgite clay for adsorption of n-paraffins. *Adsorption*. 2016;22(3):309-314. DOI:10.1007/s10450-016-9776-y

20. Keller J, Staudt R. *Gas adsorption equilibria. Experimental Methods and Adsorptive Isotherms*. Boston: Springer Science + Business Media, Inc; 2005. 422 p.

21. Karnaukhov A. *Adsorption. The texture of dispersed and porous materials*. Novosibirsk: Nauka Publ. Siberian Enterprise of the Russian Academy of Sciences; 1999. 469 p. (In Russ.)

22. Jung J, Do H, Chung K, Cho M, et al. Adsorption equilibria and kinetics of CO_2, CH_4, CO, N_2, O_2, and H_2 on silica-based adsorbents for H_2 enhancement processes from steel off-gas for the direct reduced iron process. *Chemical Engineering Journal*. 2024;479:147678. DOI:10.1016/j.cej.2023.147678

Information about the authors / Информация об авторах

Nikita S. Krysanov, PhD Student, Lomonosov Moscow State University (MSU), Moscow, Russian Federation; ORCID 0009-0003-4811-7021; e-mail: n.krysanov@mail.ru

Elena A. Berdonosova, Cand. Sc. (Chem.), Senior Researcher, MSU, Moscow, Russian Federation; ORCID 0000-0002-4580-9749; e-mail: ellenganich@highp.chem.msu.ru

Semen N. Klyamkin, D. Sc. (Chem.), Professor, MSU, Moscow, Russian Federation; ORCID 0000-0001-6009-1045; e-mail: klyamkin@highp.chem.msu.ru

Крысанов Никита Сергеевич, аспирант, Московский государственный университет имени М. В. Ломоносова (МГУ), Москва, Российская Федерация; ORCID 0009-0003-4811-7021; e-mail: n.krysanov@mail.ru

Бердоносова Елена Александровна, кандидат химических наук, старший научный сотрудник, МГУ, Москва, Российская Федерация; ORCID 0000-0002-4580-9749; e-mail: ellenganich@highp.chem.msu.ru

Клямкин Семен Нисонович, доктор химических наук, профессор, МГУ, Москва, Российская Федерация; ORCID 0000-0001-6009-1045; e-mail: klyamkin@highp.chem.msu.ru

Received 16 July 2025; Revised 08 September 2025; Accepted 11 September 2025

Original papers
Materials for energy and environment, next-generation photovoltaics, and green technologies

УДК 004.942+544.723.232 DOI: 10.17277/jamt-2025-10-04-351-363

Modeling CO_2, CO, CH_4, and H_2 sorption equilibrium on NaX and CaA zeolites and activated carbon using the Dubinin–Astakhov equation

©Dmitry S. Dvoretsky[a]✉, Stanislav I. Dvoretsky[a], Evgeniy I. Akulinin[a], Evgeny N. Tugolukov[a], Gleb I. Varnikov[a], Vladimir B. Usachev[b]

[a] *Tambov State Technical University, Bld. 2, 106/5, Sovetskaya St., Tambov, 392000, Russian Federation,*
[b] *JSC Research Institute of Scientific Production Association Luch, Protvino branch, 5, Zheleznodorozhnaya St., Protvino, 142281, Russian Federation*

✉ dvoretsky@yahoo.com

Abstract: In light of the findings from experimental studies, adsorption isotherms were obtained for carbon dioxide, carbon monoxide, methane, and hydrogen gases on industrial adsorbents. A methodology has been put forth for calculating the coefficients of the Dubinin–Astakhov equation based on experimental isotherms. This approach enables the determination of the equilibrium adsorption of components of a hydrogen-containing gas mixture with a high degree of accuracy. The approach includes: calculating the limiting adsorption volume of a given adsorbent and the characteristic adsorption energy of a standard gas (nitrogen) for the specified adsorbent using experimental nitrogen adsorption isotherms obtained at a temperature of 77.3 K in the relative pressure range from 0 to 1 for each of the studied adsorbents, namely: NaX, CaA, SKT-4; determining the calculated values of the affinity coefficients, the exponent, and the thermal coefficient of limiting adsorption in the Dubinin–Astakhov equation (for the temperatures and pressures at which the experimental sorption isotherms of the studied gases were obtained), which minimize the residual between the calculated and experimental isotherms; averaging the obtained values of the affinity coefficients and the exponent. The efficacy of the proposed approach is substantiated by the calculation of the parameters of the Dubinin–Astakhov equation for CO_2, CO, and CH_4 using NaX and CaA zeolites and SKT-4 activated carbon. The root mean square deviation between the calculated and experimental data does not exceed 6.6 % over a wide range of pressures (up to 3.0 MPa) and temperatures (293–353 K) for the studied sorbents (zeolites NaX, CaA, and activated carbon SKT-4).

Keywords: hydrogen-containing gas mixture; adsorbent; adsorption separation; adsorption equilibrium; adsorption isotherm; Dubinin–Astakhov equation; zeolite; activated carbon; root mean square error; maximum deviation.

For citation: Dvoretsky DS, Dvoretsky SI, Akulinin EI, Tugolukov EN, Varnikov GI, Usachev VB. Modeling CO_2, CO, CH_4, and H_2 sorption equilibrium on NaX and CaA zeolites and activated carbon using the Dubinin–Astakhov equation. *Journal of Advanced Materials and Technologies*. 2025;10(4):351-363. DOI: 10.17277/jamt-2025-10-04-351-363

Моделирование сорбционного равновесия CO_2, CO, CH_4, H_2 с использованием уравнения Дубинина–Астахова на цеолитах NaX, CaA и активном угле

© Д. С. Дворецкий[a]✉, С. И. Дворецкий[a], Е. И. Акулинин[a], Е. Н. Туголуков[a], Г. И. Варников[a], В. Б. Усачев[b]

[a] *Тамбовский государственный технический университет, ул. Советская, 106/5, пом. 2, Тамбов, 392000, Российская Федерация,*
[b] *АО НИИ НПО «Луч» Протвинский филиал, ул. Железнодорожная, 5, Протвино, 142281, Российская Федерация*

✉ dvoretsky@yahoo.com

Аннотация: По результатам экспериментальных исследований получены адсорбционные изотермы для газов: диоксида углерода, оксида углерода, метана и водорода на промышленных адсорбентах. Предложен подход для расчета коэффициентов уравнения Дубинина–Астахова на основе экспериментальных изотерм, позволяющий

определять величину равновесной адсорбции компонентов водородсодержащей газовой смеси с высокой точностью. Подход включает: расчет значений предельного адсорбционного объема данного адсорбента и характеристической энергии адсорбции стандартного газа (азота) для заданного адсорбента с использованием экспериментальных изотерм адсорбции азота, полученных при температуре 77,3 K в диапазоне относительных давлений адсорбции от 0 до 1 на каждом из исследуемых адсорбентов, а именно: NaX, CaA, СКТ-4; нахождение расчетных значений коэффициентов аффинности, показателя степени, термического коэффициента предельной адсорбции уравнения Дубинина–Астахова (для температур и давлений, при которых получены экспериментальные изотермы сорбции исследуемых газов), обеспечивающих минимальное значение невязки между расчетными и экспериментальными изотермами; усреднение найденных значений коэффициентов аффинности и показателя степени. Эффективность предложенного подхода продемонстрирована на примере расчета параметров уравнения Дубинина–Астахова для CO_2, CO, CH_4 при использовании цеолитов NaX, CaA, активного угля СКТ-4. Среднеквадратическое отклонение между расчётными и экспериментальными данными не превышает 6,6 % в широком диапазоне давлений (до 3,0 МПа) и температур (293…353 K) для изученных сорбентов (цеолиты NaX, CaA, активный уголь СКТ-4).

Ключевые слова: водородсодержащая газовая смесь; адсорбент; адсорбционное разделение; адсорбционное равновесие; изотерма адсорбции; уравнение Дубинина–Астахова; цеолит; активный уголь; среднеквадратическая ошибка; максимальное отклонение.

Для цитирования: Dvoretsky DS, Dvoretsky SI, Akulinin EI, Tugolukov EN, Varnikov GI, Usachev VB. Modeling CO_2, CO, CH_4, and H_2 sorption equilibrium on NaX and CaA zeolites and activated carbon using the Dubinin–Astakhov equation. *Journal of Advanced Materials and Technologies*. 2025;10(4):351-363. DOI: 10.17277/jamt-2025-10-04-351-363

1. Introduction

The pressure swing adsorption (PSA) method has become a prevalent technique in the field of chemical technology, particularly in the context of the delivery and storage of pure technical gases, when relatively low production volumes are required. The present study investigates the application of the PSA method in the separation of hydrogen-containing gas mixtures during hydrogen concentration. The PSA method is implemented in the pressure range (30×10^5 Pa) and at temperatures of 293–333 K. The results demonstrate that the PSA method allows for the production of a gas mixture containing up to 99.99 % vol. hydrogen [1–3].

The contemporary design of gas separation facilities that utilize the PSA method has evolved significantly from the past, when the selection of adsorbent layers and the determination of operating modes were done on an intuitive basis. It is critical for developers of such facilities to consider a comprehensive array of interconnected trends to ensure that the plant is as competitive, efficient, flexible, and reliable as possible. The era of empirical selection and trial and error is coming to a close. In the contemporary realm of design, it is imperative that models encompass the entirety of the intricate processes that occur in tandem during the adsorption separation of gas mixtures. These processes are contingent upon variables such as temperature, pressure, the velocities of components within the gas stream and within the adsorbent (micro, meso, and macro pores), and the nature and rate of redistribution of the sorption volume between gases.

In the process of mathematical modeling of sorption processes in PSA units, it is essential to select isotherms that correctly reflect the equilibrium sorption characteristics of the "solid sorbent – absorbed component" system [4–10]. Modern gas separation calculation models are based on two main theoretical approaches to describing adsorption: surface sorption theory and the concept of volumetric filling of micropores. The first includes the fundamental Langmuir equation and its derivatives [2], while the second includes the Dubinin–Astakhov equation [11, 12].

The concept of volumetric filling of micropores provides a more accurate description of the physics of adsorption-desorption processes in microporous adsorbents, as it takes into account the specific state of the adsorbate, close to the condensed phase, and the energy heterogeneity of micropores [3, 11].

It must be acknowledged that the implementation of both methodologies necessitates the acquisition of experimental adsorption isotherms, their linearization, and the subsequent calculation of the corresponding coefficients derived from the linear forms of the isotherms. Consequently, the coefficients of the equations are derived by solving the inverse problem based on experimental data.

The primary benefit of the Dubinin–Astakhov equation over the Langmuir equation is the classification of parameters into two distinct categories: those that delineate the adsorbent (W_0, microporous volume; E_0, characteristic adsorption energy of standard gas) and those that delineate the adsorbate (φ_i, affinity coefficient; n_i, empirical

exponent; α_i, thermal coefficient of maximum adsorption). This approach enables the determination of the adsorbent constants (W_0, E_0) once from the isotherm of the reference gas. Subsequently, the parameters specific to each adsorbate (φ_i, n_i, α_i) can be determined to describe the isotherms of other gases.

According to the sources cited [1, 11, 13, 14], the ranges of values for the coefficients of the Dubinin–Astakhov equation have been established. These ranges are [0.8–4.0] for the coefficient φ_i and [1–6] for the coefficient n_i. These values are applicable to the most frequently used PSA zeolite adsorbents (NaX, CaA, and activated carbons) in adsorbers [15–22]. The temperature range for sorption processes (293–333 K) for gases included in a hydrogen-containing gas mixture (CO_2, CO, CH_4, H_2) significantly exceeds the critical temperatures of the following components: carbon monoxide (133 K), methane (190 K), hydrogen (33 K). In this regard, it is plausible that the values of the thermal coefficient of maximum adsorption, α_i, incorporated within the Dubinin-Astakhov equation, may exhibit deviation from the calculated values, as delineated in the methodology [11], which is applicable within the temperature range extending from the normal boiling point to the critical temperature.

Different estimates of the values of W_0 and E_0 for adsorbents of the same type (NaX, CaA, activated carbon) [1–3, 11] are explained by the variety of manufacturers and technological features of their production. There is also no single approach to calculating the values of affinity coefficients φ_i. The most common methods include finding the ratio of the parachors of the test and standard gases [1]. According to the Sugden–Quayle method [13], the parachor of the adsorbed gas ω can be calculated as the sum of the structural components of the parachors of the atoms that make up the molecule of the adsorbed gas. According to the McGowan method [14], the parachor of the adsorbed gas ω can be defined as the sum of the structural components of the parachors of the atoms ω_i that make up the molecule of the adsorbed gas, minus the number of bonds in the gas molecule.

Given the ranges of variation that have been described and the options for calculating the coefficients of the Dubinin–Astakhov equation, it is evident that satisfactory precision in characterizing the equilibrium conditions of hydrogen-containing gas mixture components can be attained by developing an approach that encompasses the acquisition and processing of experimental adsorption-desorption isotherms.

The objective of this study is to develop an approach to enhancing the accuracy of describing the isotherms of the adsorption process of hydrogen-containing gas mixture components on microporous adsorbents.

2. Methods and Materials

2.1. Initial materials

Industrial microporous zeolites NaX and CaA [23] and activated carbon SKT-4 (sulfurous potassium peat coal) [24] were utilized as adsorbents.

2.2. Theoretical approaches

A proposed approach is outlined, with the primary objective being the identification of the coefficients of the Dubinin–Astakhov equation that guarantee minimal values for the root mean square error (RMSE) between calculated and experimental values of equilibrium adsorption within the operational temperature and pressure ranges of 293–333 K and 30×10^5 Pa, correspondingly.

The approach encompasses the calculation of the maximum adsorption volume (W_0) and the characteristic adsorption energy (E_0) of a given adsorbent with N_2 using experimental N_2 isotherms at $T = 77.3$ K in the range $P/P_s = 0$–1 for each of the adsorbents under study (NaX, CaA, SKT-4). This approach also involves finding the calculated values of the affinity coefficients φ_i, the exponent n_i, and the thermal coefficient of maximum adsorption α_i of the Dubinin–Astakhov equation (for temperatures and pressures at which experimental adsorption isotherms of the studied gases were obtained), ensuring a minimum discrepancy between the calculated and experimental isotherms. Finally, the approach entails averaging the found values of φ_i and n_i.

To evaluate the effectiveness of the proposed approach, we compared the adsorption values using the φ_i and n_i values found in the previous step and the φ_i values determined from the literature [1, 13, 14] for $n_i = 1, 2, 3$.

Dubinin–Astakhov equation and the dependencies included in it:

$$a_i^* = a_{0i} \exp\left[-\left(\frac{RT \lg\left(P_{si}/P\right)}{\varphi_i E_0} \right)^{n_i} \right]; \qquad (1)$$

$$a_{0i} = \frac{W_0}{V_i^*}\exp\left[-\alpha_i\left(T - T_{\mathrm{b},i}\right)\right]; \quad (2)$$

$$V_i^* = \frac{M_{\mathrm{g},i}}{\rho_i^*}; \quad (3)$$

$$\rho_i^* = 10^3 \rho_{\mathrm{b},i} 10^{-0.434\alpha_i\left(T - T_{\mathrm{b},i}\right)}; \quad (4)$$

$$\alpha_i = \frac{\lg\left(\frac{\rho_{\mathrm{b},i}}{\rho_{\mathrm{cr},i}^*}\right)}{0.434\left(T_{\mathrm{cr},i} - T_{\mathrm{b},i}\right)}; \quad (5)$$

$$\rho_{\mathrm{cr},i}^* = \frac{M_{\mathrm{g},i}}{b_i}; \quad (6)$$

$$b_i = \frac{RT_{\mathrm{cr},i}}{8\cdot 10^{-3} P_{\mathrm{cr},i}}; \quad (7)$$

$$P_{\mathrm{s},i} = \frac{\exp\left(\frac{A_i - F_i}{T - C_i}\right)}{760} 10^5, \quad (8)$$

where a_{0i} is the maximum adsorption value of the i-th component, mol·kg^{-1}; P_{si} is the saturation pressure of the pure adsorbent, Pa; φ_i is the affinity coefficient characterizing the affinity of the adsorbed gas to the standard (N_2); E_0 is thecharacteristic adsorption energy of the standard gas N_2, J·mol^{-1}; n_i is and exponent; W_0 is micropore volume of the adsorbent, cm^3·g^{-1}; V_i^* is molar volume of the adsorbate, m^3·mol^{-1}; α_i is a thermal coefficient of maximum adsorption, K^{-1}; T is adsorption temperature, K; $T_{\mathrm{b},i}$ – boiling temperature of the i-th component of the gas mixture, K; $M_{\mathrm{g},i}$ – molar mass of the i-th component of the gas mixture, g·mol^{-1}; ρ_i^* – adsorbate density at a temperature T above $T_{\mathrm{b},i}$, kg·m^{-3}; $\rho_{\mathrm{b},i}$ – gas density at boiling temperature, kg·m^{-3}; T – adsorption temperature, K; $T_{\mathrm{cr},i}$ – critical temperature of the i-th component of the gas mixture, K; $\rho_{\mathrm{cr},i}^*$ – adsorbate density at critical temperature, kg·m^{-3}; b_i – molar volume constant, m^3·mol^{-1}; R – universal gas constant, J·(mol·K)$^{-1}$; $P_{\mathrm{cr},i}$ – critical pressure of the i-th component of the gas mixture, Pa; A_i, F_i, C_i – Antoine equation constants.

Table 1. Parameter values for calculations with the use of the Dubinin–Astakhov equation

Parameter	CH_4	CO_2	CO	H_2
$M_{\mathrm{g},i}$, g·mol^{-1}	16.04	44.01	28.01	2.02
$\rho_{\mathrm{b},i}$, g·cm^{-3}	0.43	0.78	0.78	0.07
$T_{\mathrm{b},i}$, K	111.7	197.7	81.6	20.4
$T_{\mathrm{cr},i}$, K	190.6	304.2	132.9	33.2
$P_{\mathrm{cr},i}$, ×10^5 Pa	45.4	72.8	34.9	12.8
A_i	15.22	22.59	14.37	13.63
F_i	897.84	3103.39	530.22	164.90
C_i	7.16	0.16	13.15	3.19

The values of the coefficients of the Dubinin–Astakhov equations (1) – (8), as determined on the basis of reference data, are presented in Table 1 [13].

The values of parameters W_0, E_0, φ_i, n_i, α_i were determined on the basis of experimental data.

The calculation of the values of the maximum adsorption volume W_0 and the characteristic adsorption energy E_0 of the standard gas N_2 was performed using the experimental adsorption isotherm of the standard gas N_2 in the range $P/P_s = 0$–1 for each adsorbent (NaX, CaA, SKT-4). The N_2 isotherms at $T = 77.3$ K in the range $P/P_s = [0–1]$ were obtained using the Autosorb IQ Nova 1200e analyzer (Quantochrome Instruments), after which W_0 and E_0 were calculated using the method described in [11]. Next, a combination of values $[\varphi_i, n_i]$ was selected at which the smallest root mean square deviation δ of the experimental and calculated isotherms was observed at k mean values $[\overline{\varphi}_j, \overline{n}_j]$, where k is the number of experimental isotherms. The values $\overline{\varphi}_j, \overline{n}_j$ were determined as the arithmetic mean φ_j, n_j found for: three temperatures ($k = 3$, $T = 293$, 313, 333 K), for the boundary values of the interval ($k = 2$, $T = 293$, 333 K), for the average temperature ($k = 1$, $T = 313$ K).

The parameters φ_j, n_j, α_i of the Dubinin–Astakhov equation were determined for three temperatures (293, 313, 333 K) based on the results of solving the problem of minimizing the discrepancy

function between the values calculated according to equations (1), (2) with the found coefficients φ_j, n_i, α_i and the experimental $a_i^{*,e}(P,T)$ isotherms. The problem of minimizing the discrepancy function is formulated as follows. For the *i*-th component of the gas mixture, it was necessary to determine the parameters φ_j, n_j and α_i in equations (1) and (2) at temperature T_j, at which there was achieved a minimum value of the root mean square deviation δ between the experimental $a_i^{*,e}$ and calculated $a_i^{*,c}$ values of equilibrium adsorption at given *P*, T_j:

$$\delta_j\left(\hat{a}_i^*\right) = \min_{\varphi_j, n_j, \alpha_j} \delta_j\left(a_i^*\left(\varphi_j, n_j, \alpha_i\right)\right), \qquad (9)$$

where δ is calculated using the formula

$$\delta = \sqrt{\frac{1}{N}\sum_{l=1}^{m}\left(\frac{a_l^{*,e} - a_l^{*,c}}{a_l^{*,e}}\right)} 100\%, \qquad (10)$$

where *N* is the total number of experimental points *l*.

The problem (9), (10) was solved in the MatLab software environment using the fmincon function [25].

The experimental isotherms $a_i^{*,e}\left(P, T_j\right)$ for CO_2, CO, CH_4, H_2 at $T_j = 293$, 313, 333 K in the range $P_i = [1–30]\times10^5$ Pa were obtained using the ISorb HP1 analyzer (Quantochrome Instruments).

The adsorption values were determined using φ_i data from [1] and calculated according to the Sugden–Quayle [13] and McGowan [14] methods at $n_i = 1, 2, 3$, with α_i values determined according to the formula (5).

3. Results and Discussion

Experimental adsorption isotherms for the model gas (nitrogen) in the relative pressure range $P/P_s = [0–1]$ at 77.3 K are shown in Fig. 1*a*, *c*, *e*, and the isotherms in rectifying coordinates $\left[\lg a_i^* - (\lg P_{0i}/P)^{n_{N_2}^*}\right]$ – in Fig. 1*b*, *d*, *f*.

The verification using Fisher criterion at a significance level of 5 % confirmed that the experimental N_2 sorption isotherms on NaX, CaA, and SKT-4 were adequately described by the linear dependencies (Fig. 1*b*, *d*, *f*).

Table 2 presents the calculated values of W_0 and E_{0,N_2} obtained by processing the linearized adsorption isotherms (Fig. 1).

The CO_2, CO, CH_4, H_2 sorption regions limited by experimental isotherms at $T = 293$ K (upper line) and $T = 333$ K (lower line) in the range $P_i = [1–30]\times10^5$ Pa are shown in Fig. 2.

For NaX and CaA zeolites, the CO_2 isotherms are extremely steep within the initial pressure range of 0 to 1×10^5 Pa. After this range, a rapid decrease in the slope of the isotherms is observed within the range of 1×10^5 Pa to 10×10^5 Pa (see Fig. 2*a*, *b*). At $P > 10\times10^5$ Pa, the slope of the isotherm becomes minimal and practically ceases to change. An increase in the adsorption value from $P = 10\times\times10^5$ Pa to $P = 30\times10^5$ Pa (a threefold increase in pressure) leads to an increase in *a* of only 5–10 % for NaX and 10–15 % for CaA (Fig. 2*a*, *b*). The CH_4 and CO isotherms on NaX and CaA are flatter than the CO_2 isotherms. The CH_4 and CO isotherms on NaX are less convex than those on CaA. The CO_2, CO, and CH_4 sorption isotherms on SKT-4 are flat across the entire pressure range (up to 30×10^5 Pa).

Analysis of the isotherm changes shown in Fig. 2 revealed that the most significant change in equilibrium sorption values *a* occurs when *T* changes from 293 to 333 K for CO_2 on SKT-4 (up to 32 %) and for CH_4 on CaA (up to 22 %). The CH_4 and CO sorption areas on NaX almost completely overlap (Fig. 2*a*), while they partially overlap on CaA (Fig. 2*b*). The H_2 isotherms are close to linear over the entire *P* range ($1–30\times10^5$ Pa) on NaX, CaA, and SKT-4.

The values of the parameters $\overline{\varphi}_j, \overline{n}_j$, α_i, calculated at different *k* based on solving equations (12) and (13), are presented in Table 3.

Analysis of the ranges of values $\overline{\varphi}_j, \overline{n}_j$, showed that the greatest deviation $\overline{\varphi}_j$ from the arithmetic mean values calculated at $k = 1, 2, 3$, is observed for CO_2 on all adsorbents: 3.8 % on NaX, 9.5 % on CaA, 1.4 % on SKT-4. It can be assumed that this is due to the large angle of inclination of CO_2 isotherms on these adsorbents compared to CO, CH_4, and H_2. No clear trend is observed for $\overline{n}_j$, and the maximum deviation from the mean value is 5.0 % for CO_2 on CaA, 3.0 % for CH_4 on NaX, and 1.54 % for H_2 on SKT-4 (Fig. 3).

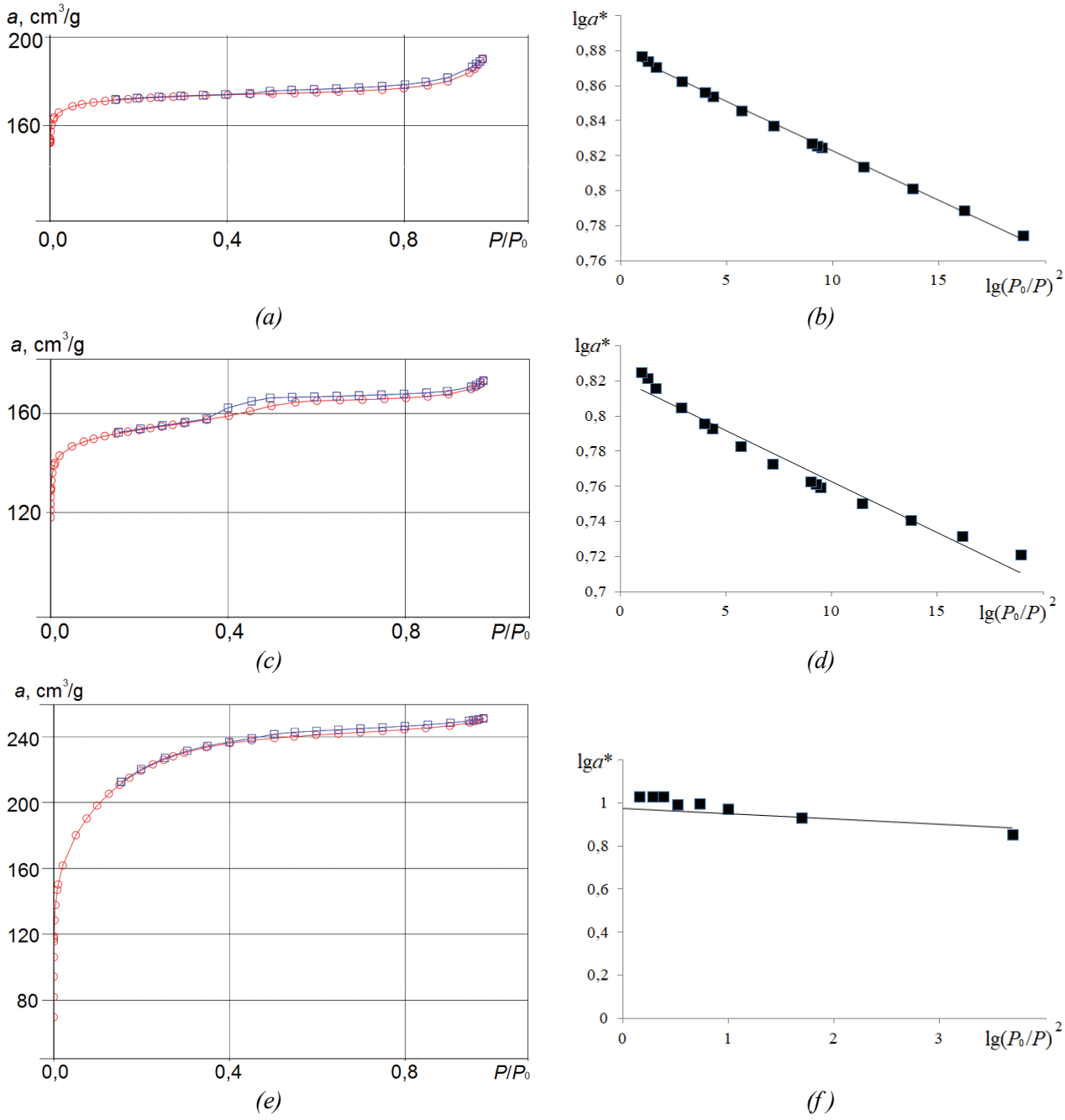

Fig. 1. Experimental sorption isotherms of model gas (nitrogen):
a, *b* on NaX zeolite; *c*, *d* on CaA zeolite; *e*, *f* on SKT-4 activated carbon; *b*, *d*, *f* in rectifying coordinates

Table 2. Linear equations of N_2 isotherms and values of W_0 and E_0

Adsorbent	Linear equation of the isotherm	W_0, $cm^3 \cdot g^{-1}$	E_0, $J \cdot mol^{-1}$
NaX	$\lg a^*_{N_2} = 0.8793 - 0.0057\left(P_{0,N_2}/P\right)^{2,1}$	0.265	12834
CaA	$\lg a^*_{N_2} = 0.8210 - 0.0058\left(P_{0,N_2}/P\right)^{2,3}$	0.230	12796
SKT-4	$\lg a^*_{N_2} = 0.9214 - 0.0208\left(P_{0,N_2}/P\right)^{1,8}$	0.293	6731

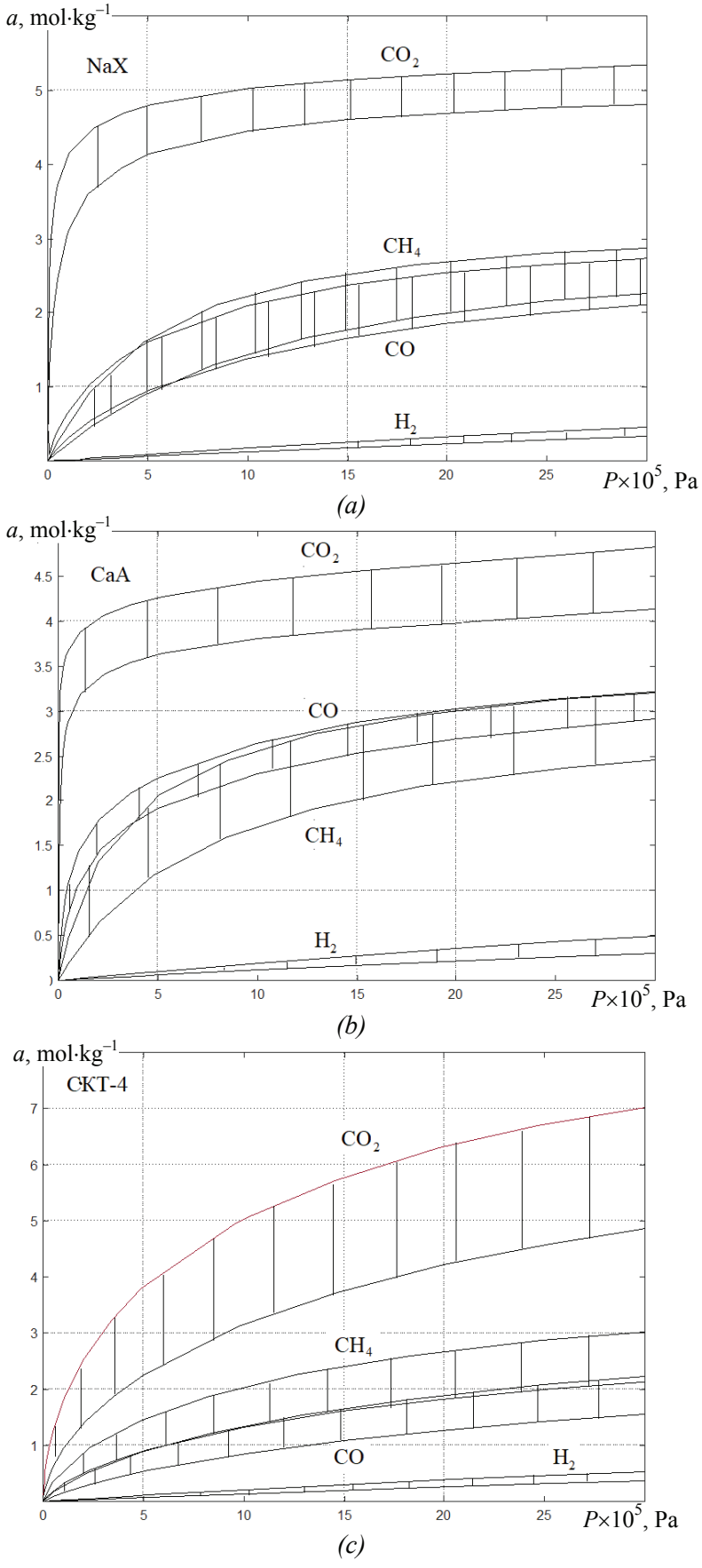

Fig. 2. Experimental adsorption isotherms of components of a hydrogen-containing gas mixture on: *a* – NaX zeolite; *b* – CaA zeolite; *c* – activated carbon SKT-4

Table 3. Values of the coefficients of equations (1) and (2) for different calculation options

Gas	k	$\overline{\varphi}_j$			$\overline{n}_j$			$\alpha_i \times 10^3$		
		NaX	CaA	SKT-4	NaX	CaA	SKT-4	NaX	CaA	SKT-4
CH_4	3	1.17	1.14	1.36	3.01	2.64	1.88	2.30	1.60	1.70
	2	1.16	1.14	1.35	2.96	2.65	1.88	2.20	1.50	1.70
	1	1.21	1.13	1.37	3.12	2.63	1.89	2.50	1.80	1.80
CO	3	0.90	1.46	1.27	2.10	2.54	1.81	1.70	1.50	2.00
	2	0.90	1.46	1.28	2.09	2.55	1.83	1.70	1.50	2.00
	1	0.91	1.47	1.25	2.12	2.54	1.79	1.70	1.50	1.90
CO_2	3	3.82	4.47	1.43	3.30	3.01	1.70	0.50	0.31	2.60
	2	3.74	4.21	1.43	3.24	2.92	1.69	0.50	0.41	2.70
	1	4.00	4.99	1.46	3.33	3.19	1.73	0.60	0.11	2.50
H_2	3	0.30	0.29	0.56	0.92	0.89	0.87	0.06	0.02	0.02
	2	0.30	0.30	0.56	0.92	0.90	0.87	0.07	0.02	0.02
	1	0.30	0.29	0.55	0.91	0.86	0.85	0.03	0.03	0.02

Based on the analysis of maximum root mean square deviations δ and maximum discrepancies Δ, acceptable accuracy in calculating equilibrium conditions for CO_2, CO, CH_4, and H_2 on NaX, CaA, and SKT-4 requires three experimental isotherms obtained at the boundaries (293 and 333 K) and in the middle (313 K) of the sorption process temperature range.

Despite the small values of δ for H_2, the analysis shows that the maximum deviations Δ between the experimental and calculated data exceed 10 % for all adsorbents. This renders the proposed approach unusable for calculating equilibrium adsorption values for H_2 in engineering calculations.

Analysis of the maximum deviations of H_2 adsorption isotherms at 293 and 333 K from the average values (Fig. 2, Table 4) showed that they range from 14 to 18 %. Therefore, based on the experimental isotherms, formal linear dependencies were obtained for the temperature range 293–333 K, which for NaX have the form:

$$a^*_{H_2} = (462 - T)\,10^{-9}\,P_{H2}, \qquad (11)$$

for CaA

$$a^*_{H_2} = (642 - 2T)\cdot 10^{-9} P_{H2}; \qquad (12)$$

for SKT-4

$$a^*_{H_2} = (942 - 2.6T)\cdot 10^{-9} P_{H2}. \qquad (13)$$

The values of φ_i, n_i found using the proposed approach, at which the smallest root mean square deviation of the calculated and experimental data was observed, are presented in Table 4.

Analysis of the data in Table 4 showed that, when calculating the equilibrium conditions for CO_2, CH_4, and CO on NaX and SKT-4 adsorbents at 353 K (which exceeds the upper limit of the experimental data, 333 K), the equilibrium adsorption value prediction remains acceptable for CO_2 and CO on NaX and SKT-4. However, for CH_4 on NaX and SKT-4, the maximum deviation exceeds 10 %.

The results of calculating the parameter φ_i values according to the method [1], the Sugden–Quayle [13], and the McGowan [14] methods are presented in Table 5.

As shown in Table 5, the calculated values of the affinity coefficient, φ_i, vary significantly. For CO_2, φ_{CO_2} ranges from 1.25 to 1.40 (±5.6 %) on SKT-4 and from 1.29 to 2.31 (±71.6 %) on NaX and CaA zeolites. For CO, φ_{CO} varies from 0.61 to 1.03 (±34.5 %) on SKT-4 and NaX and CaA zeolites. For CH_4, φ_{CH_4} varies from 1.22 to 2.02 (±34.0 %) on SKT-4 and NaX and CaA.

The values of φ_i calculated using the proposed approach align well with the intervals found for CH_4 on SKT-4 (Table 4). The values of φ_i for CO_2 and CO on SKT-4 are close to the upper limits of the intervals. On zeolites, the values of φ_i for CO and CH_4 on NaX and CaA are consistent with the found intervals.

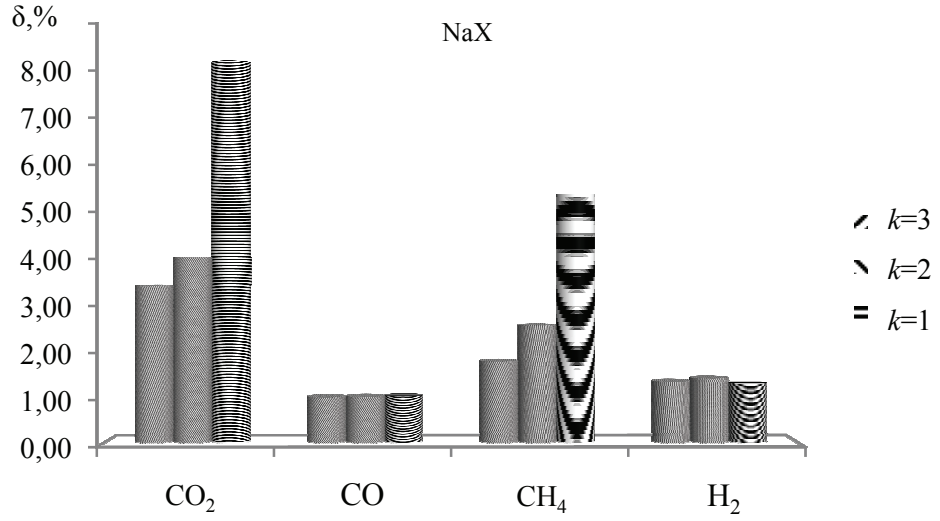

(a)

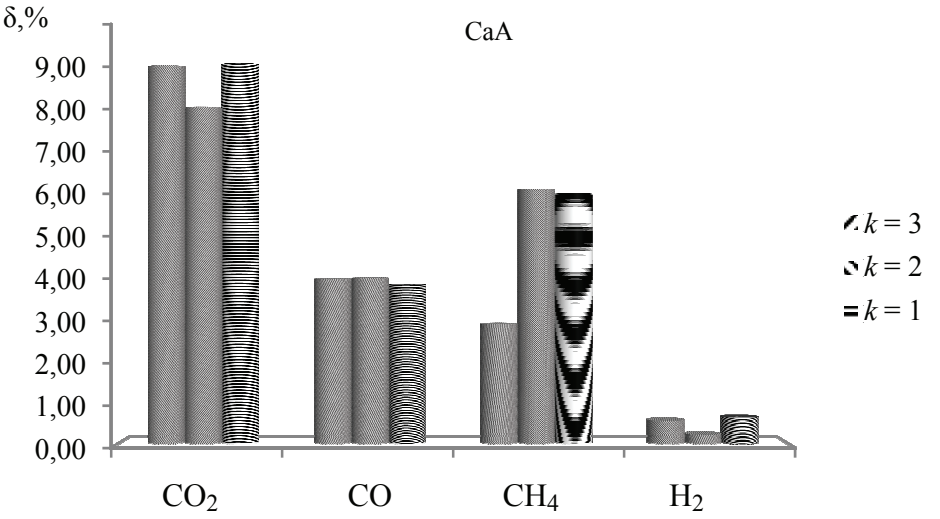

(b)

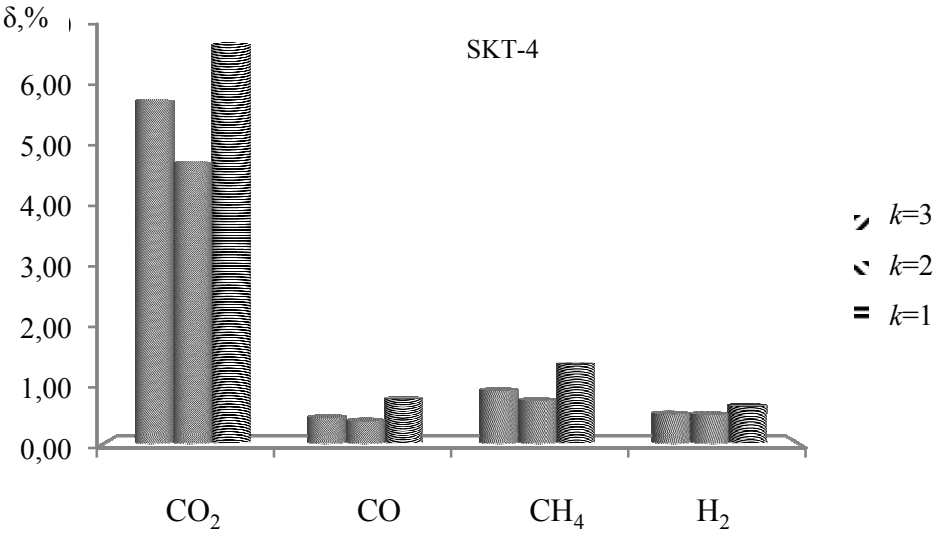

(c)

Fig. 3. Maximum values of the root mean square error:
a – on NaX zeolite; *b* – on CaA zeolite; *c* on SKT-4 activated carbon

Table 4. Root mean square deviations of calculations using the Dubinin–Astakhov equation with the coefficients found in equations (1) and (2)

Adsorbent	W_0, $cm^3 \cdot g^{-1}$	E_0, $J \cdot mol^{-1}$	Gas	φ_i	n_i	$\alpha_i \times 10^3$, K^{-1}	Error, % at T, K							
							293		313		333		353	
							δ^*	Δ	δ^*	Δ	δ^*	Δ	δ^*	Δ
NaX	0.265	12834	CO_2	3.82	3.30	0.5	3.4	4.3	4.7	2.3	5.8	6.0	6.3	8.6
			CO	0.90	2.10	1.7	1.0	0.2	0.1	0.1	0.1	0.7	1.4	5.8
			CH_4	1.17	3.01	2.3	0.6	4.0	0.9	4.8	1.8	8.7	4.3	13.4
CaA	0.230	12796	CO_2	4.47	3.01	0.31	4.7	9.1	2.7	3.5	4.8	0.3	n/d	n/d
			CO	1.47	2.54	1.5	0.5	3.8	0.1	1.0	0.5	0.7	n/d	n/d
			CH_4	1.14	2.64	1.6	0.9	4.5	2.9	8.4	0.1	2.0	n/d	n/d
SKT-4	0.293	6731	CO_2	1.43	1.69	2.7	4.8	4.8	0.6	2.4	1.8	1.5	3.9	9.2
			CO	1.28	1.83	2.0	0.4	3.6	0.1	1.6	0.4	5.3	1.4	9.7
			CH_4	1.35	1.88	1.7	0.9	2.8	0.5	3.4	0.8	5.0	3.1	11.7

Table 5. The values of φ_i when using different calculation methods

Method	SKT-4						NaX/CaA					
	Gas	C	ω_i	l/*s*	ω	φ	Gas	*C*	ω_i	l/*s*	ω	φ
Keltsev [1]	CH_4	n/d	n/d	n/d	n/d	1.52	CH_4	n/d	n/d	n/d	n/d	1.52
	CO_2	n/d	n/d	n/d	n/d	1.25	CO_2	n/d	n/d	n/d	n/d	1.25
	CO	n/d	n/d	n/d	n/d	0.61	CO	n/d	n/d	n/d	n/d	0.61
	N_2	n/d	n/d	n/d	n/d	1.00	N_2	n/d	n/d	n/d	n/d	1.00
Sugden–Quayle [13]	CH_4	C	9.00	1	71	2.02	CH_4	C	9.00	1	71	2.02
		H	15.5	4				H	15.5	4		
	CO_2	C	9.00	1	49	1.40	CO_2	C	9.00	1	49	1.40
		O	20.0	2				O	20.0	2		
	CO	C	9.00	1	29	0.83	CO	C	9.00	1	29	0.83
		O	20.0	1				O	20.0	1		
	N_2	N	17.5	2	35	1.00	N_2	N	17.5	2	35	1.00
McGowan [14]	CH_4	C	0.89	4	1.418	1.22	CH_4	C	0.89	4	1.418	1.22
		H	0.47					H	0.47			
	CO_2	C	0.89	2	1.494	1.29	CO_2	C	0.89	2	1.494	1.29
		O	0.64					O	0.64			
	CO	C	0.89	1	1.192	1.03	CO	C	0.89	1	1.192	1.03
		O	0.64					O	0.64			
	N_2	N	0.75	1	1.162	1.00	N_2	N	0.75	1	1.162	1.00

N o t e : ω – parachor; *C* – gas molecule component; *l* – number of atoms of the component in the molecule (method [13]); *s* – number of bonds in the molecule (method [14]); n/d – no data available.

However, the values of φ_i for CO_2 on NaX and CaA, as well as for CO on CaA, are above the found intervals. The indicated deviations from the φ_i value ranges found in the literature for zeolites (Table 5) are observed for extremely steep isotherms in the initial pressure range (CO_2 on NaX and CaA and CO on CaA).

Table 6. Comparison of errors in calculating equilibrium adsorption value at 293 K

Adsorbent	W_0, $cm^3 \cdot g^{-1}$	E_0, $J \cdot mol^{-1}$	Gas	Method	φ_i	n_i	$\alpha_i \times 10^3$, K^{-1}	δ^*, %
NaX	0.265	12834	CO_2	SQ	1.40	2.00	0.5	17.40
				p/a	3.82	3.30	0.5	3.40
			CO	McG	1.03	1.00	1.7	7.70
				p/a	0.90	2.10	1.7	0.98
			CH_4	McG	1.22	2.00	2.3	2.90
				p/a	1.17	3.01	2.3	0.61
CaA	0.230	12796	CO_2	SQ	1.40	2.00	0.31	17.40
				p/a	4.47	3.01	0.31	4.68
			CO	McG	1.03	1.00	1.9	7.70
				p/a	1.47	2.54	1.5	0.50
			CH_4	K	1.34	3.00	1.6	0.50
				p/a	1.14	2.64	1.6	0.92
SKT-4	0.293	6731	CO_2	SQ	1.40	2.00	2.7	17.40
				p/a	1.43	1.69	2.7	4.75
			CO	McG	1.03	1.00	2.0	7.70
				p/a	1.28	1.83	2.0	0.37
			CH_4	McG	1.22	2.00	1.7	2.90
				p/a	1.35	1.88	1.7	0.89

N o t e : K – Keltsev [1] method; SQ – Sugden-Quayle method; McG – McGowan method; p/a – results when using the proposed approach.

Table 7. Comparison of errors in calculating equilibrium adsorption value at 333K

Adsorbent	W_0, $cm^3 \cdot g^{-1}$	E_0, $J \cdot mol^{-1}$	Gas	Method	φ_i	n_i	$\alpha_i \times 10^3$, K^{-1}	δ^*, %
NaX	0.265	12834	CO_2	SQ	1.40	2.00	0.5	48.30
				p/a	3.82	3.30	0.5	5.80
			CO	McG	1.03	1.00	1.7	3.40
				p/a	0.90	2.10	1.7	0.03
			CH_4	SQ	2.02	3.00	2.3	9.70
				p/a	1.17	3.01	2.3	1.76
CaA	0.230	12796	CO_2	SQ	1.40	2.00	0.31	48.30
				p/a	4.47	3.01	0.31	4.75
			CO	McG	1.03	1.00	1.9	3.40
				p/a	1.47	2.54	1.5	0.50
			CH_4	SQ	2.02	3.00	1.6	9.70
				p/a	1.14	2.64	1.6	0.12
SKT-4	0.293	6731	CO_2	SQ	1.40	2.00	2.7	48.30
				p/a	1.43	1.69	2.7	1.83
			CO	McG	1.03	1.00	2.0	3.40
				p/a	1.28	1.83	2.0	0.35
			CH_4	K	1.52	2.00	1.7	0.50
				p/a	1.35	1.88	1.7	0.48

The results of comparing the minimum root mean square deviations achieved using the proposed approach (with the parameters presented in Table 4) with those based on literature data (selected from the sets of φ_i values in Table 6 at n_i =1, 2, 3) are shown in Tables 6 and 7.

An analysis of Tables 6 and 7 showed that, to ensure minimum deviations δ for different temperature intervals in the range of 293–333 K, different methods must be used to calculate φ_i (Keltsev [1], Sugden-Quayle and McGowan methods, as presented in the literature). However, there are no recommendations for selecting these methods.

Using the proposed approach yields significantly lower δ* values (no greater than 6.6 %) across the entire operating pressure range (up to 30×10^5 Pa) and temperature range (293–333 K).

4. Conclusion

The article proposes an approach for calculating equilibrium adsorption values of components in a hydrogen-containing gas mixture of CO_2, CO, and CH_4 at pressures up to 30×10^5 Pa and temperatures between 293 and 333 K, with an accuracy of no more than 6.6 % (in terms of standard deviation). Three experimental adsorption isotherms of the components of a hydrogen-containing gas mixture (CO_2, CO, and CH_4) on NaX, CaA, and SKT-4 are required, obtained at temperatures of 293, 313, and 333 K.

For all three adsorbents, the largest standard deviation values are observed for CO_2, which has a large isotherm inclination angle in the initial pressure range compared to CO, and CH_4on NaX, CaA, and SKT-4. Differences in affinity coefficient values for zeolites, as determined by the proposed approach versus literature data, are also observed for isotherms with a large slope angle in the initial pressure range (CO_2 on NaX and CaA, and CO on CaA).

It has been demonstrated that the equilibrium adsorption values of CO_2 and CO on NaX and SKT-4 can be calculated with a maximum deviation of no more than 10 % outside the temperature range of 293–333 K (at 253 K), for which the parameters of the Dubinin–Astakhov equation were calculated.

However, based on the analysis of the maximum deviations of the calculated and experimental isotherms, it was determined that using the proposed approach to calculate the equilibrium adsorption values of H_2 in the temperature range of 293–333 K on NaX, CaA, and SKT-4 does not provide sufficient accuracy for engineering calculations. Therefore, formal linear equilibrium dependencies were obtained based on experimental isotherms on NaX, CaA, and SKT-4 for the temperature range of 293–333 K.

5. Acknowledgements

The authors would like to express their gratitude to the staff of the Core Research Facility “Production and Application of Multifunctional Nanomaterials” of Tambov State Technical University for their help and support in carrying out this work.

6. Conflict of interests

The authors declare no conflict of interests.

References

1. Kel'tsev NV. *Fundamentals of adsorption technology*. Moscow: Khimiya; 1976. 512 p. (In Russ.)

2. Ruthven DM, Farooq S, Knaebel KS. *Pressure swing adsorption*. New York: VCH Publishers; 1993. 189 p.

3. Shumyatsky YI. *Industrial Adsorption Processes*. Moscow: KolosS; 2009. 183 p. (In Russ.)

4. Dvoretskii SI, Dvoretskii DS, Akulinin EI, Meronyuk KI, et al. Modern approaches to development of flexible pressure swing adsorption units for separation of hydrogen-containing gaseous mixtures. *Theoretical Foundations of Chemical Engineering*. 2024;58(6):1957-1979. DOI:10.1134/S0040579525601013

5. Akulinin EI, Ishin AN, Skvortsov SA, Dvoretskiy DS, Dvoretskiy SI. Numerical study of the dynamics of the adsorption separation of a gas mixture and hydrogen concentration. *Khimicheskaya tekhnologiya = Theoretical Foundations of Chemical Engineering*. 2018;19(8):368-375. (In Russ.)

6. Akulinin E, Golubyatnikov O, Dvoretsky D, Dvoretsky S. Methodology for creating and studying units for adsorption separation and purification of gas mixtures. *Journal of Advanced Materials and Technologies*. 2021;6(3):179-203. DOI:10.17277/jamt.2021.03.pp.179-203

7. Akulinin EI, Golubyatnikov OO, Dvoretsky DS, Dvoretsky SI. A numerical study of heat and mass exchange processes in swing adsorption device for oxygen-enriched air. *Advanced Materials & Technologies*. 2019; (3(15)):056-065. DOI:10.17277/amt.2019.03.pp.056-065

8. Delgado JA, Agueda VI, Uguina MA, Sotelo JL, Brea P. Hydrogen recovery from off-gases with nitrogen-rich impurity by pressure swing adsorption using CaX and 5A zeolites. *Adsorption*. 2015;21(1-2):107-123. DOI:10.1007/s10450-015-9654-z

9. Oreggioni GD, Brandani S, Luberti M, Baykan Y, et al. CO_2 capture from syngas by an adsorption process at a biomass gasification CHP plant: Its comparison with amine-based CO_2 capture. *International Journal of Greenhouse Gas Control.* 2015;35:71-81. DOI:10.1016/ j.ijggc.2015.01.008

10. Shi W, Yang H, Shen Y, Fu Q et al. Two-stage PSA/VSA to produce H_2 with CO_2 capture via steam methane reforming (SMR). *International Journal of Hydrogen Energy.* 2018;43(41):19057-19074. DOI:10.1016/j.ijhydene.2018.08.077

11. Dubinin MM. *Adsorption and Porosity*. Moscow: VAKhZ; 1972. 124 p. (In Russ.)

12. Dubinin MM. Fundamentals of the theory of adsorption in micropores of carbon adsorbents:

characteristics of their adsorption properties and microporous structures. *Carbon*. 1989;27(3):457-467. DOI:10.1016/0008-6223(89)90078-X

13. Quayle OR. The parachors of organic compounds. An interpretation and catalogue. *Chemical Reviews*. 1953;53(3):439-589. DOI:10.1021/cr60166a003

14. McGowan JC, Mellors A. Molecular volumes and the parachor. In: McGowan JC, Phillips GT. (eds.), *Molecular volumes in chemistry and biology: Applications including partitioning and toxicity*. Halsted Press; 1986. p. 1-20.

15. Park J, Beum H, Han S, Cho D, Cho K. *Pressure swing adsorption process and pressure swing adsorption apparatus*. United States patent 10,933,366. 02 March 2021.

16. Park Y, Kang JH, Moon DK, Jo YS, Lee CH. Parallel and series multi-bed pressure swing adsorption processes for H_2 recovery from a lean hydrogen mixture. *Chemical Engineering Journal.* 2021;408:127299. DOI:10.1016/j.cej.2020.127299

17. Zhang N, Bénard P, Chahine R, Yang T, Xiao J. Optimization of pressure swing adsorption for hydrogen purification based on Box-Behnken design method. *International Journal of Hydrogen Energy.* 2021;46(7): 5403-5417. DOI:10.1016/j.ijhydene.2020.11.045

18. Brea P, Delgado JA, Águeda VI, Gutiérrez P, Uguina MA. Multicomponent adsorption of H_2, CH_4, CO and CO_2 in zeolites NaX, CaX and MgX. Evaluation of performance in PSA cycles for hydrogen purification. *Microporous and Mesoporous Materials*. 2019;286:187-198. DOI:10.1016/j.micromeso.2019.05.021

19. Luberti M, Brown A, Balsamo M, Capocelli M. Numerical analysis of VPSA technology retrofitted to steam reforming hydrogen plants to capture CO_2 and produce blue H_2. *Energies.* 2022;15(3). DOI:10.3390/en15031091

20. Yang SI, Park JY, Choi DK, Kim SH. Effects of the residence time in four-bed pressure swing adsorption process. *Separation Science and Technology*. 2009;44(5): 1023-1044. DOI:10.1080/01496390902729122

21. Abdeljaoued A, Relvas F, Mendes A, Chahbani MH. Simulation and experimental results of a PSA process for production of hydrogen used in fuel cells. *Journal of Environmental Chemical Engineering*. 2018;6(1):338-355. DOI:10.1016/j.jece.2017.12.010

22. Li H, Liao Z, Sun J, Jiang, B et al. Modelling and simulation of two-bed PSA process for separating H_2 from methane steam reforming. *Chinese Journal of Chemical Engineering*. 2019;27(8):1870-1878. DOI:10.1016/ j.cjche.2018.11.022

23. *KNT group production of sorbents and catalysts*. [Website]. Available from: https://www.kntgroup.ru/ru/ main [Accessed 03 February 2025].

24. *JSC "Experimental Chemical Plant"*. [Website]. URL: https://лидеркарбон.рф/ [Accessed 03 February 2025].

25. D'yakonov VP, Kruglov VA. *Matlab extension packs: A special reference book*. Saint Petersburg: Piter; 2001. 475 p. (In Russ.)

Information about the authors / Информация об авторах

Dmitry S. Dvoretsky, D. Sc. (Eng.), Professor, Tambov State Technical University (TSTU), Tambov, Russian Federation; ORCID 0000-0002-4352-810X; e-mail: dvoretsky @yahoo.com

Stanislav I. Dvoretsky, D. Sc. (Eng.), Professor, TSTU, Tambov, Russian Federation; ORCID 0000-0002-7571-3748; e-mail: sdvoretsky@mail.tstu.ru

Evgeniy I. Akulinin, D. Sc. (Eng.), Associate Professor, TSTU, Tambov, Russian Federation; ORCID 0000-0003-0848-4380; e-mail: akulinin-2006@yandex.ru

Evgeny N. Tugolukov, D. Sc. (Eng.), Professor, TSTU, Tambov, Russian Federation; ORCID 0000-0003-1766-3786; e-mail: tugolukov.en@mail.ru

Gleb I. Varnikov, Student, TSTU, Tambov, Russian Federation; e-mail: glebvarnikov@gmail.com

Vladimir B. Usachev, Head of JSC Research Institute of Scientific Production Association Luch, Protvino branch, Protvino, Russian Federation; e-mail: npo@sialuch.ru

Дворецкий Дмитрий Станиславович, доктор технических наук, профессор, Тамбовский государственный технический университет (ТГТУ), Тамбов, Российская Федерация; ORCID 0000-0002-4352-810X; e-mail: dvoretsky@yahoo.com

Дворецкий Станислав Иванович, доктор технических наук, профессор, ТГТУ, Тамбов, Российская Федерация; ORCID 0000-0002-7571-3748; e-mail: sdvoretsky@mail.tstu.ru.

Акулинин Евгений Игоревич, доктор технических наук, доцент, ТГТУ, Тамбов, Российская Федерация; ORCID 0000-0003-0848-4380; e-mail: akulinin-2006@yandex.ru

Туголуков Евгений Николаевич, доктор технических наук, профессор, ТГТУ, Тамбов, Российская Федерация; ORCID 0000-0003-1766-3786; e-mail: tugolukov.en@mail.ru

Варников Глеб Игоревич, студент, ТГТУ, Тамбов, Российская Федерация; e-mail: glebvarnikov@ gmail.com

Усачев Владимир Борисович, директор протвинского филиала АО «НИИ НПО «Луч», Протвино, Российская Федерация, e-mail: npo@sialuch.ru

Received 27 August 2025; Revised 03 October 2025; Accepted 09 October 2025

Reviews

Materials for energy and environment, next-generation photovoltaics, and green technologies

УДК 541.183.2:539.19:661.7 DOI: 10.17277/jamt-2025-10-04-364-375

The role of potential energy landscape exploration in the development of new electrolyte solutions

© Nadezhda A. Andreeva[a]✉, Vitaly V. Chaban[b]

[a] *Peter the Great St. Petersburg Polytechnic University, 29, Politekhnicheskaya St., Saint Petersburg, 195251, Russian Federation,*
[b] *Yerevan State University, 1, Alek Manukyan St., Yerevan, 0025, Republic of Armenia*

✉ nadezhda.a.andreeva@gmail.com

Abstract: The development of new electrolyte solutions with improved characteristics is a key challenge for creating high-performance batteries, fuel cells, supercapacitors, and other electrochemical devices. The study of the potential energy landscape (PEL) plays an important role in this process, providing information about the interactions between solution components at the molecular level. In this work, we review the practice of applying PEL research methods based on classical and quantum-chemical algorithms to analyze the structure, dynamics, and thermodynamic properties of electrolyte solutions. Intermolecular and ion-molecular interactions at the microscopic level, which determine the macroscopic properties of the electrolyte solution, are considered in detail. The importance of identifying stable configurations of ions and their solvates is emphasized. PEL analysis allows for the systematic determination of the most probable structures and complexes formed in solution, which is important for understanding ion transport mechanisms. The study of the PEL allows for the determination of the energy barriers that must be overcome for ion migration, which is related to the conductivity of the electrolyte. The application of PEL research methods in combination with experimental data opens up new possibilities for the rational design of electrolyte solutions with desired physicochemical properties.

Keywords: electrolyte solution; molecular modeling; molecular dynamics; quantum chemistry; potential energy landscape.

For citation: Andreeva NA, Chaban VV. The role of potential energy landscape exploration in the development of new electrolyte solutions. *Journal of Advanced Materials and Technologies*. 2025;10(4):364-375. DOI: 10.17277/jamt-2025-10-04-364-375

Роль исследования ландшафта потенциальной энергии в разработке новых электролитных растворов

© Н. А. Андреева[a]✉, В. В. Чабан[b]

[a] *Санкт-Петербургский политехнический университет Петра Великого, ул. Политехническая, 29, Санкт-Петербург, 195251, Российская Федерация,*
[b] *Ереванский государственный университет, ул. Алека Манукяна, 1, Ереван, 0025, Республика Армения*

✉ nadezhda.a.andreeva@gmail.com

Аннотация: Разработка новых электролитных растворов с улучшенными характеристиками является ключевой задачей для создания высокоэффективных аккумуляторов, топливных элементов, суперконденсаторов и других электрохимических устройств. Исследование ландшафта потенциальной энергии (ЛПЭ) играет важную роль в этом процессе, предоставляя информацию о взаимодействиях между компонентами раствора на молекулярном уровне. В данной работе рассмотрена практика применения методов исследования ЛПЭ, основанных на классических и квантово-химических алгоритмах, для анализа структуры, динамики и термодинамических свойств электролитных растворов. Подробно рассматриваются межмолекулярные и ион-молекулярные взаимодействия на микроскопическом уровне, определяющие макроскопические свойства электролитного

раствора. Подчеркнута важность идентификации стабильных конфигураций ионов и их сольватов. Анализ ЛПЭ позволяет систематически определять наиболее вероятные структуры и комплексы, образующиеся в растворе, что важно для понимания механизмов ионного транспорта. Исследование ЛПЭ позволяет определить энергетические барьеры, которые необходимо преодолеть для миграции ионов, что связано с проводимостью электролита. Применение методов исследования ЛПЭ в сочетании с экспериментальными данными открывает новые возможности для рационального дизайна электролитных растворов с требуемыми физико-химическими свойствами.

Ключевые слова: электролитный раствор; молекулярное моделирование; молекулярная динамика; квантовая химия; ландшафт потенциальной энергии.

Для цитирования: Andreeva NA, Chaban VV. The role of potential energy landscape exploration in the development of new electrolyte solutions. *Journal of Advanced Materials and Technologies*. 2025;10(4):364-375. DOI: 10.17277/jamt-2025-10-04-364-375

1. Introduction

Due to the rapid growth of household appliances powered by the electrical grid, modern humanity is increasingly in need of additional and more efficient energy sources. This remark applies equally to both primary energy sources and rechargeable devices, among which portable electronics (phones, tablets, laptops) deserve special mention [1–4]. The concept of a potential energy landscape (PEL) is an imaginary multidimensional surface that describes the potential energy of a system depending on the internal coordinates of its components (Fig. 1). It is important to emphasize that, although the instantaneous potential energy of a system is a scalar quantity, the PEL is a multidimensional hypersurface, where the axes represent the coordinates of all particles, and the energy axis represents the corresponding potential energy value for each possible configuration. Thus, studying PEL allows us to analyze the dependence of a system's energy on its geometry, identifying stable states (minima on PEL) and the energy barriers between them, which determines the thermodynamics and kinetics of the processes being studied in electrolytes.

In the context of electrolyte solutions, PEL reflects the interactions between ions, solvent molecules, electrodes, technologically determined additives, and other system components. Systematic analysis of PEL provides valuable information on possible microscopic states of the solution, the mechanisms of solvation and ion transport during charging and discharging, and thermodynamic properties [5, 6]. PEL can use the potential energy of the system, the total energy of the system, or other thermodynamic potentials as energy, depending on the desired interpretation of the concept. Using the total energy of the system allows for the study of electrolyte systems under conditions of finite temperature and pressure.

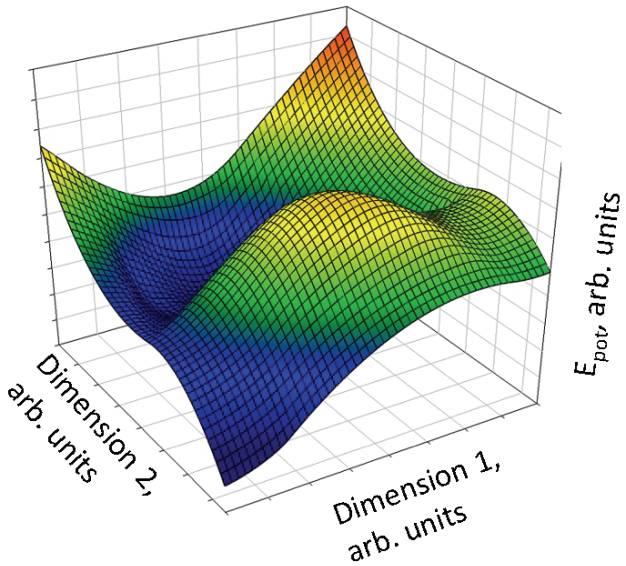

Fig. 1. Model PEL for a small section of an arbitrary electrolyte system

Currently, there is a rapid growth in research in the field of electrochemical devices such as lithium-ion batteries [7–9], sodium-ion batteries [10, 11], magnesium-ion batteries [12], solid-state batteries, fuel cells [13–15], supercapacitors [16–18], and electrolyzers [19–21]. This academic interest is driven by the steadily increasing need to produce efficient and sustainable energy storage and conversion systems [22–25]. In addition to local needs, electrochemical devices naturally play an important role in solving such global problems of civilization as climate change and depletion of fossil fuels. Electrolytes, acting as a medium for ion transport between electrodes, play a key role in the functioning efficiency and durability of these devices. Electrolytes directly affect the most important performance characteristics of electrochemical devices such as efficiency, power, cycle life, operating temperature range, and safety [26, 27]. A particular requirement of modern society is the environmental friendliness, or at least relative

environmental friendliness, of the batteries used. The cost of recycling a chemical power source must be included in the overall cost of energy technology developed in today's globalized world. Along with environmental friendliness, the issue of battery safety for the end user is important.

Currently existing electrolytes often do not fully meet the requirements of modern electrochemical devices [27]. For example, organic electrolytes, widely used in lithium-ion batteries, have limited ionic conductivity and proportionally high viscosity, a narrow electrochemical window, high flammability, and toxicity. Highly viscous electrolyte solutions create additional challenges in their development and production. It should be noted that viscosity is inversely proportional to ionic conductivity. The development of chemical power sources with reduced viscosity will automatically increase their electrical conductivity. Ionic conductivity is one of the most important characteristics of an electrolyte, and its high value makes this ion-molecular system technologically competitive [28]. The development of new electrolyte solutions with improved properties, such as high ionic conductivity, a wide electrochemical window, low viscosity, and high thermal and chemical stability, is a critical task for the creation of more efficient, safe, and durable electrochemical devices [28, 29]. Achieving this goal requires a deep understanding of the relationship between the composition, structure, and properties of electrolytes at the molecular level of organization.

Traditional experimental methods, such as measuring conductivity, viscosity, density, and electrochemical stability, provide valuable information on the macroscopic properties of electrolytes. However, they do not always provide a complete understanding of the molecular mechanisms underlying the observed phenomena. In recent years, PEL analysis has become a powerful tool for studying electrolyte solutions and rationally improving their performance. PEL analysis, based on molecular modeling methods such as quantum chemical calculations and classical molecular dynamics, provides detailed information on the interactions between solution components, i.e., ion-molecular and intermolecular electrostatic forces. The latter determine the equilibrium properties of the electrolyte solution [30–33].

Cations, anions, solvent molecules, and molecular additives influence the macroscopic properties of the electrolyte. For example, PEL studies can reveal preferred configurations of ion solvates, energy barriers for ion transport activation, and the influence of temperature and composition on the structure, transport, and macroscopic properties of the electrolyte [34–36].

In this paper, we present a critical review of recent applications of PEL studies based on classical and quantum chemical algorithms to analyze the structure, dynamics, and thermodynamic properties of electrolyte solutions [5, 22, 37, 38].

2. Results and Discussion

Calculations in theoretical chemistry and molecular physics are a powerful tool for studying PEL of electrolyte solutions. They enable modeling interactions between system components at the atomic level and obtaining detailed thermodynamic information about the structure and dynamics of the solution [39–42]. Subsequently, the thermodynamic characteristics of PEL can be translated into the language of electrochemical and physicochemical properties related to the experimentally obtained characteristics [5].

Numerical methods for calculating the potential energy of an ion-electron system from first principles, based on the fundamental laws of quantum mechanics, provide highly accurate results for parameterizing PEL. Unfortunately, they require significant computational resources and cannot be applied to systems of significant size due to the fundamental impossibility of obtaining the analytical solution to the wave equation for multielectron problems. The density functional theory (DFT) method is a less resource-intensive method that is widely used to calculate the electronic structure and properties of molecules, thermodynamic phases, and materials [7, 43–45]. The result of the DFT calculation of an electrolyte system is both the total potential energy and the forces acting on each atom, cation, or anion.

Classical molecular dynamics (MD) uses the classical laws of motion to model the motion of atoms and molecules [46, 47]. Classical MD does not consider electrons as individual interaction centers. Atoms interact with each other via simple potentials [48]. Potential functions are parameterized in advance based on quantum chemical or experimental data. During MD modeling, the potential energy of the system depends only on the distance between each two interacting centers at the current time. This method allows one to study the dynamics of the system and obtain information about its transport properties. For example, within the framework of classical MD modeling, there are methods for calculating the self-diffusion of solvent molecules and the conducting subsystem of the electrolyte, as

well as the ionic conductivity and viscosity of a multicomponent electrolyte system as a whole [46, 47, 49, 50].

Ab initio MD combines the principles of quantum mechanics and molecular dynamics, enabling the modeling of chemical reactions and other processes involving changes in electronic structure. An important practical advantage of Ab initio MD is its ability to correctly describe the effects of electron polarization and partial displacement of electron density without preliminary, labor-intensive parameterization of this physical process for different combinations of functional groups [10, 51]. Electronic polarization is an extremely common phenomenon in ion-molecular systems, capable of significantly affecting the structures of solvate complexes and the thermodynamics of the solvation process itself. The magnitude of electron polarization is directly proportional to the difference from zero of the formal charge of the participating cation or anion. While Ab initio MD is capable of producing more realistic simulation results, its cost is orders of magnitude higher than that of classical MD simulation. Therefore, Ab initio MD can only be used for isolated ion clusters and ionic solvates [10].

The Monte Carlo Metropolis method is an alternative to molecular dynamics for studying the motion of a system along PEL [52–55]. This method is used to generate system configurations corresponding to a given probability distribution. The system follows the direction belonging to PEL, which corresponds to a decrease in the potential energy of the system [56]. Unlike MD, the evolution of the system does not require the calculation of energy gradients (forces acting on atoms) and does not use a time step for integrating the equations of motion. The predominant area of application of the method turned out to be equilibrium physicochemical systems [39, 53, 56–59]. Consequently, the most natural application of the Monte Carlo Metropolis method seems to be the possibility of studying thermodynamic properties and phase transitions [6, 60–61].

The kinetic energy injection method allows one to purposefully search for low-energy stationary points by periodic kinetic excitation of the system under study [12, 62, 63]. This method combines equilibrium semi-empirical MD with a stochastic component. While MD modeling progressively leads the system to its minimum potential energies, artificially introduced excitation allows one to avoid lingering in local potential valleys. Thus, the system quickly finds itself in realistic microscopic ion-molecular configurations regardless of the energy of an arbitrarily chosen initial state. It is worth noting that a certain modification of particle momenta does not lead to the formation of unphysical ion-molecular configurations, but at the same time changes the current phase trajectory of the system [10, 64–66]. Thus, kinetic energy injection, compared to the standard MD method, allows the system to visit a larger number of microscopic states of its own phase space (Fig. 2).

Experimental research methods provide important information on the structure and dynamics of electrolyte solutions, which can be used to validate and refine theoretical models. X-ray diffraction allows one to determine the spatial arrangement of atoms and molecules in solution [68]. Neutron diffraction is sensitive to light atoms such as hydrogen, making it useful for investigating the structure of solvents [38]. Nuclear magnetic resonance spectroscopy provides information on the local structure and dynamics of molecules in solution [69]. Raman spectroscopy is used to study the vibrational modes of molecules and obtain information on intermolecular interactions. Electrochemical methods such as cyclic voltammetry, impedance spectroscopy, and others allow one to study the electrochemical properties of solutions and the kinetics of electrode reactions [66].

PEL has a fundamental influence on various properties of electrolyte solutions, which determine their effectiveness in various applications. Ionic conductivity is a key parameter of electrolytes, determining the efficiency of charge transfer in electrochemical devices. PEL influences ionic conductivity in the following ways. PEL determines

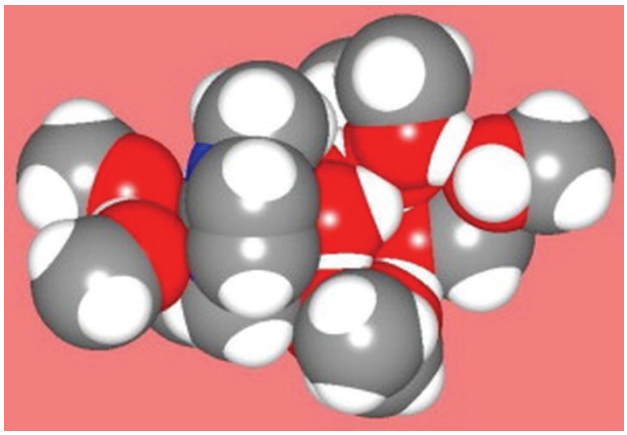

Fig. 2. Solvation shell of the imidazolium cation in a mixture of water and methanol. Reproduced from the author's source [67] with permission from Elsevier. Copyright Elsevier (2024)

the energy barriers that ions must overcome to move in solution. The lower the activation energy, the higher the ionic mobility and, consequently, the conductivity of the electrolyte solution. PEL reflects the coordination of ions by the solvent, which in turn affects their mobility. PEL contains information about the strength of interactions between ions and the formation of ion pairs. The combination of cations and anions in an electrolyte solution is considered undesirable in the context of practical applications, as it leads to a decrease in ionic conductivity. Electrolyte development involves selecting optimal concentrations of all its components to minimize the formation of ionic aggregates. The dependence of ionic conductivity on the mole fraction of ions in the electrolyte contains a maximum corresponding to the desired properties of the system (Fig. 3).

The electrochemical stability of an electrolyte determines its ability to resist decomposition at high voltages, which is critical for the operation of batteries and other devices [71]. The shape of certain PEL regions and specific energy differences in the system describe electrochemical stability. In particular, PEL determines the energy required to decompose solvent molecules or other electrolyte components. Interactions with electrodes can also be reflected in PEL if they were included in the model system during the theoretical study of the landscape. PEL determines the energy of interaction between the electrolyte and the electrodes and provides an estimate of the possibility of the formation of passivation layers or the occurrence of other undesirable reactions [72].

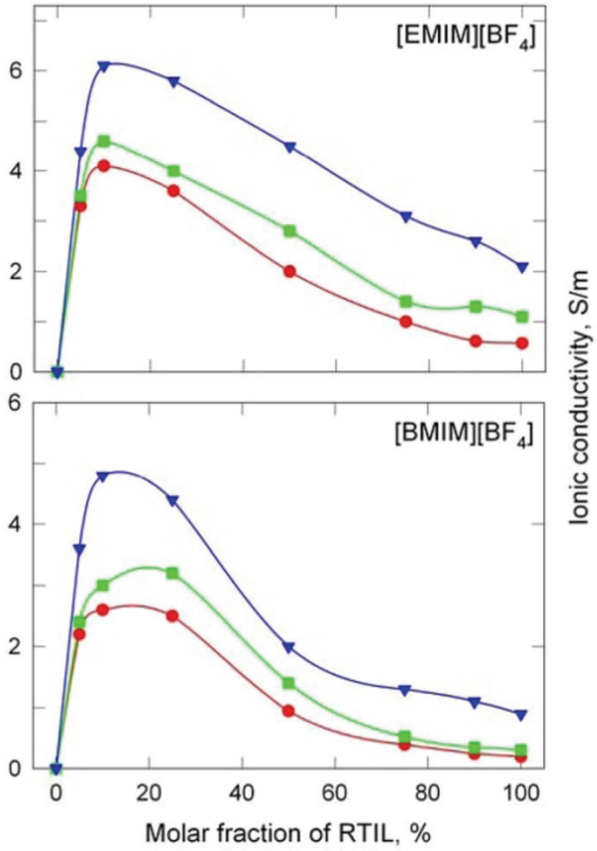

Fig. 3. Calculated maximum conductivity in mixtures of ionic liquids, [EMIM][BF4] and [BMIM][BF4], with acetonitrile at 283 K (red circles), 298 K (green squares), and 323 K (blue triangles). Reproduced from the author's source [70] with permission from the American Chemical Society. Copyright ACS (2024)

Electrolyte viscosity affects the transport properties and the operating efficiency of electrochemical devices [73, 74]. Viscosity is associated with energy gradients observed in PEL. Intermolecular interactions that determine PEL characterize the strength of interactions between solvent molecules and ions, which affects the viscosity of the solution.

PEL reflects the possible microscopic states of the electrolyte solution at different temperatures and pressures. The structure of an electrolyte solution, among other things, implies the formation of clusters or other ordered structures, which can also dramatically affect viscosity.

Therefore, information on PEL can be used for the rational design of new electrolyte solutions with improved characteristics. PEL analysis enables the selection of the most suitable solvent that ensures optimal ion solvation and minimal activation energy for ion transport. PEL allows for the quantitative assessment of the strength of interactions between ions and the selection of a salt that minimizes ion association and ensures high ionic conductivity. PEL also allows for the study of the influence of additives on the structure and properties of an electrolyte, such as viscosity, electrochemical stability, and electrode wettability [75].

For the past two decades, ionic liquids have been considered a promising basis for liquid electrolyte systems. The low volatility of these compounds eliminates electrolyte loss at any stage of production and operation of a chemical power source. Some ionic liquids exhibit only minor toxicity to humans and animals or are generally considered harmless. The wide range of liquid states, especially at low temperatures, opens up new frontiers for the application of such electrolytes. Because ionic liquids do not contain molecules, their use as electrolytes enables previously unheard-of concentrations of cations and anions in the system. However, a current problem is the high viscosity and, consequently, the

mediocre electrical conductivity of these chemical compounds. To stimulate ion transport in electrolytes, optimal mixtures of ionic and molecular liquids are being developed, for example, those containing acetonitrile, methanol, or propylene carbonate [76]. PEL enables the study of the structure and properties of ionic liquids, as well as the above-described mixtures, which remain promising electrolytes for various electrochemical applications [70].

Beyond the scope of electrolyte solutions, the versatility of PEL as a source of information on a wide range of chemical and physicochemical properties of a prototype system should be noted. Similar to the cases described above, studying PEL allows us to investigate the mechanisms of ion transport in solid and polymer electrolytes and develop new materials with higher ionic conductivity. This goal can potentially be achieved by suppressing undesirable atom-atom interactions. Naturally, such modification of the electrolyte system also requires synthetic efforts on the part of the electrochemical laboratory.

Ion migration in liquid electrolyte solutions is a complex physical process that requires overcoming certain energy barriers. These barriers arise from the interaction of the migrating ion with surrounding atoms or molecules. For ion migration in an electrolyte, several significant energy barriers of varying heights must be overcome. The specific values of the activation barriers within ion transport depend on the nature of the solvent and the electrostatic charge of the ion. For example, it is well known that the solvation of cations in the vast majority of cases is described by higher potential energies than the solvation of anions [77].

Using PEL, it is possible to calculate the activation energy for an ion to leave its solvation shell. Ions in an electrolyte are surrounded by solvent molecules, forming a solvation shell. For an ion to begin moving, it must break these bonds, which requires energy. Next, it must overcome an energy barrier to move the ion through the electrolyte. Ion movement in the electrolyte is hindered by interactions with other ions and solvent molecules. The ion must overcome electrostatic attraction and repulsion forces, as well as van der Waals forces. An energy barrier also accompanies the ion's entry into its new solvation shell. When the ion reaches its destination, it must form new bonds with solvent molecules to create a new solvation shell. A correctly calculated PEL contains complete thermodynamic information characterizing the processes described above [78].

The following factors influence the heights of energy barriers. The type of solvent and solutes initially determines the energy barriers. For example, solvent viscosity affects the energy required for ion movement. The higher the ion concentration, the stronger the interaction between them, which increases energy barriers. Increasing temperature increases the kinetic energy of ions, which helps them overcome energy barriers. An external electric field can lower the energy barriers to ion movement in a given direction.

The magnitude of the energy barriers in PEL at the microscopic level determines the macroscopic characteristics of the electrolyte. The lower the energy barriers, the higher the ion mobility and, consequently, the ionic conductivity of the electrolyte. Energy barriers affect the rate of ion diffusion in the electrolyte and the dynamics of charging and discharging [78]. Understanding the energy barriers to ion migration is key to the development of new electrolytes with improved characteristics, for example, for use in batteries, fuel cells, and other electrochemical devices.

PEL allows for the modeling of processes occurring in batteries [79], such as ion intercalation, the formation of passivation layers, and electrolyte degradation. Furthermore, PEL enables the modeling of charge and mass transfer processes in fuel cells and the optimization of their design. Finally, PEL enables the modeling of charge storage processes in supercapacitors and the development of new high-capacity materials [78].

Research into PEL has enabled the development of new electrolytes with high ionic conductivity and electrochemical stability, leading to batteries with increased efficiency, capacity, reduced production costs, and extended service life. Similar research into supercapacitors has enabled the increase of their capacity and charging rates [80, 81].

Lithium-sulfur batteries have a high theoretical capacity, but their practical application is limited by several issues, such as the dissolution of lithium polysulfides and the low electrical conductivity of sulfur. Research into PEL allows us to understand the mechanisms of these processes and develop electrolytes that minimize polysulfide dissolution and increase sulfur conductivity. For example, the use of electrolytes with a high salt content or the addition of special additives can significantly improve the performance of lithium-sulfur batteries [82]. Sodium-ion batteries are considered a promising alternative to lithium-ion batteries due to their lower cost and greater availability of sodium. However, sodium ions are larger in size and mass than lithium ions, resulting

in reduced ionic conductivity and deterioration of electrode reaction kinetics. Studying PEL allows for optimization of electrolyte compositions for sodium-ion batteries, for example, by selecting solvents with high permittivity and low viscosity, as well as by adding salts with high solubility and low activation energy for sodium ion transport [10, 51]. Modeling PEL allows for inclusion of the electrode in the analysis and an energetic description of the electrolyte behavior in a charged device (Fig. 4).

Studying the influence of temperature and pressure on PEL helps understand how electrolyte properties change under various operating conditions. Taking into account the shape of PEL in an applied electric field allows us to understand charge transfer mechanisms in electrolytes and optimize the operation of electrochemical devices [83]. Electrolyte–electrode surface interactions are important for understanding the mechanisms of electrode reactions. Thus, it is possible to propose new, improved materials with improved electrochemical properties.

The development of theoretical methods for studying PEL opens new possibilities for the development of electrolyte solutions with improved characteristics [84–85]. A comparative analysis of modern approaches (Table 1) demonstrates their complementarity.

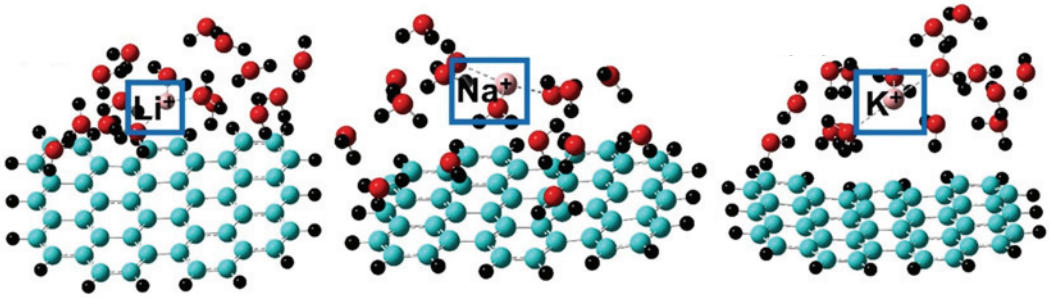

Fig. 4. Low-energy ion-molecular configurations of lithium, sodium, and potassium ions on the surface of a negatively charged graphene electrode. Dashed lines indicate the water molecules closest to the ions. Reproduced from the author's source [51] with permission from Elsevier. Copyright Elsevier (2024)

Table 1. Comparative assessment of the methods for studying PEL presented in this paper and their application

Method	Essence of the method	Potential opportunities	Disadvantages
Quantum-chemical calculations (DFT) [7, 12, 43-45]	Solution of quantum mechanical equations to calculate the electronic structure and total energy of a system	High accuracy, study of chemical reactions, bond breaking / formation, electron polarization, parametrization of force fields for classical methods	Extremely high computational costs. Inapplicable to large systems (>1000 atoms) and long processes
Classical Molecular Dynamics (MD) [22, 46-47, 49]	Simulation of atomic motion based on classical Newton's laws using predefined force fields	Simulation of large systems (millions of atoms) over nanoseconds and microseconds. Calculation of transport properties: ionic conductivity, viscosity, and self-diffusion coefficients	Accuracy depends entirely on the quality of the force field parameterization. It does not take into account chemical reactions or electron polarization (without special polarizable fields)
Ab initio molecular dynamics (AIMD) [10, 23, 51]	A combination of quantum chemical calculations (usually DFT) and molecular dynamics. Forces are calculated on the fly from first principles	The most accurate modeling, taking into account the electronic structure. Correct description of reactions, polarization, and charge transfer. It does not require parameterization of force fields	The most resource-intensive method. Limited to very small systems (hundreds of atoms) and picosecond time scales

Continued Table 1

Method	Essence of the method	Potential opportunities	Disadvantages
Monte Carlo (Metropolis) Method [6, 52–55]	A stochastic method for generating system configurations according to a given distribution (e.g., canonical NVT)	Efficient calculation of equilibrium thermodynamic properties (free energies, phase diagrams). It does not require calculation of forces (energy gradients)	It does not provide information on the dynamics and kinetics of processes (no concept of time). Not applicable for direct calculation of transport properties
Kinetic Energy Injection Method [12, 62, 63]	A modification of MD in which the system periodically receives kinetic excitation to escape from local PEL minima	It effectively searches for the global energy minimum and low-energy configurations. It allows one to avoid "stuckness" and more fully explore the phase space	It introduces a non-physical stochastic element. It requires careful selection of injection parameters to avoid artifacts and non-physical states
Experimental methods (for validation) [38, 66, 69]	X-ray and neutron diffraction, NMR, Raman spectroscopy, and electrochemical methods	Provide direct data on the structure, dynamics, and macroscopic properties of real systems. Critically important for testing and refining theoretical models	They provide averaged information, often without atomic detail. They do not allow one to directly "see" PEL, but only its consequences

Advances in methods for calculating the potential energy of a system can enable the study of electrolyte systems with more complex compositions and provide more information about PEL. The combination of theoretical calculations and experimental data will provide a more symbiotic understanding of PEL and use this information for the rational design of new electrolytes. Finally, the application of machine learning methods to PEL analysis will accelerate the development of new electrolytes and optimize their properties [83].

3. Conclusion

This paper analyzed a significant number of the most recent literature sources, covering both comprehensive studies of electrolyte solutions using molecular modeling methods to describe PEL, and auxiliary computer calculations to confirm experimental results.

Based on this critical analysis, we believe it is appropriate to draw the following conclusions. Studying PEL is a powerful tool for analyzing and predicting the properties of electrolyte solutions. The use of research methods based on classical and quantum chemical approaches allows us to obtain unique physical information. First, it seems possible to study in detail the intermolecular and ion-molecular interactions that determine the macroscopic properties of an electrolyte solution. Ionic conductivity, viscosity, and density can be calculated using analytical relationships based on statistical processing of the system's phase trajectory. Second, it is easy to identify stable configurations of ions and solvates that influence the equilibrium state of the electrolyte and the mechanisms of ion transport within it. Third, the resulting thermodynamic properties of the simulated system and the energies of paired ion-molecule interactions allow us to estimate barriers to ion migration, which is directly related to electrolyte conductivity.

Thus, the combination of PEL research methods with experimental data opens new prospects for the targeted design of electrolyte solutions with specified characteristics, which is crucial for the development of highly efficient electrochemical devices.

4. Acknowledgement

V.V. Chaban is a visiting professor and international consultant at Yerevan State University.

5. Conflict of interest

The authors declare no conflict of interest.

References

1. Zittlau P, Mross S, Gond D, Kohns M. Molecular modeling and simulation of organic electrolyte solutions for lithium ion batteries. *The Journal of Chemical Physics*. 2024;161(12):124118. DOI:10.1063/5.0228158

2. Shi N, Wang G, Mu T, Li H, et al. Long side-chain imidazolium functionalized poly(vinyl chloride)

membranes with low cost and high performance for vanadium redox flow batteries. *Journal of Molecular Liquids*. 2023;376:121401. DOI:10.1016/j.molliq.2023.121401

3. Deb D, Bhattacharya S. Imidazolium-based ionanofluid electrolytes with viscosity decoupled ion transport properties for lithium-ion batteries. *Journal of Molecular Liquids*. 2023;379:121645. DOI:10.1016/j.molliq.2023.121645

4. Wu Z, Tian Y, Chen H, Wang L, et al. Evolving aprotic Li–air batteries. *Chemical Society Reviews*. 2022;51(18):8045-8101. DOI:10.1039/D2CS00003B

5. Habibi P, Polat HM, Blazquez S, Vega C, et al. Accurate free energies of aqueous electrolyte solutions from molecular simulations with non-polarizable force fields. *The Journal of Physical Chemistry Letters*. 2024;15(16):4477-4485. DOI:10.1021/acs.jpclett.4c00428

6. Lu GW, Li CX, Wang WC, Wang ZH. A Monte-Carlo simulation on structure and thermodynamics of potassium nitrate electrolyte solution. *Molecular Physics*. 2005;103(5):599-610. DOI:10.1080/00268970410001683834

7. Parida R, Yong Lee J. Boron based podand molecule as an anion receptor additive in Li-ion battery electrolytes: a combined density functional theory and molecular dynamics study. *Journal of Molecular Liquids*. 2023;384:122236. DOI:10.1016/j.molliq.2023.122236

8. Kartha TR, Mallik BS. Revisiting $LiClO_4$ as an electrolyte for Li-ion battery: effect of aggregation behavior on ion-pairing dynamics and conductance. *Journal of Molecular Liquids*. 2020;302:112536. DOI:10.1016/j.molliq.2020.112536

9. Jiang H, Zhang Q, Zhang Y, Sui L, et al. Li-ion solvation in propylene carbonate electrolytes determined by molecular rotational measurements. *Physical Chemistry Chemical Physics*. 2019;21(20):10417-10422. DOI:10.1039/C8CP07552B

10. Chaban VV, Andreeva NA. Shorter-chained trialkylsulfonium cations are preferable as admixtures to lithium-ion and sodium-ion electrolytes in acetonitrile. *Journal of Molecular Liquids*. 2023;385:122399. DOI:10.1016/j.molliq.2023.122399

11. Haghani H, Behrouz M, Chaban VV. Triethylsulfonium-based ionic liquids enforce lithium salt electrolytes. *Physical Chemistry Chemical Physics*. 2022;24(16):9418-9431. DOI:10.1039/D2CP00275B

12. Chaban VV, Andreeva NA. Magnesium-based electrolytes with ionic liquids chloride additives: quantum chemical stationary point analysis. *Journal of Molecular Liquids*. 2024;402:124804. DOI:10.1016/j.molliq.2024.124804

13. Zhang W, Hu YH. Material design and performance of carbon monoxide-fueled solid oxide fuel cells: a review. *Energy Science & Engineering*. 2023;11(9):3276-3288. DOI:10.1002/ese3.1502

14. Dethan JFN, Swamy V. Mechanical and thermal properties of carbon nanotubes and boron nitride nanotubes for fuel cells and hydrogen storage applications: a comparative review of molecular dynamics studies. *International Journal of Hydrogen Energy*. 2022;47(59):24916-24944. DOI:10.1016/j.ijhydene.2022.05.240

15. Pant R, Sengupta S, Lyulin AV, Venkatnathan A. Computational investigation of a protic ionic liquid doped poly-benzimidazole fuel cell electrolyte. *Journal of Molecular Liquids*. 2020;314:113686. DOI:10.1016/j.molliq.2020.113686

16. Khan HA, Tawalbeh M, Aljawrneh B, Abuwatfa W, et al. A comprehensive review on supercapacitors: their promise to flexibility, high temperature, materials, design, and challenges. *Energy*. 2024;295:131043. DOI:10.1016/j.energy.2024.131043

17. Varner S, Wang ZG. Effects of dilution in ionic liquid supercapacitors. *Physical Chemistry Chemical Physics*. 2022;24(44):27362-27374. DOI:10.1039/D2CP03398D

18. Dashti Najafi M, Kowsari E, Reza Naderi H, Sarabadani Tafreshi S, et al. High-performance symmetric supercapacitor based on new functionalized graphene oxide composites with pyrimidine nucleotide and nucleoside. *Journal of Molecular Liquids*. 2022;348:118381. DOI:10.1016/j.molliq.2021.118381

19. Bakhshandeh A, Dos Santos AP, Levin Y. Efficient simulation method for nano-patterned charged surfaces in an electrolyte solution. *Soft Matter*. 2018;14(20):4081-4086. DOI:10.1039/C8SM00226F

20. Brkljača Z, Namjesnik D, Lützenkirchen J, Předota M, et al. Quartz/aqueous electrolyte solution interface: molecular dynamic simulation and interfacial potential measurements. *The Journal of Physical Chemistry C*. 2018;122(42):24025-24036. DOI:10.1021/acs.jpcc.8b04035

21. Di Tommaso D, Prakash M, Lemaire T, Lewerenz M, et al. Molecular dynamics simulations of hydroxyapatite nanopores in contact with electrolyte solutions: the effect of nanoconfinement and solvated ions on the surface reactivity and the structural, dynamical, and vibrational properties of water. *Crystals*. 2017;7(2):57. DOI:10.3390/cryst7020057

22. Karatrantos AV, Middendorf M, Nosov DR, Cai Q, et al. Diffusion and structure of propylene carbonate–metal salt electrolyte solutions for post-lithium-ion batteries: from experiment to simulation. *The Journal of Chemical Physics*. 2024;161(5):054502. DOI:10.1063/5.0216222

23. Eisenhart AE, Beck TL. Quantum simulations of hydrogen bonding effects in glycerol carbonate electrolyte solutions. *The Journal of Physical Chemistry B*. 2021;125(8):2157-2166. DOI:10.1021/acs.jpcb.0c10942

24. Friedman R. Simulations of biomolecules in electrolyte solutions. *Advanced Theory and Simulations*. 2019;2(4):1800163. DOI:10.1002/adts.201800163

25. Chaiyasit P, Tongraar A, Kerdcharoen T. Characteristics of methylammonium ion ($CH_3NH_3^+$) in aqueous electrolyte solution: an ONIOM-XS md simulation study. *Chemical Physics*. 2017;493:91-101. DOI:10.1016/j.chemphys.2017.06.012

26. Li Y, Wu F, Li Y, Liu M, et al. Ether-based electrolytes for sodium ion batteries. *Chemical Society Reviews*. 2022;51(11):4484-4536. DOI:10.1039/D1CS00948F

27. Yang Q, Zhang Z, Sun XG, Hu YS, et al. Ionic liquids and derived materials for lithium and sodium batteries. *Chemical Society Reviews*. 2018;47(6):2020-2064. DOI:10.1039/C7CS00464H

28. Yang L, Huang K. Electric conductivity in electrolyte solution under external electromagnetic field by nonequilibrium molecular dynamics simulation. *The Journal of Physical Chemistry B*. 2010;114(25):8449-8452. DOI:10.1021/jp102593m

29. Kumar P, Yashonath S. Ionic conductivity in aqueous electrolyte solutions: insights from computer simulations. *Journal of Molecular Liquids*. 2019;277:506-515. DOI:10.1016/j.molliq.2018.12.090

30. Liu Y, Zhu W, Li B, Yang L. Simulation study on the flow behaviors of weak electrolyte solutions in nano-sized and micron-sized pores considering electric double layer interactions. *Energy Sources, Part A: Recovery, Utilization, and Environmental Effects*. 2022;44(2):3532-3543. DOI:10.1080/15567036.2022.2067266

31. Guàrdia E, Martí J, Padró JA. Ion solvation in aqueous supercritical electrolyte solutions at finite concentrations: a computer simulation study. *Theoretical Chemistry Accounts*. 2006;115(2-3):161-169. DOI:10.1007/s00214-005-0055-3

32. Balbuena PB, Johnston KP, Rossky PJ. Molecular dynamics simulation of electrolyte solutions in ambient and supercritical water. 1. Ion solvation. *The Journal of Physical Chemistry*. 1996;100(7):2706-2715. DOI:10.1021/jp952194o

33. Bosen A, Roth M. Simulation of a distillation column on an IBM PC, accounting for real behaviour of electrolyte solutions. *Chemical Engineering & Technology*. 1991;14(5):295-300. DOI:10.1002/ceat.270140502

34. Neria E, Nitzan A. Numerical simulations of solvation dynamics in electrolyte solutions. *The Journal of Chemical Physics*. 1994;100(5):3855-3868. DOI:10.1063/1.466374

35. Padró JA, Trullàs J, Giró A. Langevin dynamics simulations of electrolyte solutions. Influence of friction and random forces. *Journal of the Chemical Society, Faraday Transactions.* 1990;86(12):2139-2143. DOI:10.1039/FT9908602139

36. Spohr E, Heinzinger K. Computer simulations of water and aqueous electrolyte solutions at interfaces. *Electrochimica Acta*. 1988;33(9):1211-1222. DOI:10.1016/0013-4686(88)80151-8

37. Feng HJ, Zhou J, Lu XH. Molecular dynamics simulations on the interfacial structures of electrolyte solutions. *Acta Chimica Sinica.* 2009;67(21):2407-2412.

38. Neilson GW. The structure of aqueous electrolyte solutions: comparison of computer simulation and experiment. *Zeitschrift für Naturforschung A*. 1991;46(1-2):100-106. DOI:10.1515/zna-1991-1-216

39. Lee LL, Llano-Restrepo M, Chapman WG, Shukla KP. Improved MSA theory for concentrated electrolyte solutions based on Monte-Carlo simulation at high ionic strengths. *Journal of the Chinese Institute of Chemical Engineers*. 1996;27(4).

40. Malekzadeh Moghani M, Khomami B. Flexible polyelectrolyte chain in a strong electrolyte solution: insight into equilibrium properties and force-extension behavior from mesoscale simulation. *The Journal of Chemical Physics*. 2016;144(2):024903. DOI:10.1063/1.4939720

41. Kohns M, Reiser S, Horsch M, Hasse H. Solvent activity in electrolyte solutions from molecular simulation of the osmotic pressure. *The Journal of Chemical Physics*. 2016;144(8):084112. DOI:10.1063/1.4942500

42. Yi L, Liang D, Zhou X, Li D, et al. Molecular dynamics simulations of carbon dioxide hydrate growth in electrolyte solutions of NaCl and $MgCl_2$. *Molecular Physics*. 2014;112(24):3127-3137. DOI:10.1080/00268976.2014.932454

43. Fiates J, Ratochinski RH, Lourenço TC, Da Silva JLF, et al. Fluoroalkoxyaluminate-based ionic liquids as electrolytes for sodium-ion batteries. *Journal of Molecular Liquids*. 2023;369:120919. DOI:10.1016/j.molliq.2022.120919

44. Xu X, Su L, Lu F, Yin Z, et al. Unraveling anion effect on lithium ion dynamics and interactions in concentrated ionic liquid electrolyte. *Journal of Molecular Liquids*. 2022;361:119629. DOI:10.1016/j.molliq.2022.119629

45. Khudozhitkov AE, Stange P, Stepanov AG, Kolokolov DI, et al. Structure, hydrogen bond dynamics and phase transition in a model ionic liquid electrolyte. *Physical Chemistry Chemical Physics*. 2022;24(10):6064-6071. DOI:10.1039/D2CP00452F

46. Calero C, Faraudo J, Aguilella-Arzo M. Molecular dynamics simulations of concentrated aqueous electrolyte solutions. *Molecular Simulation*. 2011;37(2):123-134. DOI:10.1080/08927022.2010.525513

47. Murad S, Oder K, Lin J. Molecular simulation of osmosis, reverse osmosis, and electro-osmosis in aqueous and methanolic electrolyte solutions. *Molecular Physics*. 1998;95(3):401-408. DOI:10.1080/00268979809483173

48. Berendsen HJC, van der Spoel D, van Drunen R. GROMACS - A message-passing parallel molecular-dynamics implementation. *Computer Physics Communication.* 1995;91:43-56.

49. Lu G wu, Li Y feng, Sun W, Li C. Molecular dynamics simulation of hydration structure of KNO_3 electrolyte solution. *Chinese Journal of Chemical Physics*. 2007;20(1):22-30. DOI:10.1360/cjcp2007.20(1).22.9

50. Kerisit S, Ilton ES, Parker SC. Molecular dynamics simulations of electrolyte solutions at the (100) goethite surface. *The Journal of Physical Chemistry B*. 2006;110(41):20491-20501. DOI:10.1021/jp0636569

51. Chaban VV, Andreeva NA. Aqueous electrolytes at the charged graphene Surface: Electrode-Electrolyte coupling. *Journal of Molecular Liquids*. 2023;387:122724.

52. Izarra AD, Coudert FX, Fuchs AH, Boutin A. Alchemical Osmo stat for Monte-Carlo simulation: sampling aqueous electrolyte solution in open systems. *The Journal of Physical Chemistry B*. 2023;127(3):766-776. DOI:10.1021/acs.jpcb.2c07902

53. Theiss M, Gross J. Nonprimitive model electrolyte solutions: comprehensive data from Monte-Carlo simulations. *Journal of Chemical & Engineering Data*. 2020;65(2):634-639. DOI:10.1021/acs.jced.9b00855

54. Ozaki H, Kuratani K, Kiyobayashi T. Monte-Carlo simulation of the ionic transport of electrolyte solutions at high concentrations based on the pseudo-lattice model. *Journal of The Electrochemical Society*. 2016;163(7):H576-H583. DOI:10.1149/2.0941607jes

55. Van Megen W, Snook I, Vincent B. Monte-Carlo simulation of small particle adsorption at the solid/electrolyte solution interface. *Journal of Colloid and Interface Science*. 1983;92(1):262-264. DOI:10.1016/0021-9797(83)90136-4

56. Lukšič M, Hribar-Lee B, Tochimani SB, Pizio O. Solvent primitive model for electrolyte solutions in disordered porous matrices of charged species. Replica Ornstein-Zernike theory and grand canonical monte Carlo simulations. *Molecular Physics*. 2012;110(1):17-30. DOI:10.1080/00268976.2011.631057

57. Jönsson M, Skepö M, Linse P. Monte-Carlo simulations of the hydrophobic effect in aqueous electrolyte solutions. *The Journal of Physical Chemistry B*. 2006;110(17):8782-8788. DOI:10.1021/jp0604241

58. Sørensen TS, Sloth P. Ion and potential distributions in charged and non-charged primitive spherical pores in equilibrium with primitive electrolyte solution calculated by grand canonical ensemble Monte-Carlo simulation. Comparison with generalized Debye–Hückel and Donnan theory. *Journal of the Chemical Society, Faraday Transactions.* 1992;88(4):571-589. DOI:10.1039/FT9928800571

59. Svensson B, Jönsson B. The interaction between charged aggregates in electrolyte solution. A Monte-Carlo simulation study. *Chemical Physics Letters*. 1984;108(6):580-584. DOI:10.1016/0009-2614(84)85058-7

60. Truzzolillo D, Bordi F, Sciortino F, Sennato S. Interaction between like-charged polyelectrolyte-colloid complexes in electrolyte solutions: a Monte-Carlo simulation study in the Debye–Hückel approximation. *The Journal of Chemical Physics*. 2010;133(2):024901. DOI:10.1063/1.3459125

61. Li CX, Tian R, Lu GW, Wang ZH, Wang WC. Monte-Carlo simulation on model fluid of electrolyte solution. *Acta Physico-Chimica Sinica*. 2003;61(2):175-180.

62. Bedair MA, Abuelela AM, Melhi S, Yousif QA, et al. Highly effective inhibition of steel corrosion in 1.0 M HCl solution using a novel non-ionic surfactant with coumarin moiety: Practical and computational studies. *Materials Chemistry and Physics*. 2024;312:128644.

63. Duczinski R, Polesso BB, Duarte E, Bernard FL, et al. Separation of Co_2/N_2 mixtures by new il/acrylic polymer microcapsules designed by a one-step suspension-based polymerization encapsulation process. *Journal of Molecular Liquids*. 2023;385:122394. DOI:10.1016/j.molliq.2023.122394

64. Chaban VV, Andreeva NA. Mutual miscibility of diethyl sulfoxide and acetonitrile: fundamental origin. *Journal of Molecular Liquids*. 2022;349:118110. DOI:10.1016/j.molliq.2021.118110

65. Chaban VV, Andreeva NA. Mixtures of diethyl sulfoxide and methanol: structure and thermodynamics. *Journal of Solution Chemistry*. 2022;51(7):788-801. DOI:10.1007/s10953-022-01167-x

66. Jones FGE, Dryfe RAW. Hydrodynamic voltammetry at the interface between immiscible electrolyte solutions: numerical simulation of the voltammetric response. *Journal of Electroanalytical Chemistry*. 2008;615(1):25-33. DOI:10.1016/j.jelechem.2007.11.021

67. Chaban V. Competitive solvation of the imidazolium cation by water and methanol. *Chemical Physics Letters*. 2015;623:76-81. DOI:10.1016/j.cplett.2015.01.051

68. Ohba T, Hata K, Chaban VV. Nanocrystallization of imidazolium ionic liquid in carbon nanotubes. *The Journal of Physical Chemistry C*. 2015;119(51):28424-28429. DOI:10.1021/acs.jpcc.5b09423

69. Chizhik VI, Egorov AV, Komolkin AV, Vorontsova AA. Microstructure and dynamics of electrolyte solutions containing polyatomic ions by NMR relaxation and molecular dynamics simulation. *Journal of Molecular Liquids*. 2002;98-99:173-182. DOI:10.1016/S0167-7322(01)00306-3

70. Chaban VV, Voroshylova IV, Kalugin ON, Prezhdo OV. Acetonitrile boosts conductivity of imidazolium ionic liquids. *The Journal of Physical Chemistry B*. 2012;116(26):7719-7727. DOI:10.1021/jp3034825

71. Thakur RC, Sharma A, Sharma R, Kaur H. A comparative analysis of volumetric, viscometric and conductometric properties of triethylmethylammonium tetrafluoroborate ($TEMABF_4$) and tetraethylammonium tetrafluoroborate ($TEABF_4$) in pure propylene carbonate (PC) and binary aqueous propylene carbonate solvents. *Journal of Molecular Liquids*. 2023;374:121244. DOI:10.1016/j.molliq.2023.121244

72. Piatti E, Guglielmero L, Tofani G, Mezzetta A, et al. Ionic liquids for electrochemical applications: correlation between molecular structure and electrochemical stability window. *Journal of Molecular Liquids*. 2022;364:120001. DOI:10.1016/j.molliq.2022.120001

73. Dočkal J, Mimrová P, Lísal M, Moučka F. Structure of aqueous alkali metal halide electrolyte solutions from molecular simulations of phase-transferable polarizable models. *Journal of Molecular Liquids*. 2024;394:123797. DOI:10.1016/j.molliq.2023.123797

74. Panagiotopoulos AZ. Simulations of activities, solubilities, transport properties, and nucleation rates for aqueous electrolyte solutions. *The Journal of Chemical Physics*. 2020;153(1):010903. DOI:10.1063/5.0012102

75. Maftoon-Azad L. Electrochemical stability windows of Ali-cyclic ionic liquids as lithium metal battery electrolytes: a computational approach. *Journal of*

Molecular Liquids. 2021;343:117589. DOI:10.1016/j.molliq.2021.117589

76. Chaban VV, Prezhdo OV. Ionic and molecular liquids: working together for robust engineering. *The Journal of Physical Chemistry Letters*. 2013;4(9):1423-1431. DOI:10.1021/jz400113y

77. Bdey S, Boussadoune N, Allard F, Huot J, et al. Synthesis, structural study, and Na^+ migration pathways simulation of the new phase $Na_3Al_3(AsO_4)_4$. *Journal of Solid State Chemistry*. 2024;330:124459. DOI:10.1016/j.jssc.2023.124459

78. Colherinhas G, Fileti EE, Chaban VV. Can inorganic salts tune electronic properties of graphene quantum dots? *Physical Chemistry Chemical Physics*. 2015;17(26):17413-17420. DOI:10.1039/C5CP02083B

79. Yun Y, Wu S, Wang D, Luo X, et al. Molecular dynamics simulations in semiconductor material processing: a comprehensive review. *Measurement*. 2025;241:115708. DOI:10.1016/j.measurement.2024.115708

80. De Araujo Chagas H, Fileti EE, Colherinhas G. Comparing supercapacitors with graphene/graphyne electrodes and [Bmim][PF_6], [Emim][BF_4], [Ch][Gly] and [Pyr][Tfsi] ionic liquids using molecular dynamics. *Journal of Molecular Liquids*. 2023;379:121703. DOI:10.1016/j.molliq.2023.121703

81. Messias A, Fileti EE. Assessing the impact of valence asymmetry in ionic solutions and its consequences on the performance of supercapacitors. *Physical Chemistry Chemical Physics*. 2022;24(34):20445-20453. DOI:10.1039/D2CP00348A

82. Brieske DM, Warnecke A, Sauer DU. Modeling the volumetric expansion of the lithium-sulfur battery considering charge and discharge profiles. *Energy Storage Materials*. 2023;55:289-300. DOI:10.1016/j.ensm.2022.11.053

83. Zhang J, Pagotto J, Duignan TT. Towards predictive design of electrolyte solutions by accelerating *ab initio* simulation with neural networks. *Journal of Materials Chemistry A*. 2022;10(37):19560-19571. DOI:10.1039/D2TA02610D

84. Chaban VV, Andreeva NA. Sodium-ion electrolytes based on ionic liquids: a role of cation-anion hydrogen bonding. *Journal of Molecular Modeling*. 2016;22(8):172. DOI:10.1007/s00894-016-3042-9

85. Chaban VV. The tricyanomethanide anion favors low viscosity of the pure ionic liquid and its aqueous mixtures. *Physical Chemistry Chemical Physics*. 2015;17(47):31839-31849. DOI:10.1039/C5CP05666G

Information about the authors / Информация об авторах

Nadezhda A. Andreeva, Cand. Sc. (Phys. and Math.), Associate Professor, Peter the Great St.Petersburg Polytechnic University, St. Petersburg, Russian Federation; ORCID 0000-0003-0723-4080; e-mail: nadezhda.a.andreeva@gmail.com

Vitaly V. Chaban, D. Sc. (Chem.), Professor, Yerevan State University, Yerevan, Armenia; ORCID 0000-0002-3399-6567; e-mail: vvchaban@gmail.com

Андреева Надежда Анатольевна, кандидат физико-математических наук, доцент, Санкт-Петербургский политехнический университет Петра Великого, Санкт-Петербург, Российская Федерация; ORCID 0000-0003-0723-4080; e-mail: nadezhda.a.andreeva@gmail.com

Чабан Виталий Витальевич, доктор химических наук, профессор, Ереванский государственный университет, Ереван, Республика Армения; ORCID 0000-0002-3399-6567; e-mail: vvchaban@gmail.com

Received 17 July 2025; Revised 22 August 2025; Accepted 26 August 2025

Территория распространения – Российская Федерация, зарубежные страны
Distributed is the Russian Federation and foreign countries

Computer layout: Olga V. Mochalina, TSTU, Tambov, Russian Federation
Компьютерный дизайн и верстка: Мочалина О. В., ТГТУ, Тамбов, Россия

Оригинал-макет подготовлен в Издательском центре ФГБОУ ВО «ТГТУ»,
392032, Тамбовская обл., г. Тамбов, ул. Мичуринская, д. 112А

Подписано в печать 27.11.2025. Дата выхода в свет 12.12.2025.
Формат 60×90/8. Усл. печ. л. 11,75. Уч.-изд. л. 12,22. Тираж 100 экз. Цена свободная. Заказ № 040.
СМИ журнал “Journal of Advanced Materials and Technologies”
(Журнал современных материалов и технологий) выпуск 2025. Том 10, № 4